Lattice Boltzmann Methods for Flows of Complex Fluids

Edward Lewis

Supervised by Prof. T.N. Phillips

A thesis presented for the degree of
Doctor of Philosophy

School of Mathematics
Cardiff University
United Kingdom
2017

Acknowledgements

Firstly I would like to thank my supervisor, Professor Tim Phillips, for his time, care and understanding throughout the time I have been at Cardiff University. His advice and guidance has always been very useful and gratefully received and our frequent meetings is something I am going to miss on completion of my studies. I would also like to thank Cardiff University's School of Mathematics for providing such a stimulating academic environment. The people in the department provide that extra bit of inspiration and joy on a cold wet winter Welsh morning. Finally, I would like to thank my family and my fiancée for their love, support and gracious understanding. It is difficult to imagine how I could have done this without them.

Declaration

This work has not previously been accepted in substance for any degree and is not concurrently submitted in candidature for any degree.

Signed.....Date.....

Statement 1

This thesis is being submitted in partial fulfilment of the requirements for the degree of PhD.

Signed..... Date.....

Statement 2

This thesis is the result of my own independent work/investigation, except where otherwise stated. Other sources are acknowledged by explicit references.

Signed..... Date.....

Statement 3

I hereby give consent for my thesis, if accepted, to be available for photocopying and for inter-library loan, and for the title and summary to be made available to outside organisations.

Signed..... Date.....

Statement 4

I hereby give consent for my thesis, if accepted, to be available for photocopying and for inter-library loans after expiry of a bar on access approved by the Graduate Development Committee.

Signed..... Date.....

Abstract

This thesis presents the extension of the lattice Boltzmann method (LBM) to the solution of the Fokker-Planck equation with the FENE force law, on a single lattice for the use of modelling the flows of polymeric liquids. First implementation and the basic theory of the LBM is discussed including the derivation of the equilibrium function as a discretisation of the Maxwell-Boltzmann distribution function using Gauss-Hermite quadrature and the recovery of the Navier-Stokes equations from the LBE by use of multiscale analysis. A review of the extension of the LBM to multiphase flow is presented including colour models, pseudo-potential models and free energy models. Numerical results for a colour model have been given. Current viscoelastic lattice Boltzmann methods are discussed including results validating the approach by Onishi et al. [75] in the cases of simple shear flow and start up shear flow. A LBM for the Fokker-Planck equation with the FENE force law is developed based on a new Gauss quadrature rule that has been derived. The validity of this method is confirmed for small We by comparison with results by Ammar [2] and Singh et al. [96] where it gives good agreement. A LBM for the Fokker-Planck equation is then coupled with a macroscopic solver for the solvent velocity to solve start-up plane Couette flow. This approach is validated by comparison with results by Leonenko and Phillips [60].

Contents

Chapter 1

Introduction

The lattice Boltzmann method (LBM) is an algorithm for simulating the flows of fluids. Conventional numerical schemes, such as finite difference, finite elements and finite volumes, rely on discretising macroscopic continuum equations. However, the LBM is a discrete kinetic theory approach that features a mescoscale description of the microstructure of the fluid.

The most commonly used macroscopic continuum equations used in fluid dynamics are the Navier-Stokes equations

$$\rho \frac{D\mathbf{u}}{Dt} = -\nabla P + \eta \nabla^2 \mathbf{u} + \rho \mathbf{b}, \tag{1.0.1}$$

$$\nabla \cdot \mathbf{u} = 0. \tag{1.0.2}$$

where $\mathbf{u}$ is the macroscopic fluid velocity, ρ is the fluid density, P is the fluid pressure, η is the dynamic viscosity, $\mathbf{b}$ is body force (e.g. gravity) and the material derivative is given by

$$\frac{D}{Dt} = \frac{\partial}{\partial t} + \mathbf{u} \cdot \nabla. \tag{1.0.3}$$

1.0.1 Finite Difference methods

In finite difference methods, differential equations are approximated with difference equations, in which finite differences approximate the derivatives. For example, first we need to define a grid of points in the domain $D = [a, b] \times [c, d]$. We choose step sizes $\Delta x = \frac{b-a}{N}$ and $\Delta y = \frac{d-c}{M}$ in the x and y directions, re-

spectively (where N and M are integers) and a time step size Δt. We draw a set of horizontal and vertical lines across D, and get a set of intersection points (x_i, y_j, t_n), or simply (i, j, n), where $x_i = a + i\Delta x$, $i = 0, \ldots, N$, $y_j = a + j\Delta y$, $j = 0, \ldots, M$, and $t_n = n\Delta t$. Then using first order forward difference for time discretisation, first order backwards difference for first order space derivative and second order central difference for second order space derivative, the component of the momentum equation in the x-direction is given by

$$\begin{aligned}&\frac{u_{ij}^{n+1} - u_{ij}^n}{\Delta t} + u_{ij}^n \frac{u_{ij}^n - u_{i-1,j}^n}{\Delta x} + v_{ij}^n \frac{u_{ij}^n - u_{i-1,j}^n}{\Delta y} \\ &\quad = -\frac{1}{\rho}\frac{p_{i+1,j}^n - p_{i-1,j}^n}{2\Delta x} + \eta\left(\frac{u_{i+1,j}^n - 2u_{ij}^n + u_{i-1,j}^n}{\Delta x^2} + \frac{u_{i,j+1}^n - 2u_{ij}^n + u_{i,j-1}^n}{\Delta y^2}\right)\end{aligned}$$

where u_{ij}^n is the velocity in the x direction at the point (i, j, n). Finite difference methods have a few drawbacks. For hyperbolic systems, the differential equations do not hold at discontinuities, whereas the integral conservation laws do and in practice finite difference methods require structured meshes making simulating the flow around complex geometries (such as flow through porous media) very difficult to implement.

1.0.2 Finite Volume methods

Finite volume methods are similar to finite difference methods in that values are calculated at discrete points on a meshed geometry. The basis of the finite volume method is the integral conservation law. The essential idea is to divide the domain into many control volumes and approximate the integral conservation law on each of the control volumes. Because the flux entering a given volume is identical to that leaving an adjacent volume, these methods are conservative. Finite volume methods are also easily formulated to allow for unstructured meshes. Beginning with the incompressible form of the momentum equation divided through by the density ($p = P/\rho$) and density has been absorbed into the body force term f_i

$$\frac{\partial u_i}{\partial t} + \frac{\partial u_i \partial u_j}{\partial x_j} = -\frac{\partial p}{\partial x_i} + \nu \frac{\partial^2 u_i}{\partial x_j \partial x_j} + f_i. \tag{1.0.4}$$

The equation is integrated over the control volume of a computational cell

$$\int\int\int_V \left[\frac{\partial u_i}{\partial t} + \frac{\partial u_i \partial u_j}{\partial x_j}\right] dV = \int\int\int_V \left[-\frac{\partial p}{\partial x_i} + \nu \frac{\partial^2 u_i}{\partial x_j \partial x_j} + f_i\right] dV \quad (1.0.5)$$

The time dependent term and the body force term are assumed to be constant over the volume of the cell. The divergence theorem is applied to remaining terms to give

$$\frac{\partial u_i}{\partial t} V + \int\int_A u_i u_j n_j dA = -\int\int_A p n_i dA + \int\int \nu \frac{\partial u_i}{\partial x_j} n_j dA + f_i V \quad (1.0.6)$$

where n is the normal of the surface of the control volume and V is the volume. Usually polyhedra are used as control volumes and values are assumed constant over each face, and so the area integrals can be written as summations over each face

$$\frac{\partial u_i}{\partial t} V + \sum_{nbr} (u_i u_j n_j A)_{nbr} = -\sum_{nbr} (p n_i A)_{nbr} + \sum_{nbr} \left(\nu \frac{\partial u_i}{\partial x_j} n_j A\right)_{nbr} + f_i V \quad (1.0.7)$$

where the subscript nbr denotes the value at any given face.

1.0.3 Finite Element methods

The finite element method again formulates the problem in terms of a system of algebraic equations. The method yields approximate values of the unknowns at discrete number points over the domain. To solve the problem, it subdivides the computational domain into a number of finite elements. The simple equations that model these finite elements are then assembled into a larger system of equations that model the entire problem. FEM then uses variational methods to approximate a solution by minimizing an associated error function.

For example, we consider the two dimensional steady flow problem in a domain Ω where the fluid velocity $\mathbf{u} = 0$ at the boundary Γ. The formulation

of our example is now. For $x \in \Omega$ solve $\mathbf{u}$ satisfying

$$\text{div } \mathbf{u} = 0, \tag{1.0.8}$$

$$-\text{ div } \boldsymbol{\sigma} + \rho(\mathbf{u} \cdot \nabla \mathbf{u}) = \rho \mathbf{b}, \tag{1.0.9}$$

$$\boldsymbol{\sigma}_{ij} = -P\delta_{ij} + \mathbf{T} \tag{1.0.10}$$

$$\mathbf{u} = 0 \quad \text{for } \mathbf{x} \in \Gamma. \tag{1.0.11}$$

where $\mathbf{T}$ is the deviatoric extra stress tensor. Define the solution space for $\mathbf{u}$ as

$$V = H_E^1(\Omega) = \left\{ v : \int_\Omega (v(x))^2 d\Omega + \int_\Omega |\nabla v(x)|^2 d\Omega \leq C_1, \quad v = 0 \text{ on } \Gamma \right\}. \tag{1.0.12}$$

and the solution space for P as

$$Q = H_E(\Omega) = \left\{ q : \int_\Omega (q(x))^2 d\Omega \leq C_2 \right\}. \tag{1.0.13}$$

In order to derive the weak formulation, equations (1.0.8) and (1.0.9) must be multiplied by test functions that belong to the solution space. First equation (1.0.8) is multiplied by a test function $\mathbf{q}$ and integrated over Ω which yields

$$\int_\Omega q \text{ div } \mathbf{u} d\Omega = 0. \tag{1.0.14}$$

The momentum equations (1.0.9) consist of two equations (one for the x and y directions), which are each multiplied by separate test functions v_1 and v_2 and then integrated over Ω. By defining $\mathbf{v} = (v_1, v_2)^\dagger$ these equations can be combined to

$$\int_\Omega (-\text{ div } \boldsymbol{\sigma} + \rho(\mathbf{u} \cdot \nabla \mathbf{u})) \cdot \mathbf{v} d\Omega = \int_\Omega \mathbf{b} \cdot \mathbf{v} d\Omega. \tag{1.0.15}$$

The first term in (1.0.15) is further reduced by applying integration by parts (Divergence theorem) to

$$\int \Omega(-\text{ div}\boldsymbol{\Sigma}) \cdot \mathbf{v} d\Omega = \int_\Omega \boldsymbol{\sigma} \cdot \nabla \mathbf{v} d\Omega - \int_\Gamma \mathbf{n} \cdot \boldsymbol{\sigma} \cdot \mathbf{v} d\Gamma \tag{1.0.16}$$

where $\mathbf{n}$ is the outward pointing unit normal vector. Furthermore by substituting equation (1.0.10) into (1.0.16), the first term of (1.0.15) may be written as

$$\int \Omega(-\ \mathrm{div}\boldsymbol{\Sigma}) \cdot \mathbf{v} d\Omega = \int_\Omega \mathbf{T} \cdot \nabla \mathbf{v} d\Omega + \int_\Omega P\ \mathrm{div}\ \mathbf{v} d\Omega - \int_\Gamma \mathbf{n} \cdot \boldsymbol{\sigma} \cdot \mathbf{v} d\Gamma \tag{1.0.17}$$

Combining these results leads to the weak formulation of the Navier-Stokes equations. Find $\mathbf{u} \in V$ and $P \in Q$ with

$$\mathbf{u} = 0 \text{ at } \Gamma, \tag{1.0.18}$$

such that

$$\int_\Omega q\ \mathrm{div}\ \mathbf{u} d\Omega = 0, \tag{1.0.19}$$

$$\int_\Omega \mathbf{T} \cdot \nabla \mathbf{v} d\Omega + \int_\Omega \rho(\mathbf{u} \cdot \nabla \mathbf{u}) \cdot \mathbf{v} d\Omega - \int_\Omega P\ \mathrm{div}\ \mathbf{v} d\Omega = \int_\Omega \rho \mathbf{b} \cdot \mathbf{v} d\Omega, \tag{1.0.20}$$

for all $\mathbf{v}$ such that $\mathbf{v} = 0$ at Γ, Ω is the fluid domain boundary, Γ is the boundary of Ω and $\mathbf{T}$ is the deviatoric extra stress tensor. We see that no derivatives of P and q are necessary and so it is sufficient that P and q are integrable. For $\mathbf{u}$ and $\mathbf{v}$, first derivatives are required and hence not only $\mathbf{u}$ and $\mathbf{v}$ but also their first derivatives must be integrable.

In the standard Galerkin method we define a basis function $\Psi_i(\mathbf{x})$ for the pressure components and functions $\Phi_{ij}(\mathbf{x})$ for the vector components (Φ_{i1} and Φ_{i2} for the x and y directions). Now the approximation of $\mathbf{u}$ and P will be defined by

$$p_h = \sum_{j=1}^{m} p_j \Psi_j(\mathbf{x}) \tag{1.0.21}$$

$$\mathbf{u}_h = \sum_{j=1}^{n} u_{1j}\Phi_{j1}(\mathbf{x}) + u_{2j}\Phi_{j2}(\mathbf{x}) = \sum_{j=1}^{2n} u_j \Phi_j(\mathbf{x}). \tag{1.0.22}$$

In equation (1.0.22) u_j is defined by $u_j = u_{1j}$ $(j = 1, \ldots, n)$, $u_{j+n} = u_{2j}$ $(j = 1, \ldots, n)$ and Φ_j in the same way. In order to get the standard Galerkin

formulation we substitute $\mathbf{v} = \Phi_i(\mathbf{x}), q = \Psi_i(\mathbf{x})$ into the weak formulation. In this way we get, find p_h and $\mathbf{u}_h$ defined by equations (1.0.21,1.0.22) such that

$$\int_\Omega \Psi_i \text{ div } \mathbf{u}_h d\Omega = 0, \quad i = 1, \ldots, m \tag{1.0.23}$$

and

$$\int_\Omega \mathbf{T} \cdot \nabla \Phi_i d\Omega + \int_\Omega \rho(\mathbf{u}_h \cdot \nabla \mathbf{u}_h) \cdot \Phi_i d\Omega \tag{1.0.24}$$

$$-\int_\Omega P \text{ div } \Phi_i d\Omega = \int_\Omega \rho \mathbf{b} \cdot \Phi_i d\Omega, \quad i = 1, \ldots, m. \tag{1.0.25}$$

The finite element method may be used to construct the basis functions Φ_i and Ψ_i and once they are known the integrals (1.0.23) and (1.0.25) may be evaluated element-wise. This produces a system of $m+2n$ non-linear equations with $m + 2n$ unknowns. The solution of the system of equations introduces two difficulties, firstly the equations are non-linear so require an iterative solver and secondly the equations resulting from the mass equation do not contain the unknown pressure P. For a finite element problem to be well-posed it is necessary that the test spaces satisfy the well known LBB condition. In general finite element methods are very amenable to unstructured meshes but are more difficult to formulate and implement when compared to finite difference schemes.

With the LBM the aim is to construct simplified kinetic type models that preserve the conservation laws (e.g. mass, momentum) and necessary symmetries (e.g. Galilean invariance) so that in the macroscopic limit, the macroscopic averaged properties obey the desired continuum equations of motion, such as the Navier-Stokes equations. These simplified models are sufficient since the macroscopic dynamics are not sensitive to the underlying details of the microscopic physics.

The LBM developed in the late 1980s has seen rapid development and is now being used for many applications such as heat convection in buildings [54], blood coagulation in a human artery [4] and modelling of fluid turbulence [19].

1.1 Different Modelling Approaches

People have been interested in the world around them for thousands of years but it is only in the last few centuries that we have started to quantify physical phenomena. The physics of fluids is very complicated and for all but the simplest of flows is poorly understood. With the rise of computing power it has been possible to start to model fluids numerically. Traditionally scientists have modelled fluids at a continuum scale, where fluids are described in terms of space filling fields, such as density, velocity, and pressure, that vary smoothly in space and time. Such a description is fairly adequate for many applications, to the point that the physics of fluids is often implicitly identified with continuum fluid mechanics. Nevertheless, it has been known for over a century, that fluids (gas and liquids) are ultimately composed of a collection of individual entities, atoms and molecules, whose discrete nature becomes apparent at scales around the nanometre and below.

The different levels of description have an associated characteristic length scale. At the macroscopic level there may be a number of such lengths such as the width of a channel or the diameter of an object in the flow. These are examples of geometric lengths but more intrinsic flow properties like the diameter of a vortex shed in turbulent flow may also be considered. Denote the smallest of the hydrodynamic length scales by L_H. At the particle, or microscopic scale, the characteristic length scale is generally taken to be the mean free path, L_{mfp}, which is the average distance particles travel between collisions. A basic hypothesis underlying continuum fluid mechanics is that the macroscopic description holds whenever $L_H \gg L_{mfp}$, or alternatively

$$\varepsilon = \frac{L_{mfp}}{L_H} \ll 1, \tag{1.1.1}$$

where ε is known as the Knudsen number.

For a purely microscopic approach we consider a collection of N particles of mass m moving in a volume V at time t, each with position vector $\mathbf{x}_i$, $i = 1, \ldots, N$. Let each particle move freely under the influence of a force $\mathbf{F}_i$.

The particles are described by the Hamiltonian equations of motion:

$$\frac{d\mathbf{x}_i}{dt} = \frac{\mathbf{j}_i}{m}, \tag{1.1.2}$$

$$\frac{d\mathbf{j}_i}{dt} = \mathbf{F}_i \tag{1.1.3}$$

where $\mathbf{j}_i$ is the momentum of particle i. If initial conditions and boundary conditions are specified, the Hamiltonian equations can, in principle, be solved in time to give full knowledge of the state of the system. However, the number of particles N in V is large. In fact, it is typically very large indeed. If we had a $1\,\mathrm{m}^3$ box full of air at room temperature, we would have roughly 10^{25} particles. This is why simply solving the Hamiltonian equations is an infeasible task in practice.

The macroscopic approach does not consider the internal structure of V but instead considers it to be an arbitrary material volume fixed in space with a density ρ and a momentum which is assumed to satisfy the conservation laws of Newtonian mechanics so that

$$\frac{d}{dt}\int_V \rho dV = 0, \tag{1.1.4}$$

$$\frac{d}{dt}\int_V \rho\mathbf{u} dV = \int_S \mathbf{n}\cdot\boldsymbol{\sigma} dS + \int_V \rho\mathbf{b} dV, \tag{1.1.5}$$

where $\mathbf{u}$ is the fluid velocity, $\boldsymbol{\sigma}$ is a stress tensor, S is the surface of V with outward normal $\mathbf{n}$ and $\mathbf{b}$ is a body force (such as gravity). Applying the divergence and Reynolds transport theorems yields, under the assumptions that all integrands are continuous and the fluid is incompressible, the macroscopic equations of motion for a fluid are

$$\nabla\cdot\mathbf{u} = 0, \tag{1.1.6}$$

$$\rho\frac{D\mathbf{u}}{Dt} = \nabla\cdot\boldsymbol{\sigma} + \rho\mathbf{b}, \tag{1.1.7}$$

where

$$\frac{D}{Dt} = \frac{\partial}{\partial t} + \mathbf{u}\cdot\nabla \tag{1.1.8}$$

is the material derivative. To derive an explicit form of the stress tensor we

write the components $\sigma_{\alpha\beta}$ of $\boldsymbol{\sigma}$ in the form

$$\sigma_{\alpha\beta} = -P\delta_{\alpha\beta} + T_{\alpha\beta}, \tag{1.1.9}$$

where $\delta_{\alpha\beta}$ is the usual Kronecker delta function and $\mathbf{T}$ is the deviatoric extra stress tensor. Define P, the pressure, to be the negative average of the diagonal stress components, i.e.

$$P = -\frac{1}{3}\operatorname{Tr}\sigma. \tag{1.1.10}$$

A constitutive equation is needed to model the extra stress tensor $\mathbf{T}$ to close the system of equations. This can take many forms depending on the type of fluid that is to be modelled. For a Newtonian fluid it is assumed that the extra stress tensor is proportional to the rate of strain $\dot{\boldsymbol{\gamma}}$ i.e.

$$\mathbf{T} = \eta\dot{\boldsymbol{\gamma}}, \tag{1.1.11}$$

where η, is known as the viscosity and the rate of strain tensor is defined to be

$$\dot{\boldsymbol{\gamma}} = \nabla\mathbf{u} + (\nabla\mathbf{u})^{\dagger}, \tag{1.1.12}$$

and $\dagger$ denotes the matrix transpose. With $\mathbf{T}$ defined in (1.1.11), the Navier-Stokes equations can be recovered

$$\rho\frac{D\mathbf{u}}{Dt} = -\nabla P + \eta\nabla^2\mathbf{u} + \rho\mathbf{b}, \tag{1.1.13}$$

$$\nabla\cdot\mathbf{u} = 0. \tag{1.1.14}$$

This forms a continuum model that assumes the underlying physical system is smoothly varying, in contrast to physical fluids which are actually composed of a fixed number of discrete particles. The Navier-Stokes equations (1.1.13), (1.1.14) are highly nonlinear and analytic solutions are rarely available. Therefore, numerical solutions become necessary and traditionally this has been achieved through finite volume or finite element methods (local methods) or spectral elements (global method). For many real life problems, such as the aerodynamic properties of cars or weather forecasting, these techniques have proved to be very successful, especially in predicting qualitative behaviour of fluid flows. However there are some potential issues which can cause com-

putational difficulties. For example, there may be truncation errors and numerical instabilities due to the necessary discretisation process, irregular fluid domain boundaries which are difficult to incorporate (in particular with the finite volume method), a Poisson solver is often required to solve for the pressure (which is computationally expensive), issues with the ill-posedness of the discrete problem caused by possible incompatibilty between the approximation spaces (finite and spectral element methods), the nonlinearity of the Navier-Stokes equations and for multiphase flows, the interface between the two fluids has to be tracked in time (which is not easily achieved by continuum-based methods). For non-Newtonian fluids that have a complex constitutive equation for the stress, care must be taken to avoid extra numerical instabilities and spurious oscillations when dealing with the convective term, $\mathbf{u} \cdot \nabla \mathbf{T}$.

Modern computing architectures are driving the demand for CFD techniques that are amenable to parallel computing. There are two main issues with producing an algorithm suitable for parallel computing,

(i) the fraction of parallel content

(ii) the load balance.

To illustrate (i), suppose we were given the task of summing N numbers. We could get P processors to sum a fraction of the numbers each but there is a serial bottleneck when it comes to summing these P partial sums. An algorithm with many such bottlenecks will not work well on parallel computers. The benefit ($S(P)$) of using P processors, where W is the fraction of work that can be performed in parallel is given in [100] by

$$S(P) = \frac{1}{W/P + (1 - W)}. \tag{1.1.15}$$

This equation shows that in the limit of an infinite number of processors, the speed up asymptotes to $S(\infty) = 1/(1 - W)$. As an example suppose we have ninety percent parallel code, the above equation shows that the maximum pay off will never exceed a factor of 10. Therefore 10 processors is approximately the threshold above which further parallelisation becomes wasteful. For reference large scale LBM easily place more than 99 percent of the computer demand on the collision phase which is perfectly parallel [100] giving scope for

the use of more than 100 processors.

Load balancing, (ii) refers to making sure each processor is doing roughly the same amount of work, as computational speed can be limited by the speed of the slowest processor. With regular geometries, load balancing is a trivial matter, where a simple geometric domain decomposition assures good performance. When the geometry is complex and possibly even changing in time it is difficult a priori to know how to ensure each processor is performing even approximately the same amount of work. LBM has a simple data structure and so is well positioned to steer clear of load balancing issues for many practical applications.

A third intermediate level of description is provided by kinetic theory. This connects the small scale (L_{mfp}) microscopic picture with the large scale (L_H) macroscopic properties. Kinetic theory considers a statistical description of the fluid microstructure and defines the physical observables (e.g. density, velocity, temperature, pressure) to be averages over a large number of molecular histories. The primary variable in kinetic theory is not the position of a particle or the macroscopic velocity, but instead the distribution function, $f(\mathbf{x}, \boldsymbol{\xi}, t)$, which is defined to be the probability of finding a particle at position $\mathbf{x}$ with velocity $\boldsymbol{\xi}$ at time t.

In 1872 Ludwig Boltzmann devised the famous Boltzmann equation which describes the statistical behaviour of a thermodynamic system not in thermodynamic equilibrium which reads

$$\partial_t f + \boldsymbol{\xi} \cdot \nabla f = \Omega(f) \tag{1.1.16}$$

where $f = f(\mathbf{x}, \boldsymbol{\xi}, t)$ is the single particle distribution function, $\boldsymbol{\xi}$ is the microscopic velocity, and $\Omega(f)$ is a collision operator, so that $f(\mathbf{x}, \boldsymbol{\xi}, t) d^3\mathbf{x} d^3\boldsymbol{\xi}$ is the probability of finding a particle in the volume $d^3\mathbf{x}$ around $\mathbf{x}$ with velocity between $\boldsymbol{\xi}$ and $\boldsymbol{\xi} + d\boldsymbol{\xi}$.

The macroscopic variables are determined from the moments of the distri-

bution function

$$\rho(\mathbf{x},t) = \int f(\mathbf{x},\boldsymbol{\xi},t)d\boldsymbol{\xi}, \tag{1.1.17}$$

$$\rho(\mathbf{x},t)\mathbf{u}(\mathbf{x},t) = \int \boldsymbol{\xi} f(\mathbf{x},\boldsymbol{\xi},t)d\boldsymbol{\xi}, \tag{1.1.18}$$

$$\rho(\mathbf{x},t)e(\mathbf{x},t) = \int (\boldsymbol{\xi}-\mathbf{u})^2 f(\mathbf{x},\boldsymbol{\xi},t)d\boldsymbol{\xi}, \tag{1.1.19}$$

where ρ is the fluid density, $\mathbf{u}$ is the fluid velocity and e is the internal energy, the energy contained within the system excluding the kinetic and potential energy of the system as a whole.

The collision operator $\Omega(f)$ is very complicated and suitable approximations need to be constructed to make the LBE amenable to numerical computations. The assumption behind many simplifications to Ω is that a large amount of information about the two-body interactions is unlikely to influence, to a great extent, the values of experimentally measured quantities.

Cercignani [12] showed that the collision integral possesses exactly five elementary collision invariants $\psi_k(\mathbf{c}), k = 0,\ldots,4$, i.e.

$$\int \Omega(f,f)\psi_k(\mathbf{c})d\mathbf{c} = 0. \tag{1.1.20}$$

These are

$$\psi_0 = 1, \quad (\psi_1,\psi_2,\psi_3) = \mathbf{c}, \psi_4 = \mathbf{c}^2. \tag{1.1.21}$$

Simpler collision operators should also satisfy this constraint as well as the tendency to a Maxwellian distribution (H-theorem) [81]. The most commonly chosen approximation to the collision operator is the Bhatnagar-Gross-Krook (BGK) operator [5]

$$\Omega(f) = -\frac{1}{\lambda}(f - f^{eq}) \tag{1.1.22}$$

which represents a simplified description of a particle's relaxation to a local equilibrium state due to collisions. In equation (1.1.22), λ is the relaxation time (characteristic time taken to relax to the equilibrium solution) due to collisions and f^{eq} is the Boltzmann-Maxwellian distribution function

$$f^{eq} = \frac{\rho}{(2\pi RT)^{D/2}} \exp\left(-\frac{(\boldsymbol{\xi}-\mathbf{u})^2}{2RT}\right), \tag{1.1.23}$$

where R is the ideal gas constant, D is the dimension of physical space, and ρ, $\mathbf{u}$ and T are the macroscopic density, velocity and temperature, respectively.

This simplified model does have some disadvantages as the relaxation time simultaneously controls the fluid viscosity and the discretisation errors. Solutions obtained with the BGK model generally exhibit λ-dependent and therefore viscosity-dependent characteristics. Thus the fundamental physical requirement that hydrodynamic solutions are uniquely determined by their non-dimensional physical parameters is not satisfied [53] (p. 143).

The connection between kinetic theory and hydrodynamics is provided by multiscale analysis, which separates the different spatial and temporal scales within a fluid. This is done using Chapman-Enskog analysis on Boltzmann's equation (1.1.16) which allows one to derive the Navier-Stokes equations (1.1.13) and (1.1.14).

1.2 The Lattice Gas Cellular Automaton

In 1986, Frisch, Hasslacher and Pomeau [30] showed that a simple cellular automaton (commonly called FHP after the authors' initials) which obeyed only simple conservation laws at a microscopic level, was able to reproduce the complexity of real fluid flows. This was the subject of great excitement in the CFD community. The prospects were promising: a round-off free, intrinsically parallel computational paradigm for fluid flow and perhaps, even more importantly the analogue of the Ising model for turbulence [100]. A few serious problems (such as statistical noise and amenability to three dimensions) were quickly recognised and the Lattice Boltzmann Equation (LBE) was developed in its wake as a response to some of drawbacks of LGCA [45]. LBE is now viewed as its own self-standing research subject in its own right and it can be derived independently, without reference to LGCA at all. However, it is still useful to start with a brief overview of LGCA as it aids our understanding of the LBE.

The FHP lattice, which is shown in Figure 1.2.1, is a regular lattice with hexagonal symmetry and associated with each node are the six link vectors defined by

$$\mathbf{c}_i = \left(\cos\frac{i\pi}{3}, \sin\frac{i\pi}{3}\right), \quad i = 1, \ldots, 6, \tag{1.2.1}$$

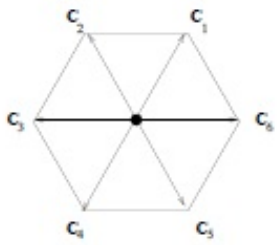

Figure 1.2.1: The FHP lattice.

and $|\mathbf{c}_i| = 1$ for all i. Each lattice site hosts up to six particles with the following prescriptions:

- All particles have the same mass $m = 1$.
- Particles can move only along one of the six directions defined by the discrete displacements $\mathbf{c}_i$.
- In a time step the particles hop to the nearest neighbour in the direction of the corresponding discrete vector $\mathbf{c}_i$. Both longer and shorter jumps are forbidden, which means all lattice particles have the same energy.
- No two particles sitting on the same site can move along the same direction $\mathbf{c}_i$ (exclusion principle) in the same time step.

Although real molecules can move at virtually any speed (subject to special relativity) and in any direction this apparently poor cartoon of true molecular dynamics has all that it takes to simulate realistic hydrodynamics.

We can readily code the information of the system by using a single binary digit per site and direction so that the entire state of the lattice gas is specified by $6N$ bits, where N is the number of lattice sites. Define the occupation variables $n_i(\mathbf{x}, t)$ such that

$$n_i(\mathbf{x}, t) = 0 \quad \text{particle, with velocity in } i \text{ direction, absence at site } \mathbf{x} \text{ and time } t, \tag{1.2.2}$$

$$n_i(\mathbf{x}, t) = 1 \quad \text{particle, with velocity in } i \text{ direction, presence at site } \mathbf{x} \text{ and time } t. \tag{1.2.3}$$

LGCA consists of two main stages, propagation/streaming, in which each

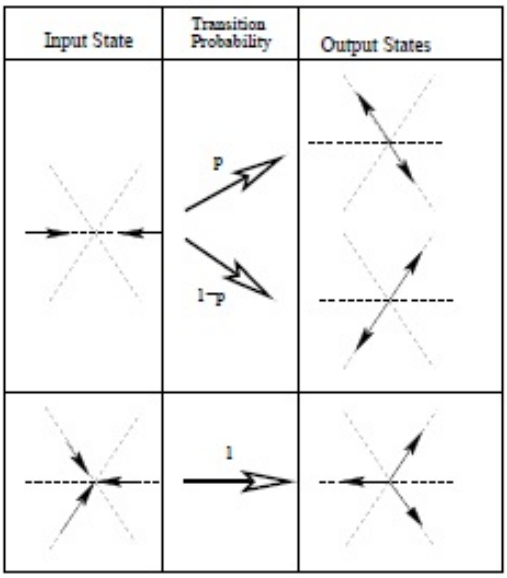

Figure 1.2.2: The collision rules on the FHP lattice. The numbers on the open arrows are the transition probabilities. The most common choice for p is 0.5

particle hops to one of its nearest neighbours according to its momentum, and collision in which particles entering the same lattice site interact and change their momentum according to a set of pre-determined collision rules (in practice this is done by use of a look-up table).

The LGCA evolution can now be described by the equation

$$n_i(\mathbf{x} + \mathbf{c}_i, t + 1) - n_i(\mathbf{x}, t) = \Omega_i(\mathbf{n}) \tag{1.2.4}$$

where Ω_i is the collision operator that acts on all particles $\mathbf{n} = \{n_i : i = 1, \ldots, 6\}$. The collision operator Ω_i must conserve mass and momentum, i.e.

$$\sum_i \Omega_i = 0, \tag{1.2.5}$$

$$\sum_i \Omega_i \mathbf{c}_i = 0. \tag{1.2.6}$$

In the HPP model the collision phase is deterministic whereas the FHP model features a partially stochastic process. If there is a head-on two body collision then the incoming particles will rotate by either $+\frac{\pi}{3}$ or $-\frac{\pi}{3}$ with probabilities p and $1 - p$, respectively. Examples are shown in Figure 1.2.2.

In order to calculate macroscopic quantities such as density and momentum, we first start by averaging n_i over a small subdomain $\mathbf{x}$ in some suitable manner to reduce the statistical noise associated with LGCA. The region in which spatial averaging takes place must be small compared to a typical macroscopic length scale of the flow. The mean occupation numbers N_i are then used to calculate the macroscopic density, momentum and momentum flux tensor defined, respectively, by

$$\rho(\mathbf{x},t) = \sum N_i(\mathbf{x},t) \tag{1.2.7}$$

$$\rho(\mathbf{x},t)u_\alpha(\mathbf{x},t) = \sum N_i(\mathbf{x},t)c_{i\alpha} \tag{1.2.8}$$

$$\Pi_{\alpha\beta}(\mathbf{x},t) = \sum N_i(\mathbf{x},t)c_{i\alpha}c_{i\beta} \tag{1.2.9}$$

where u_α is the α component of velocity $\mathbf{u}$. Rivet and Boon [87] have shown that the FHP lattice gas, can give rise to the full equations of motion for a real isotropic fluid.

Despite the elegance and practical appeal of round-off-free parallel computing, LGCA are plagued by a number of anomalies, such as statistical noise (common to any particle method) and broken symmetries which cannot be restored even in the limit of zero lattice spacing [21].

One such problem is encountered when we move into the third dimension. The only regular polytope that fills the whole space is the cube, while the only regular polytopes with a sufficiently large symmetry group are the dodecahedron and icosahedron. There is an elegant solution to this problem, d'Humières et al.[26] showed that a suitable lattice could be found by going into the fourth dimension. They showed that the Face Centred HyperCube (FCHC) has the correct properties. It consists of all neighbours of a given site (the central site) generated by the speeds $c_i = [\pm 1, \pm 1, 0, 0]$ and permutations thereof. This yields 24 speeds all with the same magnitude $c_i^2 = 2$.

If we examine the lattice (Figure 1.2.3) we see that the neighbours in the centre of a face are represented by two particles corresponding to the ± 1 in the fourth dimension. Although it solves the problem of isotropy in the third dimension, it dramatically increases the computational complexity. This was a decisive factor in the move from LGCA to LBM.

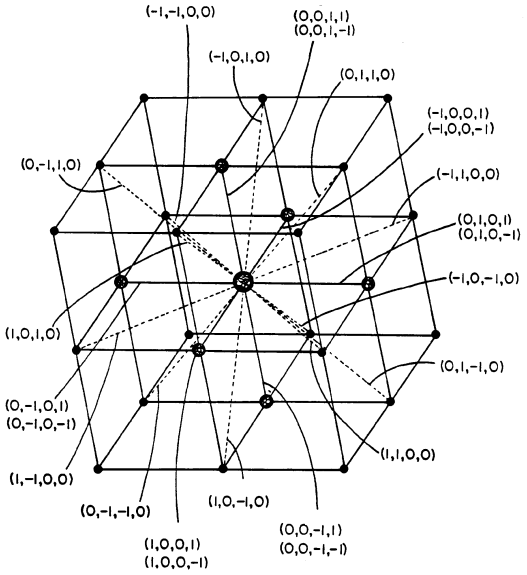

Figure 1.2.3: The face centered hypercubic lattice.

1.3 From LGCA to LBM

The Lattice Boltzmann Model (LBM) can be viewed as a direct extension of LGCA developed by researchers such as McNamara and Zanetti [69] to resolve some of the shortcomings of LGCA. The occupation variable n_i is replaced by the average population density $f_i(\mathbf{x}, t) = \langle n_i(\mathbf{x}, t) \rangle$. Taking the ensemble average of the LGCA evolution equation (1.2.4) leads to the non-linear LBE

$$f_i(\mathbf{x} + \mathbf{c}_i, t + 1) = f_i(\mathbf{x}, t) + \langle \Omega_i(\mathbf{n}) \rangle. \tag{1.3.1}$$

To obtain a kinetic equation in closed form Boltzmann's assumption that particles entering a collision are uncorrelated is used

$$f_i(\mathbf{x} + \mathbf{c}_i, t + 1) = f_i(\mathbf{x}, t) + \Omega_i(\mathbf{f}), \tag{1.3.2}$$

where $\mathbf{f} = [f_1, \ldots, f_b]$. In the lattice Boltzmann framework, the macroscopic density and momentum are defined by the zeroth and first moments of the

distribution function, respectively:

$$\rho = \sum_i f_i, \tag{1.3.3}$$

$$\rho \mathbf{u} = \sum_i f_i \mathbf{c}_i. \tag{1.3.4}$$

This solved some issues such as statistical noise but still had difficulties in three dimensions, a lack of Galilean invariance and a relatively high viscosity and therefore low Reynolds number barrier (due to the maximum number of collisions an automaton can support) [84].

The next major breakthrough was by Higuera and Jimenez [45] who conquered the exponential complexity limitation by considering perturbations of the local equilibrium function. The macrostates of the LBM are functions of the space variable $\mathbf{x}$ and vary slowly in space. Any significant variation takes place over distances much larger than the lattice length scale. We can say that the population distribution function departs slightly from the local equilibrium state and write

$$f_i = f_i^{(0)} + \varepsilon f_i^{(1)} + \varepsilon^2 f_i^{(2)} + \ldots, \tag{1.3.5}$$

where $f_i^{(0)} = f_i^{eq}$ is the equilibrium state and the expansion parameter (Knudsen number) $\varepsilon \ll 1$ is the ratio of the microscopic scale to the smallest macroscopic scale.

The equilibrium component is required to fulfil the following constraints

$$\sum_{i=1}^{b} f_i^{eq} = \rho, \tag{1.3.6}$$

$$\sum_{i=1}^{b} f_i^{eq} \mathbf{c}_i = \rho \mathbf{u}. \tag{1.3.7}$$

Upon inserting f_i into the collision term and expanding in a Taylor series about the equilibrium component we get

$$\Omega_i(f_i) \approx \Omega_i^{(0)} + \varepsilon \sum_j \frac{\partial \Omega_i^{(0)}}{\partial f_j} f_j^{(1)} + \frac{\varepsilon^2}{2} \sum_{jk} \frac{\partial^2 \Omega_i^{(0)}}{\partial f_j \partial f_k} f_j^{(1)} f_k^{(1)}, \tag{1.3.8}$$

where $\Omega_i^{(0)} = \Omega_i(f_i^{(0)})$. This equation can be simplified since $\Omega_i(f_i^{(0)}) = 0$ and

by the conservation of momentum $\frac{\partial \Omega_i^{(0)}}{\partial f_j} f_j^{(1)} = 0$ [84], so that we obtain the quasi-linear lattice Boltzmann equation

$$f_i(\mathbf{x} + \mathbf{c}_i, t+1) - f_i(\mathbf{x}, t) = \sum_j M_{ij} \left(f_j - f_j^{eq} \right), \tag{1.3.9}$$

where $M_{ij} = \frac{\partial \Omega_i^{(0)}}{\partial f_j}$, defines the collision matrix which determines the scattering rate between directions i and j. The importance of this procedure is that it reduces the complexity of the collision term from 2^b to b^2 and then, due to the symmetry of M_{ij}, to order b, thus making it computationally feasible to perform lattice Boltzmann simulations in three dimensions.

The viscosity of the LB fluid is entirely controlled by a single parameter, namely the leading nonzero eigenvalue of the scattering matrix M_{ij} [100]. The remaining eigenvalues are then chosen to improve stability. This raises the question that since transport is related to a single nonzero eigenvalue, why not simplify things and choose a one parameter scattering matrix? Many authors [16, 52, 82] raised this point simultaneously and defined the Lattice Bhatnagar Gross Krook (LBGK) model

$$f_i(\mathbf{x} + \mathbf{c}_i, t+1) - f_i(\mathbf{x}, t) = \omega \left(f_j - f_j^{eq} \right), \tag{1.3.10}$$

where ω, which is the first nonzero eigenvalue of M_{ij}, is a relaxation parameter. The LBGK model is the simplest and most efficient LBM that recovers the Navier-Stokes equations and is probably the most widely used due to its simplicity and ease of implementation.

1.4 Overview of the Lattice Boltzmann Model

The LBM simplifies Boltzmann's original idea of gas dynamics by reducing the number of particles and confining them to the nodes of a lattice. Although it is entirely possible to perform lattice Boltzmann simulations on the FHP lattice with additional 'rest' velocity, most simulations are now performed on square lattices. The common notation used for describing lattices used in LBM is DmQn where m is the number of dimensions and n is the number of velocities. The advantages of square lattices include greater accuracy due to the increased

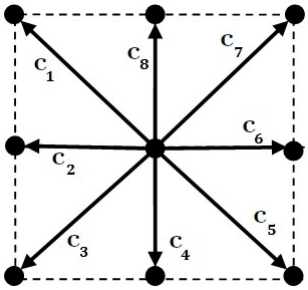

Figure 1.4.1: The D2Q9 Lattice

number of discrete velocity vectors [97], the ease of implementation and their amenability to three dimensional problems. To give a brief overview of the lattice Boltzmann method we shall discuss the D2Q9 model, which is two dimensional and consists of nine discrete velocity vectors. Figure 1.4.1 shows a typical lattice node of the D2Q9 model with nine velocities $\mathbf{c}_i$ defined by

$$\mathbf{c}_i = \begin{cases} (0,0) & i = 0 \\ (-1,1),(-1,0),(-1,-1),(0,-1) & i = 1,2,3,4 \\ (1,-1),(1,0),(1,1),(0,1) & i = 5,6,7,8 \end{cases} \tag{1.4.1}$$

where $\mathbf{c}_i = -\mathbf{c}_{i+4}$ for $i = 1,2,3,4$, as this makes coding easier.

We associate a discrete probability distribution function $f_i(\mathbf{x}_i, \mathbf{c}_i, t)$ or simply $f_i(\mathbf{x}_i, t)$ $i = 0, \ldots, 8$, which describes the probability of streaming in one particular direction. We can then discretise (1.1.16) to obtain

$$\underbrace{f_i(\mathbf{x} + \mathbf{c}_i\Delta t, t + \Delta t) - f_i(\mathbf{x}, t)}_{\text{streaming}} = \underbrace{\Omega_i}_{\text{collision}} . \tag{1.4.2}$$

where the key steps in LBM are the streaming (or propagation) and collision processes. When implementing the model the collision and propagation (streaming) steps are computed separately, and attention must be paid when applying boundary conditions since some types have to applied after the collision step and some after the propagation step. For example the on-grid bounce back boundary condition is applied after the propagation step but the mid-grid bounce back boundary condition is applied after the collision step.

The macroscopic fluid density, momentum and internal energy can be defined by moments of the microscopic particle distribution function,

$$\rho(\mathbf{x},t) = \sum_{i=0}^{8} f_i(\mathbf{x},t), \tag{1.4.3}$$

$$\rho(\mathbf{x},t)\mathbf{u}(\mathbf{x},t) = \sum_{i=0}^{8} \mathbf{c}_i f_i(\mathbf{x},t), \tag{1.4.4}$$

$$\rho(\mathbf{x},t)e(\mathbf{x},t) = \sum_{i=0}^{8} (\mathbf{c}_i - \mathbf{u})^2 f_i(\mathbf{x},t), \tag{1.4.5}$$

The equilibrium component (to be discussed in more detail in Chapter 3) to which the distribution function relaxes, is required to fulfil the following constraints:

$$\rho(\mathbf{x},t) = \sum_{i=0}^{8} f_i^{eq}(\mathbf{x},,t), \tag{1.4.6}$$

$$\rho(\mathbf{x},t)\mathbf{u}(\mathbf{x},t) = \sum_{i=0}^{8} \mathbf{c}_i f_i^{eq}(\mathbf{x},t). \tag{1.4.7}$$

When using the on-grid bounce-back boundary condition (which will be discussed in the next chapter), the algorithm can be summarized as follows:

1. Initialize ρ, $\mathbf{u}$, f_i and f_i^{eq}
2. Collision step: calculate the updated distribution functions
3. Propagation step: move $f_i \rightarrow f_i^*$ in the direction of $\mathbf{c}_i$
4. Compute the post propagation boundary conditions (if applicable)
5. Compute macroscopic ρ and $\mathbf{u}$ from f_i^* using the moment equations
6. Compute f_i^{eq} using the equilibrium equation
7. Advance time and repeat steps 2 to 7 until the stopping criteria are satisfied. For example a specified end time or convergence to a steady state solution.

In the case where mid-grid bounce-back condition is used, the boundary condition is computed after the collision step rather than after the propagation step.

Chapter 2

The Lattice Boltzmann Method: Implementation

In this chapter we will explore in greater depth different aspects of the LBM and how one would implement the algorithm in practice.

2.1 Collision Algorithm

When constructing simpler collision operators it has been common to use one of two different methods based on either a single relaxation time or multiple relaxation times. Single relaxation time methods tend to be faster and easier to implement and multiple relaxation times tend to be more stable.

BGK single relaxation time

A simplified collision model that satisfies the necessary constraints is the BGK (Bhatnagar, Gross Krook) approximation [5]:

$$\Omega(f) = \omega(f^{eq} - f), \tag{2.1.1}$$

where f now relaxes towards f^{eq} with a single relaxation time $\tau_f = 1/\omega$ where ω is the collision frequency. This gives rise to the LBGK equation

$$f_i(\mathbf{x} + \mathbf{c}_i\Delta t, t + \Delta t) - f_i(\mathbf{x}, t) = -\frac{1}{\tau_f}(f_i(\mathbf{x}, t) - f_i^{eq}(\mathbf{x}, t)). \tag{2.1.2}$$

From the study of the literature we see that the lattice form of the BGK is the most commonly used collision operator due to the ease with which it can be implemented. However due to the use of a single relaxation time the method does suffer from stability issues unless $0 < \tau_f < 2$. Since there is a single relaxation time it means that the bulk ν' and kinematic ν viscosities are linearly proportional [23]. The use of a single relaxation time means that heat transfer takes place at the same rate as momentum transfer. Therefore the Prandtl number is always unity and so the LBGK equation is only appropriate for isothermal flows.

Multiple Relaxation Time (MRT)

The lattices commonly used in applications contain more distribution functions than necessary to reproduce the fluid density, momentum, and stress that appear in the Navier-Stokes equations. The additional degrees of freedom are required for isotropy, but are detrimental to stability. A Multiple-Relaxation-Time (MRT) or matrix collision operator is constructed to over-relax the stress alone. The remaining variables (non physical) are damped towards equilibrium, leading to substantial gains in stability.

MRT collision schemes are applied to the moments for each lattice point rather than the distribution functions [49, 56]. The moments and distribution functions which are related to each other by

$$\mathbf{M} = T\mathbf{f} \tag{2.1.3}$$

where $\mathbf{f}$ is a vector of all m distribution functions for the point, i.e. $(f_0, f_1, ..., f_8)^\dagger$, $\mathbf{M}$ the vector of moments (also the size of the number of discrete lattice speeds and dependent on the lattice system) and T the transformation matrix that renders the moments in terms of the distribution functions. Equilibrium values for the moments $\mathbf{M}^{eq}$, can be determined by transforming the standard local equilibrium functions into moment space by

$$\mathbf{M}^{eq} = T\mathbf{f}^{eq}, \tag{2.1.4}$$

where $\mathbf{f}^{eq}$ is the vector of local equilibrium distribution functions. The resulting equilibrium moments can alternatively be expressed directly as functions of

fluid density and velocity. Certain moments, such as density and momentum, must be conserved and their equilibrium values are set so that no changes are made. The post-collisional moments are determined by relaxation of the non-equilibrium part, i.e.

$$\mathbf{M}(\mathbf{x}, t + \Delta t) = \mathbf{M}(\mathbf{x}, t) - \Lambda(\mathbf{M}(\mathbf{x}, t) - \mathbf{M}^{eq}(\mathbf{x}, t)) \tag{2.1.5}$$

where Λ is the collision matrix, which takes the form of a diagonal matrix of collision parameters (again the same size as the number of discrete velocities of the lattice used), which we represent by the vector $\mathbf{s}$ so that

$$\Lambda = diag(\mathbf{s}). \tag{2.1.6}$$

Some of the collision parameters can be specified to set both kinematic and bulk viscosities, a few others can be tuned to improve simulation stability and the remainder are fixed (as previously stated) to conserve macroscopic hydrodynamics. Setting all the values of $\mathbf{s}$ (the diagonal entries of Λ) to $\frac{1}{\tau_f}$ reduces the scheme to the BGK single relaxation time collision model.

Since the collision matrix is diagonal, equation (2.1.5) can be rewritten in terms of each moment, i.e.

$$\mathbf{M}_i(\mathbf{x}, t + \Delta t) = \mathbf{M}_i(\mathbf{x}, t) - s_i(\mathbf{M}_i(\mathbf{x}, t) - \mathbf{M}_i^{eq}(\mathbf{x}, t) \tag{2.1.7}$$

Multiplying $\mathbf{M}_i(\mathbf{x}, t + \Delta t)$ by the inverse of the transformation matrix, T^{-1}, gives the post-collisional distribution functions.

An example is given for the D2Q9 lattice system; the moment vector is

$$\mathbf{M} = (\rho, e, \epsilon, j_x, q_x, j_y, q_y, p_{xx}, p_{xy})^{\dagger} \tag{2.1.8}$$

with ρ as the density, e the energy, ϵ the square of energy, $\mathbf{j}$ momentum, $\mathbf{q}$ energy flux, p_{xx} the diagonal stress tensor component and p_{xy} the off-diagonal stress tensor component. The transformation matrix is

$$T = \begin{pmatrix} 1 & 1 & 1 & 1 & 1 & 1 & 1 & 1 & 1 \\ -4 & 2 & -1 & 2 & -1 & 2 & -1 & 2 & -1 \\ 4 & 1 & -2 & 1 & -2 & 1 & -2 & 1 & -2 \\ 0 & -1 & -1 & -1 & 0 & 1 & 1 & 1 & 0 \\ 0 & -1 & 2 & -1 & 0 & 1 & -2 & 1 & 0 \\ 0 & 1 & 0 & -1 & -1 & -1 & 0 & 1 & 1 \\ 0 & 1 & 0 & -1 & 2 & -1 & 0 & 1 & -2 \\ 0 & 0 & 1 & 0 & -1 & 0 & 1 & 0 & -1 \\ 0 & -1 & 0 & 1 & 0 & -1 & 0 & 1 & 0 \end{pmatrix}$$

The equilibrium moment vector is

$$\mathbf{M}^{eq} = \left(\rho, -2\rho + \frac{3(j_x^2 + j_y^2)}{\rho}, w_\epsilon \rho + w_{\epsilon j}\frac{(j_x^2 + j_y^2)}{\rho}, j_x, -j_x, j_y, -j_y, \frac{j_x^2 - j_y^2}{3\rho}, \frac{j_x + j_y}{3\rho}\right)^\dagger$$

with w_ϵ and $w_{\epsilon j}$ as adjustable parameters: for convergence to the single relaxation time BGK scheme, these are set equal to 1 and -3 respectively. Of the 9 collision parameters available, s_0, s_3 and s_5 have no effect (except when applying external forces, when they should be set equal to one) as the associated moments are preserved and s_2, s_4 and s_6 are tuneable parameters for calculational stability with the condition that $s_4 = s_6$. Lallemand and Luo [56] state that one can keep values of these three relaxation parameters only slightly larger than 1 such that the corresponding kinetic modes are well separated from those modes more directly affecting hydrodynamic transport. The remaining parameters represent the viscosities of the fluid, i.e.

$$\nu = \frac{1}{3}\left(\frac{1}{s_7} - \frac{1}{2}\right)\frac{(\Delta x)^2}{\Delta t} = \frac{1}{3}\left(\frac{1}{s_8} - \frac{1}{2}\right)\frac{(\Delta x)^2}{\Delta t} = \frac{1}{3}\left(\tau_f - \frac{1}{2}\right)\frac{(\Delta x)^2}{\Delta t}$$
$$\nu' = \frac{1}{6}\left(\frac{1}{s_1} - \frac{1}{2}\right)\frac{(\Delta x)^2}{\Delta t} = \frac{1}{6}\left(\tau_{bulk} - \frac{1}{2}\right)\frac{(\Delta x)^2}{\Delta t}$$

so that $\tau = \frac{1}{s_7} = \frac{1}{s_8}$ and $\tau_{bulk} = \frac{1}{s_1}$.

2.2 Propagation Algorithm

The simplest implementation involves the use of a temporary array to copy post-collisional distribution functions to their new positions, which are subsequently copied back to the main distribution function array. This method is clear, easy to understand and can be applied throughout the system's lattice points in any order, its drawbacks include the use of two loops for propagation and array copying, two large arrays for distribution functions at each lattice node and significant amounts of time expended in memory access.

An alternative, more memory efficient implementation of propagation is the swap algorithm detailed in [68], in which this process is performed by the systematic swapping of pairs of collided distribution function values. To make this easier to implement, the lattice links are organised so that the conjugate link j to link i (i.e. $\mathbf{c}_j = -\mathbf{c}_i$) is equal to $i + \frac{m-1}{2}$ for $i = 1, \ldots, \frac{m-1}{2}$ (where m is number of discrete velocities of the lattice model). Looping i between 1 and $\frac{m-1}{2}$ the post-collisional distribution functions for each lattice point $f_i(\mathbf{x})$ are initially swapped with their conjugate values $f_j(\mathbf{x})$, then at each point the value $f_j(\mathbf{x})$ is then swapped with $f_i(\mathbf{x} + \mathbf{c}_i \Delta t)$.

These sets of swaps can be carried out either in two separate steps or in one go. The use of separate swap steps requires two sweeps through the domain, but the order in which distribution functions are swapped does not matter and no boundary domain is necessary for serial calculations. Simultaneous swapping cannot make use of automatic periodic boundary conditions and requires lattice links to be additionally ordered so that the first half are directed to lattice points that have previously gone through at least the first swap stage, but only a single sweep through the domain is required.

The two array method when implemented efficiently could be significantly faster on modern computer architectures as there are fewer read and writes to memory which for large systems can take a significant time. There is a trade off between speed and memory usage and this may depend on the particular application.

2.3 Boundary Conditions

To apply boundary conditions to a Lattice Boltzmann Equation simulation, the distribution functions f_i at boundary lattice points have to be modified or replaced during each time step to give the required fluid velocity or pressure. This may take place either between the collision and propagation stages or at the end of each time step. The easy implementation of boundary conditions is a massive advantage for LBM, making LBM an ideal numerical method for the simulation of fluid flows in complicated geometries, such as flow through porous media. Here are some examples of simple boundary conditions.

Periodic

Periodic boundaries are used to simulate bulk fluids sufficiently far away from the actual boundaries of a real physical system so that surface effects can be neglected. As the fluid moves out of one face of the system volume it reappears on the opposite face with the same velocity, density etc.

Bounce-back

This boundary condition evolved from the bounce back condition of LGCA. The bounce-back condition applies a no-slip condition at a boundary. This is applied after the propagation stage by reversing the distribution functions sitting on each wall node $\mathbf{x}_w$, i.e.

$$f_i(\mathbf{x}_w, t) = f_j(\mathbf{x}_w, t) \tag{2.3.1}$$

where j is the conjugate lattice link to i, i.e. $\mathbf{c}_j = -\mathbf{c}_i$. The reflection of distribution functions occurs on-grid and this is shown in Figure 2.3.1. On-grid bounce-back is a first order approximation of the boundary condition (error is proportional to lattice spacing), but it is completely local.

Ziegler [105] realised that a second-order bounce back scheme can be used if the boundary lies between two lattice grid lines and this is illustrated in Figure 2.3.2. This method essentially applies the actual reflection halfway between timesteps and is a spatially second-order method.

The bounce-back condition is accurate and easy to implement when the

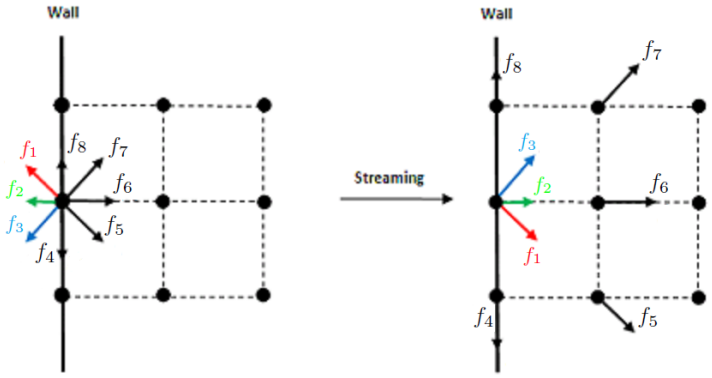

Figure 2.3.1: Illustration of on-grid bounce-back

boundary lines up with the lattice [84]. However, in general, this is not the case. Curved boundaries can be approximated with staircase-like lattices, leading to discontinuities which cause larger numerical errors as the Reynolds number increases. To overcome this, it is common to use interpolation. However, this adds complexity and the resulting method loses simplicity and efficiency.

Constant pressure/velocity

To specify either velocity or density (pressure) at planar boundaries the Zou-He method [106] can be used. This is based upon applying the bounce-back rule to the non-equilibrium distribution functions,

$$f_i^{(1)}(\mathbf{x}_w, t) = f_j^{(1)}(\mathbf{x}_w, t) \tag{2.3.2}$$

where $f_i^{(1)} = f_i - f_i^{eq}$. This function can be used to determine the missing wall velocity or density along with the known distribution function values. For instance, for a left edge with a known velocity $\mathbf{u}_w$ using the D2Q9 lattice scheme, after streaming f_0, f_1, f_2, f_3, f_4 and f_8 are known. We need to determine f_5, f_6, f_7 and ρ (see Figure 2.3.3).

The idea of Zou-He boundary conditions is to formulate the unknown distribution functions, f_5, f_6, f_7 and ρ using the moment formulae for the density

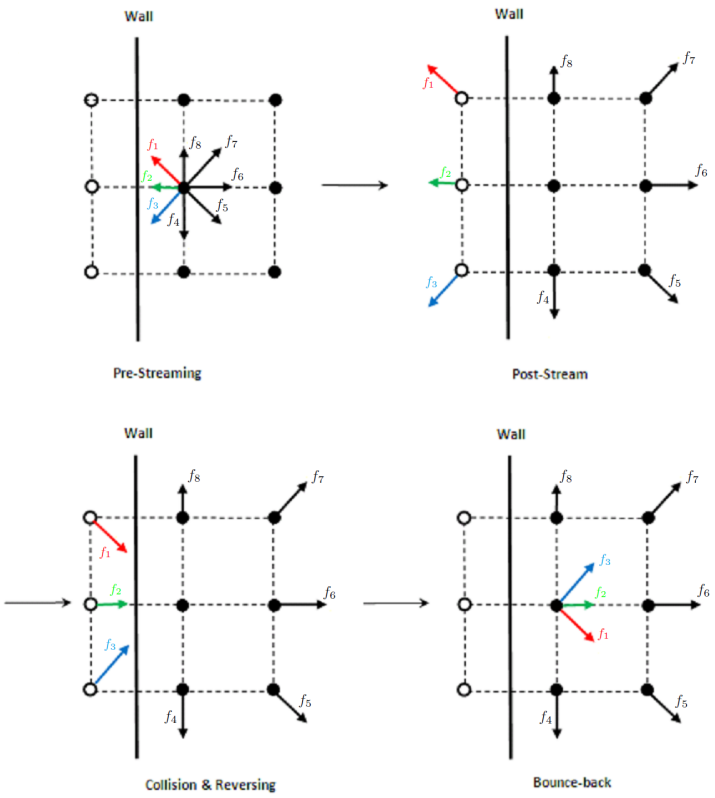

Figure 2.3.2: Illustration of mid-grid bounce back

and the momentum. Rearranging the moment formulae gives

$$f_5 + f_6 + f_7 = \rho - (f_0 + f_1 + f_2 + f_3 + f_4 + f_8) \tag{2.3.3}$$

$$f_5 + f_6 + f_7 = \rho u_{w,x} + (f_2 + f_1 + f_3) \tag{2.3.4}$$

$$f_7 - f_5 = \rho u_{w,y} - f_8 + f_4 - f_1 + f_3 \tag{2.3.5}$$

Using (2.3.3) and (2.3.4) we can determine

$$\rho_w = \frac{f_0 + f_4 + f_8 + 2(f_1 + f_2 + f_3)}{1 - u_{w,x}} \tag{2.3.6}$$

To solve for f_5, f_6 and f_7 we need to close the system for which we require a fourth equation. The assumption made by Zou-He [106] is that the bounce-back rule still holds for the non-equilibrium part of the particle distribution

normal to the boundary. In this case, the fourth equation is

$$f_6 - f_6^{eq} = f_2 - f_2^{eq} \tag{2.3.7}$$

With f_6 determined, f_5 and f_7 are subsequently calculated using

$$\begin{aligned} f_6 &= f_2 + \frac{2\rho_w v_{w,y}}{3} \\ f_7 &= f_3 - \frac{1}{2}(f_8 - f_4) + \frac{1}{6}\rho_w u_{w,x} + \frac{1}{2}\rho_w u_{w,y} \\ f_5 &= f_1 + \frac{1}{2}(f_8 - f_4) + \frac{1}{6}\rho_w u_{w,x} - \frac{1}{2}\rho_w u_{w,y} \end{aligned}$$

The other form, specifying the wall fluid density, requires the calculation of the wall velocity, which can be simplified by setting non-orthogonal velocity components to zero. For the analogous example at the top wall for D2Q9, the same equations for f_3, f_4 and f_5 can be used together with

$$\begin{aligned} \rho_w u_{w,y} &= 0, \\ \rho_w u_{w,x} &= f_0 + f_2 + f_6 + 2(f_1 + f_7 + f_8) - \rho_w. \end{aligned}$$

One complication for three-dimensional lattices is the requirement to apply the non-equilibrium bounce-back to all unknown distribution functions, which ordinarily over-specifies the system but can be counteracted using transverse momentum corrections for directions other than orthogonal to the boundary, which are non-zero for e.g. shearing flows. It should be noted that if the wall velocity is set to zero, the boundary condition reduces to on-grid bounce-back.

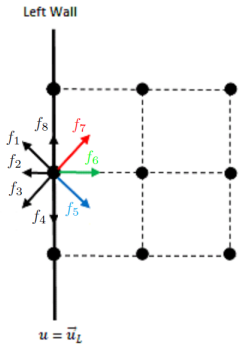

Figure 2.3.3: Illustration of Zou-He velocity BC

2.4 Body Forces

To incorporate a body force such as a pressure force or gravity there are two many options which both give accurate results. Either external forces are dealt with by adding $\frac{\tau \mathbf{F}}{\rho}$ to the velocity of the fluid when calculating the equilibrium distribution function f_i^{eq} [67], or by adding a forcing term to the collisional distribution function [37]

$$F_i = \left(1 - \frac{1}{2\tau_f} w_i\right) \left[\frac{\mathbf{c}_i - \mathbf{v}}{c_s^2} + \frac{\mathbf{c}_i - \mathbf{v}}{c_s^4} \mathbf{c}_i\right] \cdot \mathbf{F} \tag{2.4.1}$$

where $\mathbf{v}$ is defined to be $\mathbf{u} + \frac{\Delta t}{2\rho}\mathbf{F}$ and is also used in calculating the equilibrium distribution function. This second method is by Guo et al. [37] has been shown to recover the correct continuity and moment equations. Mohamad and Kusmin [70] show that adding a forcing term to the collisional distribution function is the more accurate, however, for small values of viscosity either scheme predicts the same results. Due to the ease of adding a forcing term to the collisional distribution function that is the recommended way of incorporating a body force in LBM.

2.5 Numerical Results

To demonstrate the LBM we present some numerical results to illustrate the effects of using different boundary conditions and different underlying lattices.

Poiseuille Channel Flow

Here we present the classic Poiseuille channel flow in order to highlight the differences between mid-grid and on-grid bounce back conditions in terms of accuracy of the velocity profile. A single fluid is modelled on a 42×42 grid using fixed density boundary conditions on the left and right boundaries to represent a pressure drop across the system, which is bounded by solid walls at the top and bottom. The solid walls are modelled with both the on-grid bounce back condition and the mid-grid bounce back condition. This generates a pressure-driven (Poiseuille) laminar flow with a parabolic velocity profile

which we can compare with the analytic solution

$$u(y) = \frac{1}{2\mu}\left(-\frac{dp}{dx}\right) y(h-y) \tag{2.5.1}$$

where h is the width of the channel, μ is the dynamic viscosity and $\frac{dp}{dx}$ is the pressure gradient. The plot of the numerical and analytic velocity profiles for the on-grid bounce back condition shows good agreement in the centre of the channel but has errors near the walls. The velocity is normalised so that the maximum velocity is unity. The mid-grid bounce back condition has a much smaller error compared with the analytic solution. This is shown in Fig 2.5.3 where the root mean square error has been calculated using

$$Err = \sqrt{\frac{1}{N}\sum_{i=1}^{N} |u_{lbm} - u_{analytic}|^2} \tag{2.5.2}$$

where N is the number of lattice sites. Fig 2.5.3 indicates that the convergence for the standard bounce back scheme is only first order compared to the mid-grid bounce back scheme which has second order convergence.

Couette Flow

In order to demonstrate LBM on the D2Q7 lattice we present numerical solutions for Couette flow. Here we have a stationary bottom plate, a top plate moving with a constant velocity U and periodic boundary conditions on the left and right walls of the domain. This has an exact solution in the steady state

$$u(y) = U\frac{y}{h}. \tag{2.5.3}$$

The calculations were performed on a 50×50 grid and what we can see from Figures 2.5.4 and 2.5.5 is that they both give very good agreement with the analytical solution with root square errors of 6.87×10^{-09} and 3.50×10^{-17}, respectively.

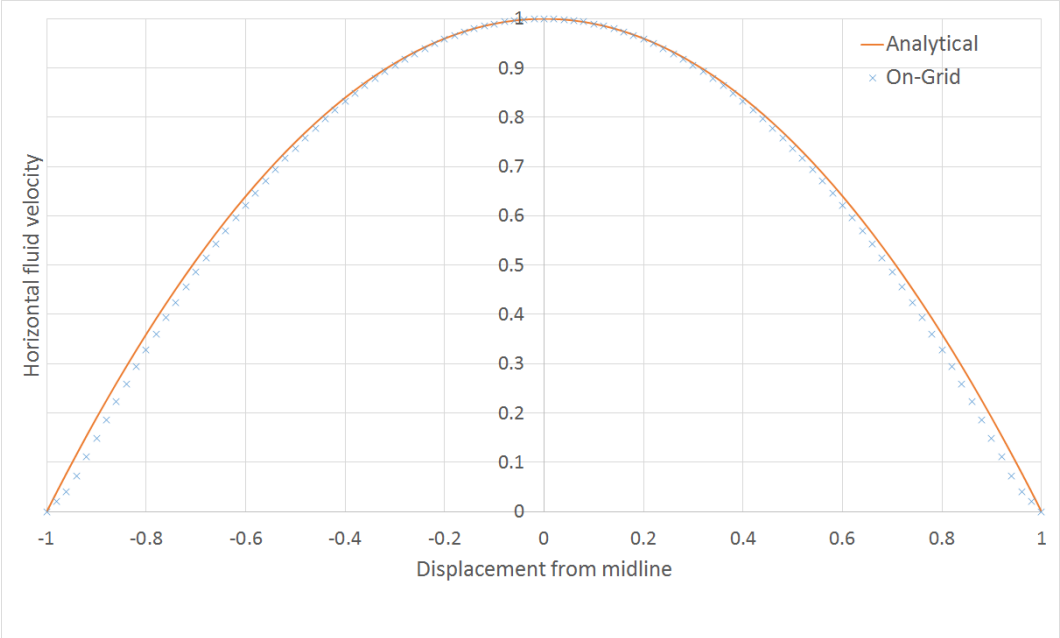

Figure 2.5.1: Normalised velocity profiles for Poiseuille flow with on-grid bounce back condition with $\omega = 1.25$

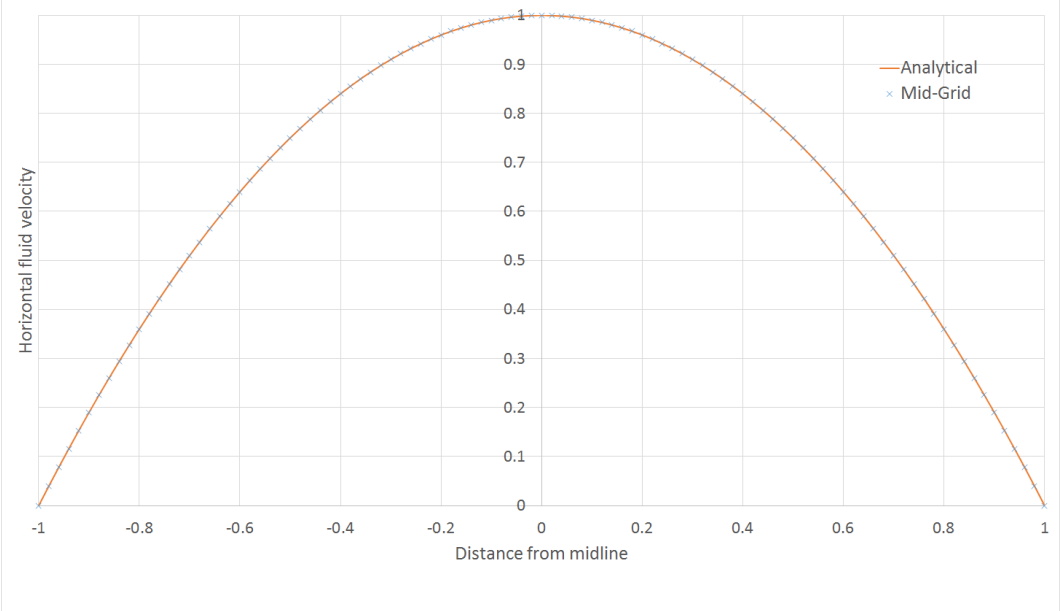

Figure 2.5.2: Normalised velocity profiles for Poiseuille flow with mid-grid bounce back condition with $\omega = 1.25$

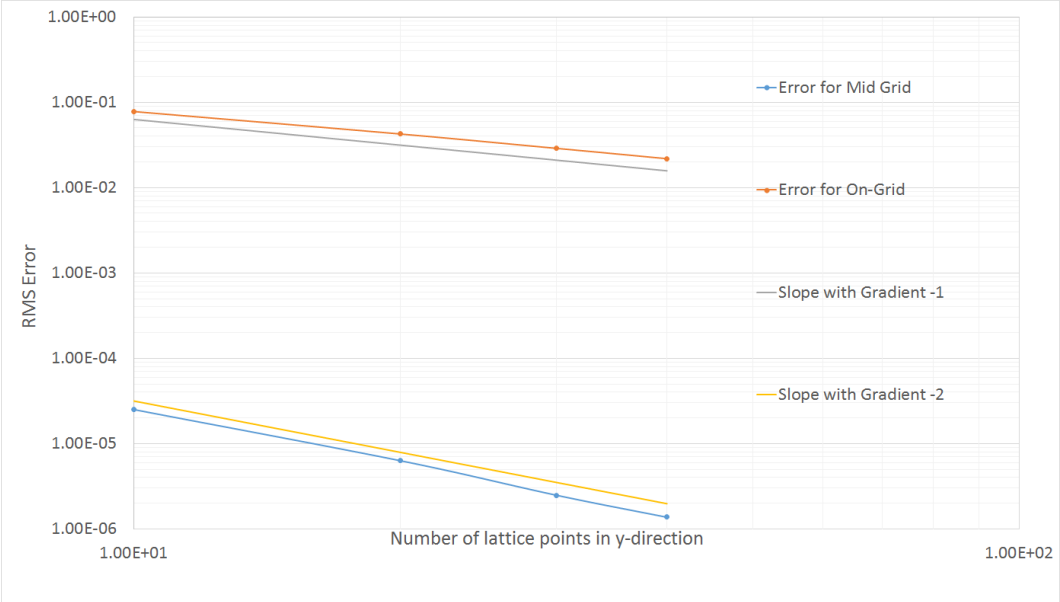

Figure 2.5.3: Comparison between the root mean square error for the mid-grid and on-grid bounce back boundary conditions with $\omega = 1.25$.

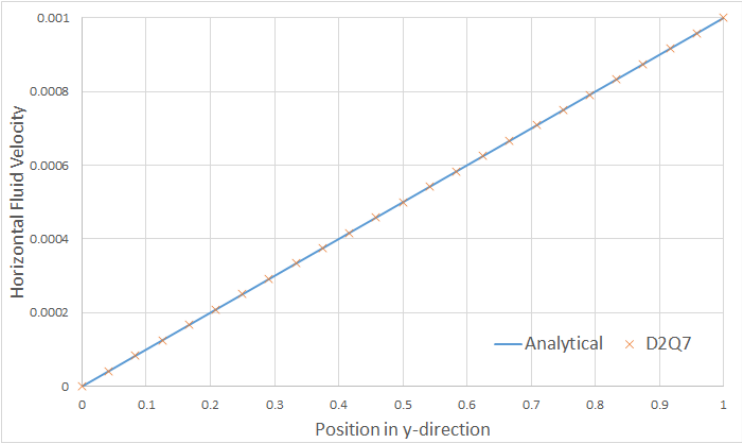

Figure 2.5.4: Couette Flow on the D2Q7 lattice, horizontal velocity profile, $\omega = 1$

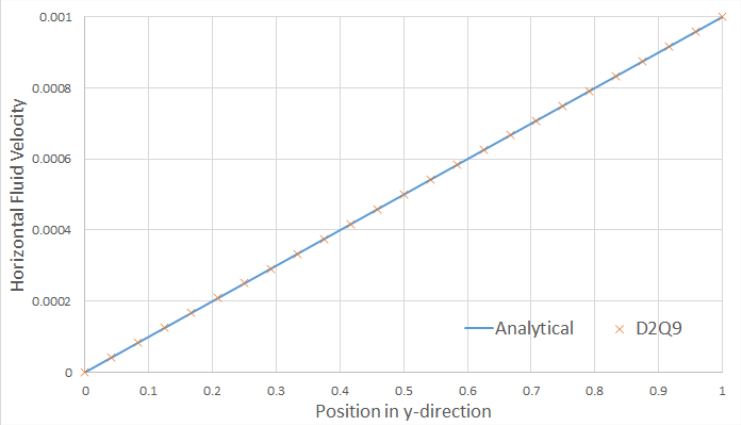

Figure 2.5.5: Couette Flow on the D2Q9 lattice, horizontal velocity profile, $\omega = 1$

2.6 Discussion

In this Chapter we have discussed the implementation of the LBM. What has been demonstrated is the ease of implementation for a wide variety of flow scenarios. We started by examining different collision operators used such as BGK and MRT. The BGK operator is the most widely used do to the ease of implementation but the MRT has significant advantages due to the increase in stability of the method. The propagation algorithm used can make a significant difference to the computational efficiency of the LBM especially when it is used to solve large problems. The choice of propagation algorithm is therefore informed by the nature of your computational architecture. Since the major advantage of using LBM over macroscopic solvers is the ease of implementing boundary conditions, different boundary conditions have been discussed and results have been presented demonstrating the advantages of using the mid-grid bounce back over the on-grid bounce back.

Chapter 3

Lattice Boltzmann Theory

Although the Lattice Boltzmann Method was developed from the Lattice Gas Cellular Automata, it can be derived independently. Understanding how to construct the LBM for solving the Navier-Stokes equations using a D2Q9 lattice is important if we want to construct Lattice Boltzmann style solvers for other equations such as the Fokker-Planck equation which is used in the modelling of a particle under the influence of drag forces and random forces as in Brownian motion or for developing Lattice Boltzmann solvers for non-isothermal flow in which higher order schemes are necessary for thermodynamic consistency. In this chapter we look at how to derive the Lattice Boltzmann equation from the continuous Boltzmann equation,the derivation of the equilibrium distribution function for the Lattice Boltzmann Equation and how the Lattice Boltzmann Equation is able to reproduce the physics of the Navier-Stokes equations.

3.1 From the Continuum Boltzmann Equation to the Lattice Boltzmann Equation

Although as discussed previously, lattice Boltzmann equations were first considered as empirical extensions of the earlier lattice gas celluar automata (LGCA), they may be derived systematically by truncating the continuum Boltzmann equation in velocity space [42, 66, 1]. We consider the continuum

Boltzmann BGK equation

$$\partial_t f + \boldsymbol{\xi} \cdot \nabla f = -\frac{1}{\tau}(f - f^{eq}) \tag{3.1.1}$$

with the Maxwell-Boltzmann equilibrium distribution function

$$f^{eq} = \frac{\rho}{(2\pi RT)^{D/2}} \exp\left(-\frac{(\boldsymbol{\xi} - \mathbf{u})^2}{2RT}\right), \tag{3.1.2}$$

where the macroscopic variables are determined from the moments of the distribution function

$$\rho(\mathbf{x}, t) = \int f(\mathbf{x}, \boldsymbol{\xi}, t) d\boldsymbol{\xi}, \tag{3.1.3}$$

$$\rho(\mathbf{x}, t)\mathbf{u}(\mathbf{x}, t) = \int \boldsymbol{\xi} f(\mathbf{x}, \boldsymbol{\xi}, t) d\boldsymbol{\xi}, \tag{3.1.4}$$

$$\rho(\mathbf{x}, t)e(\mathbf{x}, t) = \int (\boldsymbol{\xi} - \mathbf{u})^2 f(\mathbf{x}, \boldsymbol{\xi}, t) d\boldsymbol{\xi}, \tag{3.1.5}$$

where ρ is the fluid density, $\mathbf{u}$ is the fluid velocity and e is the internal energy, the energy contained within the system excluding the kinetic and potential energy of the system as a whole. Using a Taylor expansion on the equilibrium equation (3.1.2) up to u^2 we obtain

$$f^{eq} = \frac{\rho}{(2\pi RT)^{D/2}} \exp\left(-\frac{\boldsymbol{\xi}^2}{2RT}\right)\left(1 + \frac{\boldsymbol{\xi} \cdot \mathbf{u}}{RT} + \frac{(\boldsymbol{\xi} \cdot \mathbf{u})^2}{2(RT)^2} - \frac{\mathbf{u}^2}{2RT}\right) + \mathcal{O}(\mathbf{u}^3). \tag{3.1.6}$$

In order to derive the Navier-Stokes equations, the following moment integral must be evaluated exactly

$$\int \boldsymbol{\xi}^m f^{eq} d\boldsymbol{\xi}, \tag{3.1.7}$$

where $0 \leq m \leq 3$ for isothermal models [42]. The truncated equilibrium function has the form

$$f^{eq} = \exp\left(-\frac{\boldsymbol{\xi}^2}{2RT}\right) p(\boldsymbol{\xi}) \tag{3.1.8}$$

where p is a polynomial in $\boldsymbol{\xi}$ and so as He and Luo [42] realised these integrals may be evaluated as sums using Gauss-Hermitian quadrature formulae,

$$I = \int \boldsymbol{\xi}^m \exp\left(-\frac{\boldsymbol{\xi}^2}{2RT}\right) p(\boldsymbol{\xi}) d\boldsymbol{\xi} = \sum_{i=0} W_i \exp\left(-\frac{\boldsymbol{\xi}_i^2}{2RT}\right) p(\boldsymbol{\xi}_i), \tag{3.1.9}$$

where W_i and $\boldsymbol{\xi}_i$ are the weights and abscissae of the quadrature respectively.

Since the only values of the distribution function as evaluated at the abscissae need to be evolved in $\mathbf{x}$ and t, these values are sufficient to evaluate the required moments. Thus the continuum Boltzmann BGK equation may be replaced by the lattice Boltzmann BGK equation, [23]

$$\partial_t f_i + \boldsymbol{\xi}_i \cdot \nabla f_i = -\frac{1}{\tau}(f_i - f_i^{eq}), \quad \text{for } i = 0, \ldots, N \tag{3.1.10}$$

where

$$f_i(\mathbf{x}, t) = \frac{W_i f(\mathbf{x}, \boldsymbol{\xi}_i, t)}{\exp\left(-\frac{\boldsymbol{\xi}^2}{2RT}\right)}. \tag{3.1.11}$$

Accordingly, the macroscopic variables can be computed by quadrature as well

$$\rho(\mathbf{x}, t) = \sum_i f_i(\mathbf{x}, \boldsymbol{\xi}_i, t), \tag{3.1.12}$$

$$\rho(\mathbf{x}, t)\mathbf{u}(\mathbf{x}, t) = \sum_i \boldsymbol{\xi}_i f_i(\mathbf{x}, \boldsymbol{\xi}_i, t), \tag{3.1.13}$$

$$\rho(\mathbf{x}, t)e(\mathbf{x}, t) = \sum_i (\boldsymbol{\xi}_i - \mathbf{u})^2 f_i(\mathbf{x}, \boldsymbol{\xi}_i, t). \tag{3.1.14}$$

To derive the previously mentioned D2Q9 model, a Cartesian coordinate system is used. We set $p(\boldsymbol{\xi}) = \xi_x^m \xi_y^n$ and the integral of equation (3.1.9) becomes

$$I = (\sqrt{2RT})^{m+n+2} I_m I_n, \tag{3.1.15}$$

where

$$I_m = \int_{-\infty}^{+\infty} \exp(-z^2) z^m dz \tag{3.1.16}$$

where $z = \xi_x/\sqrt{2RT}$ or $z = \xi_y/\sqrt{2RT}$. Evaluating I_m using Gauss-Hermitian quadrature the three abscissae z_j and the corresponding weights ω_j of the

quadrature are

$$z_1 = -\sqrt{3/2}, \quad z_2 = 0, \quad z_3 = \sqrt{3/2}, \tag{3.1.17}$$

$$\omega_1 = \sqrt{\pi}/6, \quad \omega_2 = 2\sqrt{\pi}/3, \quad \omega_3 = \sqrt{\pi}/6, \tag{3.1.18}$$

then the integral I becomes

$$I = 2RT\left[\omega_2^2 p(0) + \sum_{i=1}^{4} \omega_1\omega_2 p(\boldsymbol{\xi}_i) + \sum_{i=5}^{8} \omega_1^2 p(\boldsymbol{\xi}_i)\right], \tag{3.1.19}$$

where $\boldsymbol{\xi}_i$ is the zero velocity vector for $i = 0$, the vectors of $\sqrt{3RT}(\pm 1, 0)$ and $\sqrt{3RT}(0, \pm 1)$ for $i = 1, \ldots, 4$ and vectors of $\sqrt{3RT}(\pm 1, \pm 1)$ for $i = 5, \ldots, 8$. To obtain the D2Q9 isothermal model we choose $\sqrt{3RT} = c$ where c is the ratio the lattice spacing to lattice time step. Thus by comparing equations (3.1.9) and (3.1.19), we can identify the weights defined in (3.1.9)

$$W_i = 2\pi RT \exp(\boldsymbol{\xi}_i^2/2RT) w_i, \tag{3.1.20}$$

where

$$w_i = \begin{cases} 4/9, & i = 0 \\ 1/9, & i = 1, \ldots, 4 \\ 1/36, & i = 5, \ldots, 8. \end{cases} \tag{3.1.21}$$

The discrete equilibrium distribution functions are

$$f_i^{eq} = w_i \rho \left\{1 + \frac{3(\mathbf{c}_i \cdot \mathbf{u})}{c^2} + \frac{9(\mathbf{c}_i \cdot \mathbf{u})^2}{2c^4} - \frac{3\mathbf{u}^2}{2c^2}\right\}. \tag{3.1.22}$$

In order to fully disretise the lattice Boltzmann equation we must approximate (3.1.10) in time and space. Integrating (3.1.10) along a characteristic for a time interval Δt we obtain

$$f_i(\mathbf{x} + \boldsymbol{\xi}_i \Delta t, t + \Delta t) - f_i(\mathbf{x}, t) = -\frac{1}{\tau}\int_0^{\Delta t} f_i(\mathbf{x} + \boldsymbol{\xi}_i s, t + s) - f^{eq}(\mathbf{x} + \boldsymbol{\xi}_i s, t + s) ds. \tag{3.1.23}$$

If we approximate this integral by the trapezium rule, we have

$$\begin{aligned} &f_i(\mathbf{x}+\boldsymbol{\xi}_i\Delta t, t+\Delta t) - f_i(\mathbf{x},t) \\ &= -\frac{\Delta t}{2\tau}(f_i(\mathbf{x}+\boldsymbol{\xi}_i\Delta t, t+\Delta t) - f_i^{eq}(\mathbf{x}+\boldsymbol{\xi}_i\Delta t, t+\Delta t) + f_i(\mathbf{x},t) - f_i^{eq}(\mathbf{x},t)) \end{aligned} \tag{3.1.24}$$

which unfortunately is implicit. Using a change of variables first suggested by He et al. [43]

$$\bar{f}_i(\mathbf{x}',t') = f_i(\mathbf{x}',t') + \frac{\Delta t}{2\tau}(f_i(\mathbf{x}',t') - f_i^{eq}(\mathbf{x}',t')) \tag{3.1.25}$$

the implicit system can be recast in the explicit form

$$\bar{f}_i(\mathbf{x}+\boldsymbol{\xi}_i\Delta t, t+\Delta t) - \bar{f}_i(\mathbf{x},t) = -\frac{\Delta t}{\tau+\Delta t/2}(\bar{f}_i(\mathbf{x},t) - f_i^{eq}(\mathbf{x},t)). \tag{3.1.26}$$

The macroscopic density, momentum and momentum flux are readily reconstructed from moments of the $\bar{f}_i$

$$\rho(\mathbf{x},t) = \sum_i \bar{f}_i(\mathbf{x},\boldsymbol{\xi}_i,t), \tag{3.1.27}$$

$$\rho(\mathbf{x},t)\mathbf{u}(\mathbf{x},t) = \sum_i \boldsymbol{\xi}_i \bar{f}_i(\mathbf{x},\boldsymbol{\xi}_i,t), \tag{3.1.28}$$

$$\left(1+\frac{\Delta t}{2\tau}\right)\boldsymbol{\Pi} = \sum_{i=0} \boldsymbol{\xi}_i\boldsymbol{\xi}_i\bar{f}_i + \frac{\Delta t}{2\tau}\boldsymbol{\Pi}^{eq}. \tag{3.1.29}$$

It should be noted that this formulation is equivalent to the usual construction based on a Taylor expansion of the discrete equation where second order accuracy may be achieved with what looks like only a first order approximation to (3.1.10), by replacing the relaxation time τ with $\tau + \Delta t/2$ [17]. The variables often denoted f_i appearing in the discrete system are actually the $\bar{f}_i$ in our notation, so that the non-equilibrium momentum flux $\boldsymbol{\Pi}^{(1)}$ in the fully discrete system (3.1.26) is given by

$$\boldsymbol{\Pi}^{(1)} = \frac{\bar{\boldsymbol{\Pi}} - \boldsymbol{\Pi}^{eq}}{1+\Delta t/(2\tau)}, \tag{3.1.30}$$

rather than by $\boldsymbol{\Pi} - \boldsymbol{\Pi}^{eq}$ as in the continuous system.

3.2 Derivation of the Equilibrium Distribution Function

There are two methods by which the local equilibria for the Lattice Boltzmann Equation can be constructed. The bottom-up method obtains the equilibrium from the Maxwell-Boltzmann equilibrium distribution. The top-down method constructs the equilibrium so that the required macroscopic properties can be reproduced.

Equilibrium from the Maxwell-Boltzmann equilibrium distribution

The equilibrium distribution f^{eq} is given by

$$f^{eq} = \frac{\rho}{(2\pi\theta)^{D/2}} e^{-(\mathbf{v}-\mathbf{u})^2/2\theta} \tag{3.2.1}$$

where $\theta = c_s^2 = kT/m$ is the scaled temperature, k is the Boltzmann constant, T is the fluid temperature, $\mathbf{v}$ is the microscopic velocity, $\mathbf{u}$ is the mean fluid velocity, D is the space dimension, and m is the mass of the particle. The parameter c_s is the speed of sound in a gas close to equilibrium described by f^{eq}.

When $|\mathbf{v} - \mathbf{u}| \ll \sqrt{\theta}$, the equilibrium distribution can be expanded and approximated by

$$f^{eq} = \frac{\rho}{(2\pi\theta)^{D/2}} \exp\left(-\frac{v^2}{2\theta}\right)\left[1 + \frac{\mathbf{v}\cdot\mathbf{u}}{\theta} + \frac{(\mathbf{v}\cdot\mathbf{u})^2}{2\theta^2} - \frac{u^2}{2\theta}\right] \tag{3.2.2}$$

For a microscopic quantity $\psi(\mathbf{v})$, the associated macroscopic quantity Ψ is calculated by

$$\Psi = \int \psi(\mathbf{v}) f^{eq} d\mathbf{v} \tag{3.2.3}$$

Let $\mathbf{v} = \sqrt{2\theta}\mathbf{c}$, where $\mathbf{c}$ is a rescaled thermal velocity; the macroscopic velocity $\mathbf{u}$ can be similarly rescaled to $\sqrt{2\theta}\tilde{\mathbf{u}}$. Equations (3.2.2) and (3.2.3) can thus be combined to give

$$\Psi = \int e^{-c^2} \psi(c) \frac{\sqrt{2\theta}\rho}{(2\pi\theta)^{D/2}} \left[1 + 2(\mathbf{c}\cdot\tilde{\mathbf{u}}) + (\mathbf{c}\cdot\tilde{\mathbf{u}})^2 - \tilde{u}^2\right] d\mathbf{c} \tag{3.2.4}$$

Using Gaussian-Hermite quadrature to approximate the integral yields

$$\Psi \simeq \sum \psi(c_i) \frac{\sqrt{2\theta}}{(2\pi\theta)^{D/2}} w(c_i) \left[1 + 2(\mathbf{c}\cdot\tilde{\mathbf{u}}) + (\mathbf{c}\cdot\tilde{\mathbf{u}})^2 - \tilde{u}^2\right] d\mathbf{c} \tag{3.2.5}$$

Let

$$w_i = \frac{\sqrt{2\theta}\rho}{(2\pi\theta)^{D/2}} w(c_i) \tag{3.2.6}$$

and

$$f_i^{eq} = w_i \rho \left[1 + 2(\mathbf{c}\cdot\tilde{\mathbf{u}}) + (\mathbf{c}\cdot\tilde{\mathbf{u}})^2 - \tilde{u}^2\right]. \tag{3.2.7}$$

The value of $w(c_i)$ can be obtained from Gauss-Hermite quadrature. Equation (3.2.7) is the equilibrium particle distribution function in the discrete regime and w_i is called the weight factor for speed vector v_i. Equation (3.2.7) can also be written in the form

$$f_i^{eq} = w_i \rho \left[1 + \frac{(\mathbf{c}_i.\mathbf{u})}{\theta} + \frac{(\mathbf{c}_i.\mathbf{u})^2}{2\theta^2} - \frac{u^2}{2\theta}\right]. \tag{3.2.8}$$

Constructing the equilibrium from the required macroscopic properties

The second way of constructing the equilibrium distribution is by starting from the macroscopic properties and solving the linear system to recover the coefficients of the equilibrium function. Here we give as an example the D2Q9 model as given by Reis [84].

The general form of the equilibrium distribution function can be written up to $\mathcal{O}(u^2)$ [15]:

$$f_i^{eq} = \rho w_i \left(A + B\mathbf{c}_i\cdot\mathbf{u} + Cu^2 + D(\mathbf{c}_i\cdot\mathbf{u})^2\right) \tag{3.2.9}$$

where A, B, C and D are constants. The weights w_i, $i = 0, \ldots, 8$ are chosen to be positive to ensure positive mass density and so that the lattice velocity moments coincide with those of the Maxwell distribution up to fourth order

i.e.

$$\sum_{i=0}^{8} w_i = 1, \tag{3.2.10}$$

$$\sum_{i=0}^{8} w_i c_{i\alpha} = 0, \tag{3.2.11}$$

$$\sum_{i=0}^{8} w_i c_{i\alpha} c_{i\beta} = \theta \delta_{\alpha\beta}, \tag{3.2.12}$$

$$\sum_{i=0}^{8} w_i c_{i\alpha} c_{i\beta} c_{i\gamma} = 0, \tag{3.2.13}$$

$$\sum_{i=0}^{8} w_i c_{i\alpha} c_{i\beta} c_{i\gamma} c_{i\delta} = \theta^2 (\delta_{\alpha\beta}\delta_{\gamma\delta} + \delta_{\alpha\gamma}\delta_{\beta\delta} + \delta_{\alpha\delta}\delta_{\gamma\beta}), \tag{3.2.14}$$

where $\delta_{\alpha\beta}$ is the Kronecker delta function and $c_{i\alpha}$ denotes the α component of the ith lattice velocity.

Using mass conservation (1.3.6)

$$\rho = \rho(A + Cu^2 + Du_\alpha u_\beta \theta \delta_{\alpha\beta}) \tag{3.2.15}$$

so we see that at 0^{th} order

$$A = 1, \tag{3.2.16}$$

and at order $\mathcal{O}(u^2)$:

$$C + D\theta = 0. \tag{3.2.17}$$

Now using momentum conservation (1.3.7)

$$B = \frac{1}{\theta}. \tag{3.2.18}$$

Defining the momentum flux tensor, $\Pi_{\alpha\beta}$, to be the second moment of the equilibrium function we find that

$$\Pi_{\alpha\beta} = \sum_{i=0}^{8} f_i^{eq} c_{i\alpha} c_{i\beta}, \tag{3.2.19}$$

$$= p_0 \delta_{\alpha\beta} + \rho u_\alpha u_\beta \tag{3.2.20}$$

where $p_0 = \theta\rho$ and we have set (at order u^2)

$$C\theta + 3D\theta^2 = 1, \tag{3.2.21}$$

and (at order $\mathcal{O}(u_\alpha u_\beta)$)

$$2D\theta^2 = 1. \tag{3.2.22}$$

A little algebra reveals that

$$B = 3, \tag{3.2.23}$$

$$C = -\frac{3}{2}, \tag{3.2.24}$$

$$D = \frac{9}{2}, \tag{3.2.25}$$

$$\theta = \frac{1}{3} \tag{3.2.26}$$

and the weights are

$$w_i = \begin{cases} \frac{4}{9} & i = 0 \\ \frac{1}{9} & i = 2, 4, 6, 8 \\ \frac{1}{36} & i = 1, 3, 5, 7. \end{cases} \tag{3.2.27}$$

Therefore, the D2Q9 equilibrium function is given by

$$f_i^{eq} = \rho w_i \left(1 + 3\mathbf{c}_i \cdot \mathbf{u} + \frac{9}{2}(\mathbf{c}_i \cdot \mathbf{u})^2 - \frac{3}{2}u^2\right) \tag{3.2.28}$$

with pressure p_0 defined by

$$p_0 = \frac{\rho}{3}. \tag{3.2.29}$$

Note that the pressure satisfies an ideal equation of state and the factor $1/3$ is the speed of sound squared, i.e. $c_s^2 = 1/3$.

A similar analysis can be performed for the D2Q7 lattice. The equilibrium for the moving particles have the general form

$$f_i^{eq} = d + \frac{\rho}{3c^2}\mathbf{c}_i \cdot \mathbf{u} + \rho\frac{2}{3c^4}(\mathbf{c}_i \cdot \mathbf{u})^2 + \gamma\mathbf{u}^2 \tag{3.2.30}$$

and the equilibrium distribution for the rest particles has the form

$$f_0^{eq} = d_0 + \gamma_0\mathbf{u}^2 \tag{3.2.31}$$

where d, d_0, γ and γ_0 are coefficients to be determined and c is the length of a lattice vector. Examining the mass conservation law we derive the following constraints

$$\rho = d_0 + 6d, \tag{3.2.32}$$

$$0 = \gamma_0 + \rho\frac{2}{c^2} + 6\gamma \tag{3.2.33}$$

and the momentum flux tensor can be expressed as

$$\Pi_{ij} = \sum_{\alpha}(\mathbf{c}_\alpha)_i(\mathbf{c}_\alpha)_j f_\alpha^{eq} = 3c^2 d\delta_{ij} + \rho u_i u_j + \left(\frac{\rho}{2} + 3c^2\gamma\right)\mathbf{u}^2\delta_{ij}, \tag{3.2.34}$$

which satisfies the requirement of Galilean invariance. It can immediately be seen that the velocity dependence of the pressure is eliminated by setting

$$\gamma = -\frac{\rho}{6c^2}. \tag{3.2.35}$$

We can then solve equation (3.2.33) to find $\gamma_0 = -\rho/c^2$. The choice of d_0 is rather arbitrary but is commonly chosen so that $d_0 = \rho_0/7$ where ρ_0 is the total number of particles divided by the total number of lattice sites. Since d_0 is a constant d is seen to be linearly dependent on the total particle density ρ with the pressure related to the total particle density having the form for an isothermal ideal gas,

$$p = c_s^2\rho. \tag{3.2.36}$$

3.3 Relation Between the Lattice Boltzmann Method and Navier-Stokes

In this chapter we show why LBM can be used to simulate fluid dynamics by showing that one can, by use of multiscale analysis (commonly referred to as the Chapman-Enskog procedure), derive the Navier-Stokes equations. Applying the BGK approximation to the collision operator we define the LBGK equation to be

$$f_i(\mathbf{x} + \mathbf{c}_i, t+1) - f_i(\mathbf{x}, t) = -\frac{1}{\tau}\left(f_i - f_i^{(0)}\right) \tag{3.3.1}$$

Expanding $f_i(\mathbf{x}+\mathbf{c}_i, t+1)$ about the point $(\mathbf{x}, t)$ and defining $f_i = f_i(\mathbf{x}, t)$ gives

$$\partial_t f_i + \mathbf{c}_{i\alpha}\partial_\alpha f_i + \frac{1}{2}\left(\partial_{tt} f_i + 2\mathbf{c}_{i\alpha}\partial_t\partial_\alpha f_i + \mathbf{c}_{i\alpha}\mathbf{c}_{i\beta}\partial_\alpha\partial_\beta f_i\right) = -\frac{1}{\tau}\left(f_i - f_i^{(0)}\right) \quad (3.3.2)$$

Now separate space and time scales as

$$\mathbf{x} = \frac{1}{\varepsilon}\mathbf{x_1}, \quad t = \frac{1}{\varepsilon}t_1 + \frac{1}{\varepsilon^2}t_2 \quad (3.3.3)$$

so that $\partial_t = \varepsilon\partial_{t_1} + \varepsilon^2\partial_{t_2}$, $\partial_x = \varepsilon\partial_{x_1}$ This means that the second-order partial derivatives are

$$\partial_{tt} = \varepsilon^2\partial_{t_1 t_1} + 2\varepsilon^3\partial_{t_1}\partial_{t_2} + \varepsilon^4\partial_{t_2 t_2} \quad (3.3.4)$$

$$\partial_{\alpha\alpha} = \varepsilon^2\partial_{\alpha_1\alpha_1} \quad (3.3.5)$$

$$\partial_t\partial_\alpha = \varepsilon^2\partial_{t_1\alpha_1} + \varepsilon^3\partial_{t_2\alpha_1} \quad (3.3.6)$$

Using these with (3.3.2) gives

$$\begin{aligned}\varepsilon\partial_{t_1} f_i + \varepsilon^2\partial_{t_2} f_i + \mathbf{c}_{i\alpha_1}\varepsilon\partial_{\alpha_1} f_i + \frac{1}{2}\left[\varepsilon^2\partial_{t_1 t_1} f_i + 2\varepsilon^3\partial_{t_1 t_2} f_i + \varepsilon^4\partial_{t_2 t_2} f_i\right.\\ \left. + 2\mathbf{c}_{i\alpha_1}\left(\varepsilon^2\partial_{t_1}\partial_{\alpha_1} f_i + \varepsilon^3\partial_{t_2}\partial_{\alpha_1} f_i\right) + \mathbf{c}_{i\alpha_1}\mathbf{c}_{i\beta_1}\varepsilon^2\partial_{\alpha_1}\partial_{\beta_1} f_i\right] = -\frac{1}{\tau}\left(f_i - f_i^{(0)}\right)\end{aligned} \quad (3.3.7)$$

Now we say that the particle distribution function departs slightly from the local equilibrium state and write

$$f_i = f_i^{(0)} + \varepsilon f_i^{(1)} + \varepsilon^2 f_i^{(2)} + \ldots \quad (3.3.8)$$

and then substitute (3.3.8) into (3.3.7) and compare coefficients of ε. At first order in ε we have

$$\partial_{t_1} f_i^{(0)} + \mathbf{c}_{i\alpha}\partial_\alpha f_i^{(0)} = -\frac{1}{\tau} f_i^{(1)} \quad (3.3.9)$$

Using mass conservation (taking moments) of (3.3.9) we obtain

$$\partial_{t_1}\rho + \partial_\alpha \rho u_\alpha = 0 \quad (3.3.10)$$

and momentum conservation yields

$$\partial_{t_1}\rho u_\alpha + \partial_\beta \Pi_{\alpha\beta} = 0. \tag{3.3.11}$$

The $\mathcal{O}(\varepsilon^2)$ terms give

$$\begin{aligned}\partial_{t_1} f_i^{(1)} + \partial_{t_2} f_i^{(0)} + \mathbf{c}_{i\alpha_1}\partial_{\alpha_1} f_i^{(1)} + \frac{1}{2}\partial_{t_1 t_1} f_i^{(0)} \\ + \mathbf{c}_{i\alpha_1}\partial_{t_1}\partial_{\alpha_1} f_i^{(0)} + \frac{1}{2}\mathbf{c}_{i\alpha_1}\mathbf{c}_{i\beta_1}\partial_{\alpha_1}\partial_{\beta_1} f_i^{(0)} = -\frac{1}{\tau} f_i^{(2)}\end{aligned} \tag{3.3.12}$$

and taking zeroth order moments gives

$$\partial_{t_2}\rho + \frac{1}{2}\partial_{t_1 t_1}\rho + \partial_{t_1}\partial_\alpha \rho u_\alpha + \frac{1}{2}\partial_\alpha\partial_\beta \Pi_{\alpha\beta} = 0. \tag{3.3.13}$$

Differentiating (3.3.10) with respect to t_1 and (3.3.11) with respect to α yields

$$\begin{aligned}\partial_{t_1 t_1}\rho &= -\partial_{t_1}\partial_\alpha \rho u_\alpha, \\ \partial_\alpha\partial_{t_1}\rho u_\alpha + \partial_\alpha\partial_\beta \Pi_{\alpha\beta} &= 0, \\ \Rightarrow \partial_{t_1 t_1}\rho &= -\partial_{t_1}\partial_\alpha \rho u_\alpha = \partial_\alpha\partial_\beta \Pi_{\alpha\beta}\end{aligned} \tag{3.3.14}$$

and substituting this into (3.3.13) shows that

$$\partial_{t_2}\rho = 0, \tag{3.3.15}$$

which with (3.3.10) yields the continuity equation:

$$\partial_t \rho + \nabla \cdot \rho\mathbf{u} = 0. \tag{3.3.16}$$

Next taking first order moments of (3.3.12) we find

$$\partial_{t_2}\rho u_\alpha + \partial_\beta Q_{\alpha\beta} + \frac{1}{2}\underbrace{\partial_{t_1 t_1}\rho u_\alpha}_{=-\frac{1}{2}\partial_{t_1}\partial_\beta \Pi_{\alpha\beta}} + \partial_{t_1}\partial_\beta \Pi_{\alpha\beta} + \frac{1}{2}\partial_\beta\partial_\gamma P_{\alpha\beta\gamma} = 0 \tag{3.3.17}$$

$$\Rightarrow \partial_{t_2}\rho u_\alpha + \partial_\beta Q_{\alpha\beta} + \frac{1}{2}\partial_{t_1}\partial_\beta \Pi_{\alpha\beta} + \frac{1}{2}\partial_\beta\partial_\gamma P_{\alpha\beta\gamma} = 0, \tag{3.3.18}$$

where $P_{\alpha\beta\gamma} = \sum_i f_i^{(0)} \mathbf{c}_{i\alpha}\mathbf{c}_{i\beta}\mathbf{c}_{i\gamma}$ and $Q_{\alpha\beta} = \sum_i f_i^{(1)} \mathbf{c}_{i\alpha}\mathbf{c}_{i\beta}$.

For the D2Q9 lattice the momentum flux tensor which gives rise to the Newtonian stress tensor, is

$$\Pi_{\alpha\beta} = p_0\delta_{\alpha\beta} + \rho u_\alpha u_\beta, \tag{3.3.19}$$

where pressure $p_0 = \rho/3$. Differentiating the momentum flux tensor with first with respect to time and space yields

$$\partial_{t_1}\Pi_{\alpha\beta} = \partial_{t_1}\left(\frac{\rho}{3}\delta_{\alpha\beta} + \rho u_\alpha u_\beta\right) \tag{3.3.20}$$

$$= \partial_{t_1}\frac{\rho}{3}\delta_{\alpha\beta} + \partial_{t_1}(\rho u_\alpha u_\beta) \tag{3.3.21}$$

$$= -\frac{1}{3}\partial_\alpha \rho u_\alpha \delta_{\alpha\beta} + \partial_{t_1}(\rho u_\alpha u_\beta) \tag{3.3.22}$$

and

$$\partial_{t_1}\partial_\beta\Pi_{\alpha\beta} == -\frac{1}{3}\partial_\alpha\partial_\beta \rho u_\alpha \delta_{\alpha\beta} + \partial_{t_1}\partial_\beta(\rho u_\alpha u_\beta) \tag{3.3.23}$$

which up to second order in $\mathbf{u}$ (low Mach number approximation) gives,

$$\partial_{t_1}\partial_\beta\Pi_{\alpha\beta} = -\frac{1}{3}\partial_\alpha\partial_\beta \rho u_\beta \tag{3.3.24}$$

and

$$\partial_\beta\partial_\gamma P_{\alpha\beta\gamma} = \frac{1}{3}(\partial_\beta\partial_\beta \rho u_\alpha + 2\partial_\alpha\partial_\beta \rho u_\beta). \tag{3.3.25}$$

To find $Q_{\alpha\beta}$ we take the second moment of equation (3.3.9)

$$\partial_{t_1}\Pi_{\alpha\beta} + \partial\gamma P_{\alpha\beta\gamma} = -\frac{1}{\tau}Q_{\alpha\beta}$$

so that

$$Q_{\alpha\beta} = -\tau\left(\partial_{t_1}\Pi_{\alpha\beta} + \partial\gamma P_{\alpha\beta\gamma}\right). \tag{3.3.26}$$

The substitution of the above into (3.3.18) gives

$$\partial_{t_2}\rho u_\alpha + \left(\frac{1}{2} - \tau_f\right)\left(\partial_{t_1}\partial_\beta\Pi_{\alpha\beta} + \partial_\beta\partial_\gamma P_{\alpha\beta\gamma}\right) = 0. \tag{3.3.27}$$

This can be written as

$$\partial_{t_2}\rho\mathbf{u} = \nu(\nabla^2\rho\mathbf{u} + \nabla\nabla\cdot\rho\mathbf{u}), \tag{3.3.28}$$

where

$$\nu = \frac{1}{3}\left(\tau_f - \frac{1}{2}\right), \tag{3.3.29}$$

is the kinematic viscosity and we note that $0 < \frac{1}{\tau_f} < 2$.

Finally, summing equations (3.3.11) and (3.3.28), assuming incompressibility we arrive at the Navier-Stokes equations for incompressible flow:

$$\partial_t\mathbf{u} + \mathbf{u}\cdot\nabla\mathbf{u} = -\frac{1}{\rho}\nabla p_0 + \nu\nabla^2\mathbf{u}, \tag{3.3.30}$$

$$\nabla\cdot\mathbf{u} = 0. \tag{3.3.31}$$

3.4 Discussion

In Chapter 3 the derivation of the equilibrium distribution function is given in two ways. Firstly it is given as a discretised version of the Maxwell-Boltzmann equilibrium distribution using Gauss-Hermite quadrature and secondly it is constructed from the macroscopic properties required and using them to solve the linear system to recover the coefficients of the equilibrium function. Also in Chapter 3 is the relation between the LBM and Navier-Stokes equations which is given by the Chapman-Enskog multiscale procedure. Chapter 3 is vital when looking for ways to adapt the LBM to solve other problems such as the Fokker-Planck equation as will be shown in Chapter 7.

Chapter 4

Multiphase fluid flows

Multiphase flows are of great importance to industry and applied science as they include processes such as boiling fluids, liquid metal melting and solidification, and even food manufacturing processes such as the creation of mayonnaise.

The numerical simulation of multiphase flows is challenging because in addition to the usual difficulties associated with tracking single phase motion, it also requires the calculation of the interface between the two fluids which changes dynamically in time. Existing methods that deal with moving interfaces generally fall into two distinct categories which are front tracking and front capturing.

In front tracking methods, markers are attached to the moving interface and their dynamics are explicitly designed so that they follow the interface evolution. As long as the interface remains sufficiently smooth, the interface can be tracked fairly accurately. If the interface breaks up and reconnects, front tracking suffers from the similar difficulty of Lagrangian methods, namely ill-conditioning and singularities due to markers coming too close to each other. The main developers of this approach are Glimm and collaborators [34, 20, 35, 33].

Front capturing methods solve this problem by using an Eulerian approach and defining a data structure throughout the whole computational domain. The interface is located by examining where the discontinuities take place. These methods avoid the problems associated with large distortions of the interface but they suffer from severe numerical diffusion effects which tend to

smear out the interface in the course of the computation. Front capturing methods are actually the oldest approach to computing multifluid and multiphase flows. The marker and cell (MAC) method, uses marker particles to identify each fluid and was developed by Harlow and Welch [39] in 1965. The volume of fluid (VOF) method which was first described by Noh and Woodward in 1976 [73] and is based on earlier MAC methods. A modern formulation of VOF is used in a number of computer codes, such as FLOW-3D, ANSYS Fluent and STAR-CCM. A review of the VOF method can be found in Scardovelli and Zaleski [90].

From a review of the literature, we shall discuss four different formulations of LBM for immiscible multiphase flows, namely;

- Chromodynamic models (see [36]);
- Pseudo-potential models (see [95]);
- Free-energy models (see [101]);
- Mean-field models (see [43]).

There seems to be no general consensus yet on which one of these methods should be recommended as the best LBE solution for multiphase problems. In fact, all of them are still affected by a certain degree of inevitable empiricism due to the fact that, even in the continuum, a fully fledged kinetic theory of complex fluid flow is still missing. It seems that all of the LBE models belong to a wide family of diffuse-interface models where the interface is located over several lattice points, the width of which is greatly influenced by the choice of multiphase model.

4.1 Surface Tension

Before we begin a discussion of various LBE models we consider some basic ideas of the physics of multiphase flows. The key to the physics of multiphase flows is the notion of surface tension. From a macroscopic perspective, surface tension (σ) is defined as the reversible work per unit surface needed to increase

the area A of surface Σ by an amount ΔA:

$$\Delta W = \sigma \Delta A. \tag{4.1.1}$$

If we consider a spherical liquid droplet of radius R at a pressure P_l, immersed in its vapour at a pressure $P_v > P_l$. The question is how much work is spent on the vapour-liquid system to expand the radius of the liquid droplet from R to $R + \Delta R$ (condensation). This work is given by $\Delta W = (P_v - P_l)\Delta V$, where $\Delta V = 4\pi R^2 \Delta R$ is the volume change of the droplet. This is the energy supply from the exterior needed to win the action of surface tension, whose 'task' is to withstand the growth of the liquid surface. Mathematically we have:

$$(P_v - P_l)\Delta V = \sigma \Delta A. \tag{4.1.2}$$

Using the equation for the surface area of a sphere ($A = 4\pi R^2$), we obtain the Laplace relation:

$$\Delta P = \frac{2\sigma}{R}. \tag{4.1.3}$$

From a microscopic perspective, surface tension is related to intermolecular interactions. Imagining the same liquid droplet as before, we consider a molecule sitting right on the droplet interface. Since the liquid is more dense than the vapour, this boundary molecule interacts with more liquid molecules than vapour molecules and since the intermolecular potential is attractive (van der Waals forces, hydrogen bonding etc.), the net result is that the boundary molecule naturally tends to be pulled back into the liquid region. This is in contrast to the situation of an internal molecule which, being surrounded by an equal number of molecules in all directions, does not experience any net force.

The conclusion we reach is that a surface molecule has an excess of energy with respect to an internal one, the difference representing the work needed to extract the internal molecule and 'peel it off' the surface. The same energy must be supplied to push a vapour molecule inside the liquid droplet, so that surface growth involves an energy toll. This implies that surface tension is a decreasing function of temperature and vanishes at the critical liquid-vapour point, where the two phases become virtually indistinguishable.

4.2 Chromodynamic models

The first multiphase LBE model was introduced by Gunstensen et al. [36], based upon the two component lattice gas model developed by Rothman and Keller [88].

In these models we have two particle distributions f_{iR} and f_{iB}, one for each fluid. It is common to call these fluids Red (R) and Blue (B). Each phase obeys its own LBGK equation:

$$\Delta_i f_{is} = -\omega_s(f_{is} - f_{is}^{eq}) + S_{is}, \quad i = 1, \ldots, b \quad s = \text{R, B.} \tag{4.2.1}$$

The source term S_{is} represents the mesoscopic interaction between the two phases and it is therefore the term responsible for describing phase separation via surface tension effects. For example, Reis and Phillips [85] handle the source term by a second collision operator.

The central quantities are the colour gradient $\mathbf{F}(\mathbf{x})$ and the colour flux $\mathbf{K}(\mathbf{x})$ defined as follows:

$$\mathbf{F}(\mathbf{x}) = \sum_i \mathbf{c}_i[\rho_r(\mathbf{x} + \mathbf{c}_i) - \rho_b(\mathbf{x} + \mathbf{c}_i)] \tag{4.2.2}$$

and

$$\mathbf{K}(\mathbf{x}) = \sum_i (f_{iR} - f_{iB})\mathbf{c}_i. \tag{4.2.3}$$

Reis and Phillips [85] choose the source term so that the correct form of the continuum equations are recovered. The source term adds mass to populations moving in the direction normal to the red-blue interface and removes mass parallel to the interface. Since this term does not conserve colour densities separately an additional step is needed to promote phase segregation and maintain surfaces between fluids. Succi [100] notes 'that such a type of 'smell and go' dynamics is commonplace in many other sectors of complex fluid dynamics, including polar fluids and biological flows.' Reis and Phillips suggest minimising the 'colour energy' $Q = \mathbf{K} \cdot \mathbf{F}$ to break the colour symmetry and cause the red and blue particles to move in preferential directions and maintain surfaces. This however would involve variational minimisation at every single lattice site where there is a mixture of fluids and is computationally expensive.

Lischuk et al. [62] and Halliday et al. [38] proposed using a continuum surface force to model interfacial tension and promote segregation using the algorithm by D'Ortona et al. [27] which gives a non-zero boundary thickness between the fluids and reduces non-physical effects such as pinning of drops to the lattice, spatial anisotropy in interfacial tension and spurious microcurrents.

Chromodynamic models have some positive and some negative features. With refinement it is able to handle many different phases. For example, DL_MESO [93] is capable of computing up to six different phases and the method is able to model phases with a high density ratio ($\mathcal{O}(1000)$). It is important to note that with chromodynamic approaches, the diffusive interface can be kept very sharp, of the order of one or two lattice sites.

The "coloured fluid" model has some issues, it is more complicated and computationally expensive to implement than the pseudo-potential model and the method is only valid for isothermal flows.

4.3 The pseudo-potential approach

The chromodynamic approach of Gunstensen [36] is based on a significant abstraction of the physical reality. The 'colour force' is nothing but the logical statement that molecules sitting at the interface between, say, dense and light fluids, experience a net force driven by the different values of the average intermolecular distance in the two fluids. It is therefore natural to look for more physically-oriented representations, in which these forces are directly encoded as the result of pairwise molecular interactions.

[95] model interactions between multiple phases and components by calculating pairwise interaction potentials. These potentials use an 'effective mass' for each component, ψ^a, which is a function of density and is most frequently defined as

$$\psi^a(\mathbf{x}) = \rho_0^a \left[1 - \exp\left(-\frac{\rho^a(\mathbf{x})}{\rho_0^a}\right)\right] \tag{4.3.1}$$

where ρ^a is the local density of component a and ρ_0^a is the reference density for the same component.

Defining g_{ab} as the interaction coefficient between components a and b, the overall force on component a due to interactions with other components is

defined as

$$\mathbf{F}^a = -\psi^a(\mathbf{x}) \sum_b g_{ab} \sum_i w_i \psi^b(\mathbf{x} + \mathbf{c}_i)\mathbf{c}_i \tag{4.3.2}$$

There are a few different ways of implementing this force such as adding $\tau_f \mathbf{F}/\rho$ to the velocity of the fluid when calculating the equilibrium distribution function f_i^{eq}, or adding a forcing term to the collisional distribution function which is favoured by Guo et al. [37].

The Shan-Chen model is able to simulate many phase separation and interface phenomena and it is quick to run and code, although it struggles to simulate phases with density ratios bigger than $\mathcal{O}(100)$.

The main drawback of the Shan-Chen model is the lack of thermodynamics as first pointed out by Swift et al. [101]. The thermodynamic inconsistency of the Shan-Chen model can be better explained by examining the pressure tensor. By expanding equation (4.3.2) about $\mathbf{x}$ and recognising that

$$\nabla \cdot \mathbf{P} = \nabla(\rho RT) - \mathbf{F} \tag{4.3.3}$$

must be satisfied at equilibrium we recover

$$\mathbf{P} = \left[\rho RT + \frac{gRT}{2}\psi^2 + \frac{g(RT)^2}{2}(\psi\nabla^2\psi + \frac{1}{2}|\nabla\psi|^2)\right]\mathbf{I} - \frac{g(RT)^2}{2}\nabla\psi\nabla\psi. \tag{4.3.4}$$

This pressure tensor implies that the Shan-Chen model has the two basic properties of non-ideal gases:

(i) An equation of state of the form

$$p_0 = \rho RT + \frac{gRT}{2}\psi(\rho)^2, \tag{4.3.5}$$

(ii) and the surface tension

$$\sigma = \frac{gRT}{2}\infty_{-\infty}^{infty}|\nabla\psi|^2 dz. \tag{4.3.6}$$

However, to be consistent with the equation of state in thermodynamic theory, we must have

$$\psi = \sqrt{\frac{2(p_0 - \rho RT)}{gRT}} \tag{4.3.7}$$

On the other hand, to be consistent with the thermodynamic definition of the surface tension given by Rowlinson and Widom [89],

$$\sigma^{\text{Rowlinson}} \propto \int_{-\infty}^{\infty} |\nabla\rho|^2 dz \tag{4.3.8}$$

we must have

$$\psi \propto \rho. \tag{4.3.9}$$

Since equations (4.3.7) and (4.3.9) cannot be satisfied simultaneously, the Shan-Chen model is thermodynamically inconsistent. The assumption that causes this inconsistency is that a molecule only interacts with its nearest neighbours. The idea of only using nearest neighbour interactions originates from the celebrated Ising model but may not be appropriate for describing molecular interactions in dense fluids. Nearest neighbour interactions only have one characteristic length (the lattice size) and therefore is not sufficient to describe the Lennard-Jones potential where both short range repulsion (Pauli repulsion at short ranges due to overlapping electron orbitals) and long range attraction (van der Waals forces) are important.

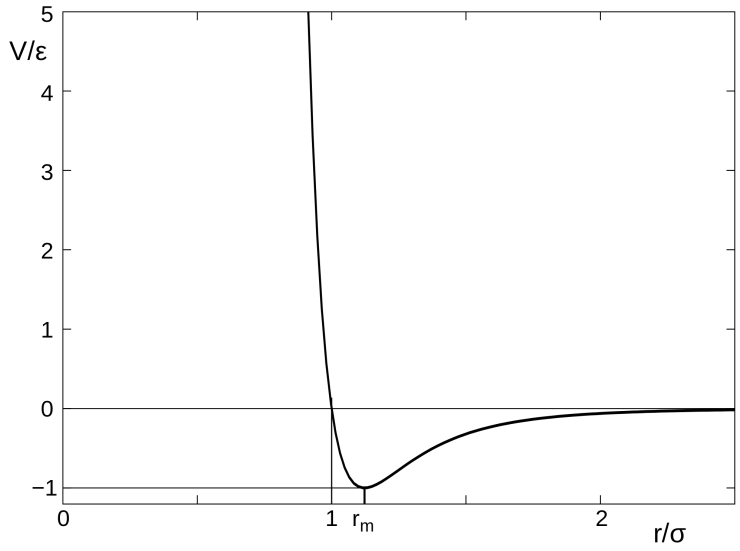

Figure 4.3.1: Lennard Jones Potential

4.4 The free energy approach

A step forward in the direction of thermodynamic consistency was taken by Swift et al. [101]. These authors introduce the equilibrium pressure tensor for a non-ideal fluid directly into an extended form of the collision operator. The idea is that, by doing so, the fluid is instructed to reach the right thermodynamic equilibrium directly under the effect of the correct equation of state. The method of Swift et al. [101] builds on the van der Waals formulation of a two component isothermal fluid. The basic object of the theory is the free energy density functional Ψ, (free energy per unit volume) defined as

$$\Psi[\rho] = \int \frac{1}{2}k\left[(\nabla\rho)^2 + \psi(\rho)\right] dV, \tag{4.4.1}$$

where the first term is the energy penalty paid to build density gradients, and the second term is the bulk free energy where ψ is the free-energy density. The non-local pressure relates to Ψ through the following expression:

$$P = \rho\frac{d\Psi}{d\rho} - \Psi = P_0 - k\rho\nabla^2\rho^2 - \frac{1}{2}k|\nabla\rho|^2, \tag{4.4.2}$$

where

$$P_0 = \rho\Psi' - \Psi \tag{4.4.3}$$

is the equation of state of the fluid (prime stands for derivative with respect to density). The full pressure tensor in a non-uniform fluid includes an off-diagonal component

$$P_{ab} = P\delta_{ab} + k\partial_a\rho\partial_b\rho, \tag{4.4.4}$$

where the second term is related to interfacial surface tension effects.

An important question is how do we encode this pressure tensor in the equilibrium distribution?

The recipe is to add (weakly) non-local terms to the discrete equilibria. In particular, for a seven state FHP lattice, Swift et al. [101] propose the following expression:

$$f_i^{eq} = A + Bc_{i\alpha}u_\alpha + Cu^2 + Dc_{i\alpha}c_{i\beta}u_\alpha u_\beta + F_\alpha c_{i\alpha} + G_{ab}c_{i\alpha}c_{i\beta}, \tag{4.4.5}$$

$$f_0^{eq} = A_0 + C_0u^2 \tag{4.4.6}$$

The Lagrangian parameters $A, B, C, D, F_\alpha, G_{\alpha\beta}$ are prescribed by the usual conservation of mass, momentum and momentum flux tensor constraints, with $P_{\alpha\beta}$ given by (4.4.4). These relations are sufficient to compute the parameters as a function ρ and its spatial derivatives, thus solving the problem of identifying a proper free energy for the multiphase LB system.

Swift et al. [101] demonstrate their model with 2D simulations based on the van der Waals fluid energy density $\Psi_{VdW} = \rho T \ln \rho/(1-\rho^b) - a\rho^2$. Like their predecessors, they test their scheme against Laplace's law:

$$P_{in} - P_{out} = \frac{\sigma}{R}, \tag{4.4.7}$$

where 'in/out' refer to inner/outer pressure of a bubble of radius R. Another test refers to the dispersion relation of capillary waves. They also compute the coexistence curve between the two phases for several values of the (static) fluid temperature, reporting excellent agreement with thermodynamic theory.

The main drawback to using a free energy model is that they suffer from a lack of Galilean invariance in the viscous term when one derives the Navier-Stokes equations. This introduces spurious currents in the interface whenever there is a density gradient. There is one case where the model of Swift et al. [101] works consistently which is for a binary fluid where each fluid is an ideal gas.

4.5 Mean field model

He et al. [43] proposed an LBM multiphase model based on mean field theory and Enskog's model for dense fluids. It was demonstrated later that the mean field model can be derived from the BBGKY theory with appropriate approximations [41]. BBGKY theory (Bogoliubov-Born-Green-Kirkwood-Yvon theory) is a set of equations describing the dynamics of a system of a large number of interacting particles. The equation for an n particle distribution function in the BBGKY theory includes the $(n+1)$ particle distribution function thus forming a coupled chain of equations. To close this system, approximations have to be introduced The key to the mean field model is to use mean field theory to describe the long range attraction among molecules, while using the

Enskog theory for dense fluids to account for short range repulsion. According to Chen et al. [18] we see that the mean field model not only recovers the correct mass, momentum and energy equations, it also contains the correct thermodynamics.

Historically, kinetic theory was first developed for studying ideal gas transport. To extend its application to phase transitions and multiphase flows, one must incorporate molecular interactions which become increasingly important in most fluids as the density increases.

The mean field LBM multiphase model is derived from kinetic theory with the intermolecular potential incorporated intrinsically. From this perspective, it inherits the fundamental feature of the inter-particle potential model. At the same time, the mean field theory guarantees thermodynamic consistency.

In the theory of the BBGKY hierachy, the evolution equation for the single-particle distribution, $f(\boldsymbol{\xi}_1, \mathbf{r}_1)$, is:

$$\partial_t f + \boldsymbol{\xi}_1 \cdot \nabla_{\mathbf{r}_1} f + \mathbf{F} \cdot \nabla_{\boldsymbol{\xi}_1} f = \int\int \frac{\partial f^{(2)}}{\partial \boldsymbol{\xi}_1} \cdot \nabla_{\mathbf{r}_1} V(r_{12}) d\boldsymbol{\xi}_2 d\mathbf{r}_2 \tag{4.5.1}$$

where $\mathbf{F}$ is the external force, $\boldsymbol{\xi}_1$ and $\boldsymbol{\xi}_2$ are microscopic velocities, $f^{(2)}(\boldsymbol{\xi}_1, \mathbf{r}_1, \boldsymbol{\xi}_2, \mathbf{r}_2)$ is the two-particle distribution function, and $V(r_{12})$ is the pair-wise intermolecular potential between particle 1 and particle 2. In the BBGKY hierarchy of equations, the time evolution of n-particle distribution depends on the $(n+1)$st particle distribution. Approximations have to be introduced to close this formulation.

He and Doolen [41] perform a simple closure at the level of the two-particle distribution. They begin by dividing the space integral domain of the right hand side of equation (4.5.1) into two parts: $\{\mathscr{D}_1 : |\mathbf{r_2} - \mathbf{r}_1| < d\}$ and $\{\mathscr{D}_2 : |\mathbf{r_2} - \mathbf{r}_1| \geq d\}$:

$$\begin{aligned} &\int\int \frac{\partial f^{(2)}}{\partial \boldsymbol{\xi}_1} \cdot \nabla_{\mathbf{r}_1} V(r_{12}) d\boldsymbol{\xi}_2 d\mathbf{r}_2 \\ &= \underbrace{\int\int_{\mathscr{D}_1} \frac{\partial f^{(2)}}{\partial \boldsymbol{\xi}_1} \cdot \nabla_{\mathbf{r}_1} V(r_{12}) d\boldsymbol{\xi}_2 d\mathbf{r}_2}_{\mathscr{J}_1} + \underbrace{\int\int_{\mathscr{D}_2} \frac{\partial f^{(2)}}{\partial \boldsymbol{\xi}_1} \cdot \nabla_{\mathbf{r}_1} V(r_{12}) d\boldsymbol{\xi}_2 d\mathbf{r}_2}_{\mathscr{J}_2} \end{aligned} \tag{4.5.2}$$

where d is the effective diameter of molecules. It is known that many intermolecular potentials can be approximated by the Lennard-Jones potential (see Fig 4.3.1), which possesses a short-range strong repulsive core and a long range weak attractive tail. Here the first integral, $\mathscr{J}_1$, describes the strong repulsive force which dominates short range molecular interaction and the second integral, $\mathscr{J}$, describes the weak attractive force which dominates long range molecular interaction.

The short range behaviour is essentially a collision process where the rate of change of the single particle distribution in this process, $\mathscr{J}_1$, can be well modelled by Enskog's theory for dense fluids [13]:

$$\begin{aligned}\mathscr{J}_1 &= \int_{\mathscr{D}_1}\int \frac{\partial f^{(2)}}{\partial \boldsymbol{\xi}_1}\cdot\nabla_{\mathbf{r_1}}V(r_{12})d\boldsymbol{\xi}_2 d\mathbf{r}_2 \\ &= \chi\boldsymbol{\Omega}_0 - b\rho\chi f^{eq}\left\{(\boldsymbol{\xi}-\mathbf{u})\cdot\left[\nabla\log(\rho^2\chi T)+\frac{3}{5}\left(C^2-\frac{5}{2}\right)\nabla\log T\right]\right. \\ &\qquad \left.+\frac{2}{5}\left[2\mathbf{CC}:\nabla\mathbf{u}+\left(C^2-\frac{5}{2}\right)\nabla\cdot\mathbf{u}\right]\right\} \quad (4.5.3)\end{aligned}$$

where $\boldsymbol{\Omega}_0$ is the ordinary collision term which neglects particle size; $\mathbf{C} = (\boldsymbol{\xi}-\mathbf{u})/\sqrt{2RT}$ and C is its magnitude; ":" represents the scalar product of two tensors; $\rho, \mathbf{u}$, and T are the macroscopic density, velocity and temperature, respectively, f^{eq} is the Maxwell equilibrium distribution function:

$$f^{eq} = \frac{\rho}{(2\pi RT)^{3/2}}\exp\left[-\frac{(\boldsymbol{\xi}-\mathbf{u})^2}{2RT}\right] \quad (4.5.4)$$

χ is the density dependent collision probability,

$$\chi = 1+\frac{5}{8}b\rho+0.2869(b\rho)^2+0.1103(b\rho)^3+0.0386(b\rho)^4+\ldots \quad (4.5.5)$$

where $b = 2\pi d^3/3m$, with d being the diameter and m the molecular mass. Notice that the corresponding χ for the van der Waals' equation of state is:

$$\chi = \frac{1}{1-b\rho} \quad (4.5.6)$$

which only agrees with Eq. (4.5.5) to zeroth order.

The rate of change of the single particle distribution due to long range molecular interaction is neglected in Enskog's original work. It can be very important in real fluids. Modern physics has shown that, for most liquids, the radial distribution function is approximately unity beyond a distance of one molecular diameter [83]. This implies that $f^{(2)}(\boldsymbol{\xi}_1, \mathbf{r}_1, \boldsymbol{\xi}_2, \mathbf{r}_2) \approx f(\boldsymbol{\xi}_1, \mathbf{r}_1) f(\boldsymbol{\xi}_2, \mathbf{r}_2)$ in $\mathscr{D}_2$. This approximation leads to:

$$\mathscr{J}_2 = \int_{\mathscr{D}_2} \int \frac{\partial f^{(2)}}{\partial \boldsymbol{\xi}_1} \cdot \nabla_{\mathbf{r}_1} V(r_{12}) d\boldsymbol{\xi}_2 d\mathbf{r}_2 = \nabla \left\{ \int_{\mathscr{D}_2} \rho(\mathbf{r}_2) V(r_{12}) d\mathbf{r}_2 \right\} \cdot \nabla_{\boldsymbol{\xi}_1} f. \tag{4.5.7}$$

The term in the bracket is exactly the mean field approximation for the intermolecular potential [89]:

$$V_m = \int_{\mathscr{D}_2} \rho(\mathbf{r}_2) V(r_{12}) d\mathbf{r}_2 \tag{4.5.8}$$

Its gradient gives the average force acting on a molecule by the surrounding molecules. Assuming the density is a slowly varying variable, we can expand the density in a Taylor series:

$$\rho(\mathbf{r}_2) = \rho(\mathbf{r}_1) + \mathbf{r}_{21} \cdot \nabla \rho + \frac{1}{2} \mathbf{r}_{21} \mathbf{r}_{21} : \nabla \nabla \rho + \ldots \tag{4.5.9}$$

where $\mathbf{r}_{21} = \mathbf{r}_2 - \mathbf{r}_1$. Substituting Eq. (4.5.9) into Eq. (4.5.8), we have:

$$V_m \simeq -2a\rho - \kappa \nabla^2 \rho \tag{4.5.10}$$

where the coefficients a and κ are defined in terms of the intermolecular potential by:

$$a = -\frac{1}{2} \int_{r>d} V(r) d\mathbf{r}, \qquad \kappa = -\frac{1}{6} \int_{r>d} r^2 V(r) d\mathbf{r}$$

a and κ are usually assumed to be constant. The integral, $\mathscr{J}_2$, subsequently becomes:

$$\mathscr{J}_2 = \nabla V_m \cdot \nabla_{\boldsymbol{\xi}_1} f. \tag{4.5.11}$$

This form of $\mathscr{J}_2$ suggests that the average long range intermolecular potential acts on a molecule in exactly the same way as an external potential. In other words, the long range molecular interaction can be modelled as a local point force. It should be mentioned that the above derivations depend on the

assumption that density varies slowly. This obviously is a source of at least some of the issues when modelling binary fluids with a large density ratio.

Combining Enksog's theory for dense fluids and mean field theory for the intermolecular potential, one obtains the following kinetic equation to describe the flow of dense fluids [43]:

$$\partial_t f + \boldsymbol{\xi} \cdot \nabla f + \mathbf{F} \cdot \nabla_{\boldsymbol{\xi}} f = \mathscr{J}_1 + \nabla V_m \cdot \nabla_{\boldsymbol{\xi}} f \tag{4.5.12}$$

where the subscripts have been dropped for simplicity. The macroscopic fluid density, ρ, velocity, $\mathbf{u}$, and the temperature, T, are calculated as the velocity moments of the distribution functions:

$$\rho = \int f d\boldsymbol{\xi} \tag{4.5.13}$$

$$\rho \mathbf{u} = \int \boldsymbol{\xi} f d\boldsymbol{\xi} \tag{4.5.14}$$

$$\frac{3\rho RT}{2} = \int \frac{(\boldsymbol{\xi} - \mathbf{u})^2}{2} f d\boldsymbol{\xi}. \tag{4.5.15}$$

It is important to note that $\mathscr{J}_1$, in general, cannot be expressed as product of a single force and velocity gradient of the distribution function. As a result, the molecular interaction as a whole also cannot be modelled by a single force term, as in the Shan-Chen model.

Any numerical approach can be used to solve the kinetic equation, but obviously we will focus on a discrete numerical lattice Boltzmann based scheme. The lattice restricts the molecule movements and this constraint can cause issues with non-isothermal flows. To study thermodynamics in which temperature variation exists, the theory must be extended. In the study performed by He and Doolen [41], is an expansion approach for small temperature variations.

Most LBM models neglect terms of order M^3 (M is the Mach number). This cut off error does not hamper LBM applications to nearly incompressible flows. [41] assume further that the variation of the absolute temperature is small in the domain of interest.

To facilitate the discussion, they introduce:

$$T = T_0(1 + \theta) \tag{4.5.16}$$

where T_0 is the average temperature of a system and θ is the normalized temperature variation. With the assumptions of small temperature variations and small Mach numbers, the equilibrium density distribution can be approximated by:

$$f^{eq} = \frac{\rho}{(2\pi RT_0)^{3/2}} \exp\left[-\frac{\boldsymbol{\xi}^2}{2RT_0}\right]\left[1 + \left(\frac{\boldsymbol{\xi}^2}{2RT_0} - \frac{3}{2}\right)\theta + \frac{\boldsymbol{\xi}\cdot\mathbf{u}}{RT_0} + \frac{(\boldsymbol{\xi}\cdot\mathbf{u})^2}{2(RT_0)^2} - \frac{\mathbf{u}^2}{2RT_0}\right]. \tag{4.5.17}$$

Using this equilibrium distribution, the next task is to select a discrete velocity set, or quadrature, that replaces the moment integrals in calculating macroscopic variables. It should be noted that the traditional D2Q7, D2Q9, D3Q15, D3Q19 and D3Q27 lattices are inadequate for this type of thermal model as a second-order time integration scheme is necessary, suitable quadratures with higher accuracy can be found in [77].

Nevertheless, once a sufficiently accurate quadrature is chosen ($\mathbf{c}_a$, $a = 1, 2, \ldots, N$), we can define the discrete distribution function as:

$$f_a(\mathbf{r}, t) = w_a f(\mathbf{r}, \mathbf{c}_a, t) \tag{4.5.18}$$

where w_a are the corresponding weight coefficients. If we use the BGK model with a single relaxation time approximation for the ordinary collision term we assume:

$$\nabla_{\boldsymbol{\xi}} f \approx -\frac{(\boldsymbol{\xi} - \mathbf{u})}{RT} f^{eq} \tag{4.5.19}$$

the evolution equation for the discrete distribution function, f_a, becomes:

$$f_a(\mathbf{r} + \mathbf{c}_a\delta_t) - f_a(\mathbf{r}, \delta_t) = -\chi\frac{(f_a - f_a^{eq})}{\tau_f + 0.5} + \frac{\tau_f}{\tau_f + 0.5}\boldsymbol{\Omega}_a f^{eq}\delta_t \tag{4.5.20}$$

where δ_t is the time step and τ_f is the relaxation parameter;

$$\boldsymbol{\Omega}_a = \frac{(\mathbf{c}_a - \mathbf{u})\cdot(\mathbf{F} - \nabla V_m)}{RT} - b\rho\chi\left\{(\mathbf{c}_a - \mathbf{u})\cdot\left[\nabla\log(\rho^2\chi T) + \frac{3}{5}\left(C_a^2 - \frac{5}{2}\right)\nabla\log T\right] + \frac{2}{5}\left[2\mathbf{C}_a\mathbf{C}_a : \nabla\mathbf{u} + \left(C_a^2 - \frac{5}{2}\right)\nabla\cdot\mathbf{u}\right]\right\} \tag{4.5.21}$$

$\mathbf{C}_a = (\mathbf{c}_a - \mathbf{u})/\sqrt{2RT}$ and C_a is its magnitude. The equilibrium distributions have the following forms:

$$f_a^{eq} = w_a \left[1 + \left(\frac{\boldsymbol{\xi}^2}{2RT_0} - \frac{3}{2}\right)\theta + \frac{\boldsymbol{\xi}\cdot\mathbf{u}}{RT_0} + \frac{(\boldsymbol{\xi}\cdot\mathbf{u})^2}{2(RT_0)^2} - \frac{\mathbf{u}^2}{2RT_0}\right] \tag{4.5.22}$$

Note that at least a second order time integration is necessary for LBM multiphase models [43]. Otherwise, non-physical properties such as spurious currents arise in simulations.

The macroscopic variables can be calculated using:

$$\rho = \sum_a f_a \tag{4.5.23}$$

$$\rho\mathbf{u} = \sum_a f_a\mathbf{c}_a + \frac{\delta_t}{2}[\rho\mathbf{F} - \rho\nabla V_m - \nabla(b\rho^2\chi RT)] \tag{4.5.24}$$

$$\frac{3\rho RT}{2} = \frac{3\rho RT_0(1+\theta)}{2} = \sum_a f_a\frac{(\mathbf{c}_a - \mathbf{u})^2}{2} \tag{4.5.25}$$

The viscosity and thermal conductivity of the above model have the following forms:

$$\mu = \tau_f\rho RT_0\delta_t\left(\frac{1}{\chi} + \frac{2}{5}b\rho\right) \tag{4.5.26}$$

$$\lambda = \frac{5}{2}\tau_f\rho R^2T_0\delta_t\left(\frac{1}{\chi} + \frac{3}{5}b\rho\right) \tag{4.5.27}$$

According to the authors the implementation of the model is straightforward. Besides the need for higher order velocity lattices, the only complication compared to the ideal gas LBM model is the calculation of gradients of macroscopic variables in $\boldsymbol{\Omega}_a$. Some of these gradients are involved in previous isothermal LBM multiphase models where their calculations have been straightforward.

The drawback of the mean field LBM multiphase model is that it cannot simulate multiphase flows with high density ratio. This drawback is likely due to the assumption that the density profile across an interface must be smooth. How to improve LBM multiphase models to simulate high density flows is still a challenging task. There have been several advances on this front such as

solving for the pressure field separately (see Inamuro et al. [50] for details).

4.6 Numerical Results

As the reader can see there are a variety of methods for implementing multiphase fluid flow within a lattice Boltzmann method. It is important to know what sorts of fluids you intend to model before you choose a particular scheme. The pseudo potential model is capable of simulating high density ratio fluids but gives relatively low numerical stability and wide interfaces for multicomponent immiscible systems [103]. By contrast the colour model is capable of simulating fluids with a significant viscosity ratio and recovers the analytical solutions for Poiseuille flow and fingering simulations. Due to the current author's interest in Non-Newtonian fluids where viscosity is variable it was decided to focus attention on a colour-gradient model which we present here.

Lattice Boltzmann immiscible two-phase model

The two-dimensional colour-gradient model is developed for immiscible two-phase fluids based on the work by Halliday et al. [38] and Reis and Phillips [85]. We give details again here for completeness. In the model, we label one fluid 'red' and one 'blue'. The distribution function for each fluid is denoted by $f_{i,k}$, where $k = R$ or B, $i = 0, \ldots, 8$, denote velocity directions for the D2Q9 lattice grid, and the total distribution function is defined as $f_i = f_{i,R} + f_{i,B}$. The lattice velocity vectors on the D2Q9 grid are given, as usual, as

$$\mathbf{c}_i = \begin{cases} (0,0), & i = 0, \\ (1,0), (0,1), (-1,0), (0,-1) & i = 1,2,3,4, \text{ respectively}, \\ (1,1), (-1,1), (-1,-1), (1,-1) & i = 5,6,7,8, \text{ respectively}. \end{cases} \tag{4.6.1}$$

In each time step, the distribution function of each fluid undergoes a collision substep and a streaming substep, and the evolution equation is expressed by

$$f_{i,k}(\mathbf{x} + \mathbf{c}_i \Delta t, t + \Delta t) = f_{i,k}(\mathbf{x}, t) + \Omega_{i,k}[f_{i,k}(\mathbf{x}, t)] \tag{4.6.2}$$

where $\mathbf{x}$ and t are the position and time, Δt is the time step, and $\Omega_{i,k}$ is the

collision operator. The collision operator $\Omega_{i,k}$ consists of three parts [85]:

$$\Omega_{i,k} = (\Omega_{i,k})^{(3)}[(\Omega_{i,k})^{(1)} + (\Omega_{i,k})^{(2)}], \tag{4.6.3}$$

where $(\Omega_{i,k})^{(1)}$ is the BGK collision operator, $(\Omega_{i,k})^{(2)}$ is the perturbation operator which generates an interfacial tension, and $(\Omega_{i,k})^{(3)}$ is the recolouring operator which contributes to maintaining the phase interface. For each phase, mass conservation and total momentum conservation are expressed (as usual) as

$$\rho_k = \sum_i f_{i,k} = \sum_i f_{i,k}^{(eq)}, \tag{4.6.4}$$

$$\rho \mathbf{u} = \sum_i \sum_k \mathbf{c}_i f_{i,k} = \sum_i \sum_k \mathbf{c}_i f_{i,k}^{(eq)}, \tag{4.6.5}$$

where ρ_k is the density of fluid k, $\rho = \rho_R + \rho_B$ is the total density, and $\mathbf{u}$ is the velocity of the fluid mixture.

BGK collision operator

The BGK collision operator is applied for each fluid, of which the particle distribution functions are relaxed towards a local equilibrium with a single relaxation time, written as

$$(\Omega_{i,k})^{(1)} = -\omega_k[f_{i,k} - f_{i,k}^{(eq)}]. \tag{4.6.6}$$

For a given multiphase flow, the equilibrium distribution function is defined by [85]

$$f_{i,k}^{(eq)}(\rho, \mathbf{u}) = \rho_k(\phi_{i,k} + W_i[3\mathbf{c}_i \cdot \mathbf{u} + 4.5(\mathbf{c}_i \cdot \mathbf{u})^2 - 1.5(\mathbf{u})^2]) \tag{4.6.7}$$

where W_i is the weight defined by

$$W_i = \begin{cases} 4/9, & i = 0, \\ 1/9, & i = 1, 2, 3, 4, \\ 1/36, & i = 5, 6, 7, 8, \end{cases} \tag{4.6.8}$$

and $\phi_{i,k}$ is a parameter related to the density ratio written as [85]

$$\phi_{i,k} = \begin{cases} \alpha_k, & i = 0, \\ (1-\alpha_k)/5, & i = 1,2,3,4, \\ (1-\alpha_k)/20, & i = 5,6,7,8, \end{cases} \tag{4.6.9}$$

where $0 \leq \alpha_k \leq 1$ should be satisfied to avoid unphysical negative values for fluid density. We note that α_R and α_B should satisfy the constraint

$$\gamma = \rho_R/\rho_B = \frac{(1-\alpha_B)}{(1-\alpha_R)} \tag{4.6.10}$$

[85], where γ is the density ratio of the red to blue fluids. The model has been proved to be valid in Reis and Phillips [85] for simulations with density ratio up to 18.5. Ba et al. [3] consider the case $\gamma = 1$, for simplicity, as their interest was modelling contact-angle hysteresis.

The interface between the two phases is identified by the constant contours of the phase field function ρ^N, which is defined as

$$\rho^N(\mathbf{x},t) = \frac{\rho_R(\mathbf{x},t) - \rho_B(\mathbf{x},t)}{\rho_R(\mathbf{x},t) + \rho_B(\mathbf{x},t)}. \tag{4.6.11}$$

In the single phase regions Reis and Phillips [85] have shown by Chapman-Enskog expansion that the Navier-Stokes equations are recovered. The relaxation parameter ω_k is a function of fluid kinematic viscosity and given by $\omega_k = 1/(3\nu_k + 0.5)$, in which ν_k is the kinematic viscosity of fluid k.

In the interface region ($|\rho^N| < 1$), to ensure the smoothness of the relaxation parameter and the stability of the interface, the relaxation parameter is written as [85]

$$\omega = \begin{cases} \omega_R, & \rho^N > \delta \\ g_R(\rho^N), & \delta \geq \rho^N > 0 \\ g_B(\rho^N), & 0 \geq \rho^N > -\delta \\ \omega_B, & \rho^N < -\delta, \end{cases} \tag{4.6.12}$$

where δ is a free parameter associated with the interface thickness and taken to

be 0.1 in the simulation by Ba et al. [3], and g_R and g_B are parabolic functions of ρ^N written as

$$g_R(\rho^N) = \chi + \eta\rho^N + \kappa(\rho^N)^2, \tag{4.6.13}$$
$$g_B(\rho^N) = \chi + \lambda\rho^N + \upsilon(\rho^N)^2, \tag{4.6.14}$$

in which the coefficients are taken to be

$$\chi = 2\omega_R\omega_B/(\omega_R + \omega_B), \tag{4.6.15}$$
$$\eta = 2(\omega_R - \chi)/\delta, \tag{4.6.16}$$
$$\kappa = -\eta/(2\delta), \tag{4.6.17}$$
$$\lambda = 2(\chi - \omega_B)/\delta, \tag{4.6.18}$$
$$\upsilon = \lambda = (2\delta). \tag{4.6.19}$$

Perturbation operator

In the perturbation operator, the CSF model [38] is used to model the interfacial tension, which has been demonstrated to effectively reduce the spurious velocities [62]. The interface force acts centripetally normal to the local interface and its magnitude is proportional to the gradient of the phase field function (more commonly known as the colour gradient) $\nabla\rho^N$. The local curvature of the interface is given by

$$K = -\nabla_S \cdot \mathbf{n}, \tag{4.6.20}$$

where $\nabla_S = (\mathbf{I} - \mathbf{nn}) \cdot \nabla$ is the surface gradient operator and $\mathbf{n} = -\nabla\rho^N/|\nabla\rho^N|$ is the outward pointing unit normal vector of the interface. In two dimensions, the curvature of the interface can be expressed by

$$K = n_x n_y \left(\frac{\partial}{\partial y}n_x + \frac{\partial}{\partial x}n_y\right) - n_x^2\frac{\partial}{\partial y}n_y - n_y^2\frac{\partial}{\partial x}n_x. \tag{4.6.21}$$

The derivatives can be calculated using a standard finite difference method.

The interfacial tension force is then given by

$$\mathbf{F} = -0.5\sigma K\nabla\rho^N, \tag{4.6.22}$$

where σ is the interfacial tension which is applied only at the lattice sites where the two fluids coexist.

Ba et al. [3], apply the body force of Guo et al. [37] due to its high accuracy in modelling a spatially varying body force and capability in reducing effectively the spurious velocites. According to Guo et al. [37], the perturbation operator $(\Omega_i)^{(2)} = (\Omega_{i,R})^{(2)} + (\Omega_{i,B})^{(2)}$ is written as

$$(\Omega_i)^{(2)} = W_i \left(1 - \frac{\omega}{2}\right) [3(\mathbf{c_i} - \mathbf{u}) + 9(\mathbf{c_i} \cdot \mathbf{u})\mathbf{c}_i] \cdot \mathbf{F} \tag{4.6.23}$$

where the velocity is redefined to include some of the effect of the external body force

$$\rho\mathbf{u} = \sum_i \sum_k \mathbf{c}_i f_{i,k} + \frac{1}{2}\mathbf{F}. \tag{4.6.24}$$

Then the interfacial tension contribution is assigned to each phase, and the pertubation operator of fluid k is given by

$$(\Omega_i)^{(2)} = A_k W_i \left(1 - \frac{\omega_k}{2}\right) [3(\mathbf{c_i} - \mathbf{u}) + 9(\mathbf{c_i} \cdot \mathbf{u})\mathbf{c}_i] \cdot \mathbf{F} \tag{4.6.25}$$

where A_k is the fraction of interfacial tension contributed by the fluid k, and satisfies $\sum_k A_k = 1$.

Recolouring operator

In the work by Ba et al. [3], the recolouring algorithm proposed by Latva et al. [58] is used to promote phase segregation and to maintain a reasonable interface. This algorithm allows the red and blue fluids to mix moderately at the tangent of the interface, and at the same time keeps the colour distribution symmetric with respect to the colour gradient. Thus, it can further reduce the spurious velocities and remove the lattice pinning problem produced by the original recolouring operator of Gunstensen et al. [36]. The algorithm is written as

$$\begin{aligned}
(\Omega_{i,R})^{(3)}(f_{i,R}) &= \frac{\rho_R}{\rho} f_i' + \beta \frac{\rho_R \rho_B}{\rho^2} \cos(\varphi_i) |\mathbf{c}_i| \sum_k f_{i,k}^{(eq)}(\rho_k, 0, \alpha_k), \\
(\Omega_{i,B})^{(3)}(f_{i,R}) &= \frac{\rho_B}{\rho} f_i' + \beta \frac{\rho_R \rho_B}{\rho^2} \cos(\varphi_i) |\mathbf{c}_i| \sum_k f_{i,k}^{(eq)}(\rho_k, 0, \alpha_k),
\end{aligned} \tag{4.6.26}$$

β	0.01	0.1	0.3	0.5	0.7	0.9
Error	0.009034	0.008225	0.008024	0.008008	0.008004	0.008003

Table 4.1: Root mean square error associated with the interface parameter β.

where f_i' is the post-perturbation value of the total distribution function, φ_i is the angle between the colour gradient $\nabla\rho^N$ and the lattice direction $\mathbf{c}_i$, and β is a free parameter associated with the interface thickness such that $0 < \beta < 1$. In the study Ba et al. [3] chose $\beta = 0.7$ to maintain a steady interface [38]. Choosing $\beta = 0.7$ means the interface has a thickness of four to five lattice spaces.

4.7 Poiseuille Flow

Consider two incompressible immiscible fluids moving under the influence of a pressure gradient G in the x-direction. If the flow is stable (the Reynolds number is sufficiently small) and the interface remains in the centre of the channel at all times then the analytic solutions for steady flow are

$$u_r = \frac{Gh^2}{2\mu_r}\left[-\left(\frac{y}{h}\right)^2 + \frac{y}{h}\left(\frac{\mu_r - \mu_b}{\mu_r + \mu_b}\right) + \frac{2\mu_r}{\mu_r + \mu_b}\right], \quad -h \leq y \leq 0, \tag{4.7.1}$$

$$u_b = \frac{Gh^2}{2\mu_b}\left[-\left(\frac{y}{h}\right)^2 + \frac{y}{h}\left(\frac{\mu_r - \mu_b}{\mu_r + \mu_b}\right) + \frac{2\mu_b}{\mu_r + \mu_b}\right], \quad 0 \leq y \leq h, \tag{4.7.2}$$

where h is the half channel width and μ_r and μ_b are the shear viscosities for the red and blue fluids [85].

A 128×65 lattice was used with fixed velocity condition on the top and bottom walls with a periodic boundary and the left and right. Initially the upper half contained pure red fluid, the bottom pure blue and the interface consisted of half red and half blue. Both fluids have the same density but different relaxation times and therefore different viscosities ($\mu_b = 0.2525, \mu_r = 0.7575$). Increasing the value of β sharpens the interface and gives a more accurate answer at the cost of numerical stability. The smoothing of the interface can be seen in Figure 4.7.2 and the overall root mean square error (given by equation (2.5.2)) associated with changing the value of β is given in Table 4.1.

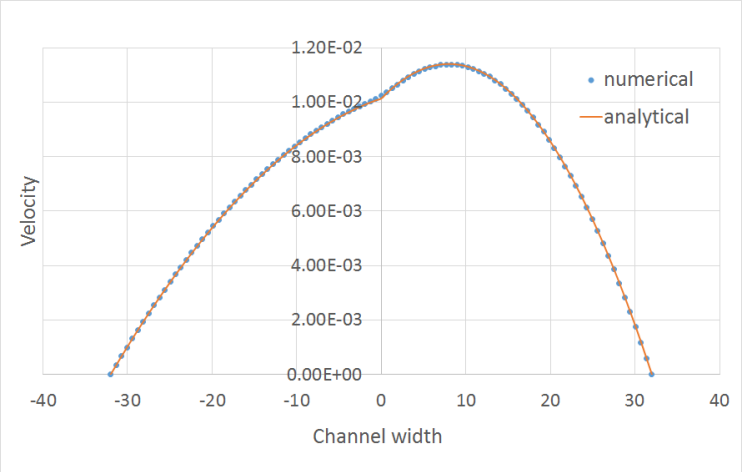

Figure 4.7.1: Numeric measurements of velocity of two adjacent immiscible fluids.

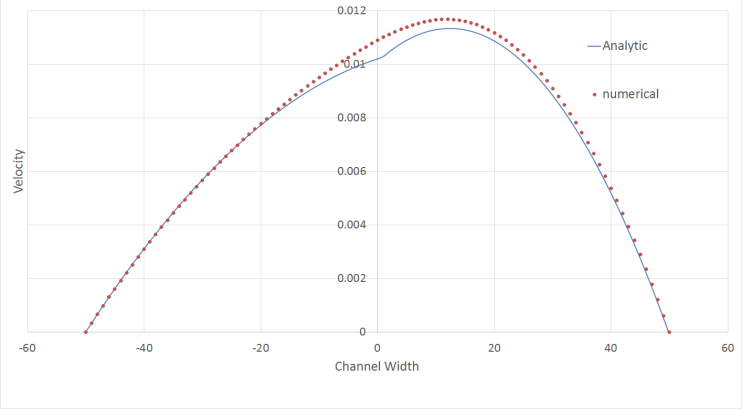

Figure 4.7.2: Numeric measurements of velocity of two adjacent fluids with $\beta = 0.1$

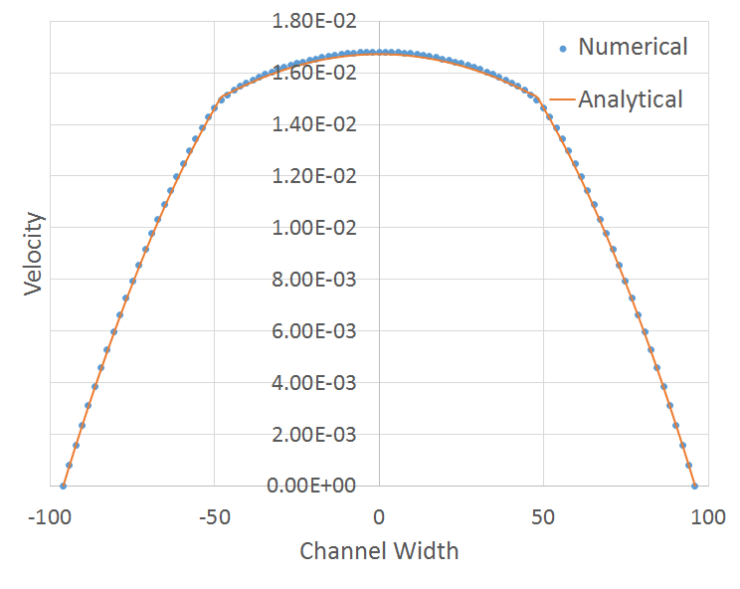

Figure 4.7.3: Numeric measurements of velocity in three-layer Poiseuille flow.

Using the same boundary conditions and body force we measure the velocity of a three-layer 'ABA' flow where one fluid is sandwiched between another less viscous fluid. Once again we see good agreement with the analytic solutions which in this case are

$$u_b = \frac{G}{8}\left(\frac{3h^2}{\mu_r} + \frac{h^2 - 4y^2}{\mu_b}\right), \quad -h \leq y \leq -\frac{h}{2}, \tag{4.7.3}$$

$$u_r = \frac{G}{2\mu_r}\left(h^2 - y^2\right), -\frac{h}{2} \leq y \leq \frac{h}{2}, \tag{4.7.4}$$

$$u_b = \frac{G}{8}\left(\frac{3h^2}{\mu_r} + \frac{h^2 - 4y^2}{\mu_b}\right). \tag{4.7.5}$$

4.8 Discussion

In Chapter 4 an overview of LBM for multiphase fluid flows has been given. The four main approaches are chromodynamic models, pseudo-potential models, free-energy models and mean field models. Free energy and mean field models are necessary when examining non-isothermal flows but are computationally expensive to solve and aren't able to solve fluid flows with a large

density ratio. Pseudo-potential models are easy to implement as they require adding a body force term to the LBM and are capable of simulating fluids with a high density ratio but have relatively low numerical stability and wide diffuse interfaces between the fluids. The colour model is capable of simulating fluids with a significant viscosity ratio and recovers the analytic solutions for Poiseuille flow and fingering simulations. In this Chapter the colour model was used to solve two and three layer Poiseuille flow and gives good agreement with the analytical solutions.

Chapter 5

Lattice Boltzmann methods for droplets

The behaviour of microdroplets on a solid surface is of great interest to many different industries. As well as the obvious application to inkjet printing, it is important for emerging fields such as the noncontact printing of functional electronics and biological materials and in the fields of microfluidic devices, microchemistry, and fast prototyping [98, 94, 104]. The advantages of inkjet printing of liquid materials over traditional delivery techniques are many and based on the technological ability of printheads to generate homogeneously sized droplets on demand at a determined speed and direction [10]. These characteristics create a scenario where precise volumes of reagents and/or reactive components can be dispatched at a specific location at precise times. The process of noncontact printing involves the generation, deposition, and coalescences of droplets to make patterns for graphics applications or three-dimensional structures in other manufacturing processes [25]. In graphical applications, the coalescence of droplets on a substrate needs to be controlled to reduce pixelation and increase the resolution of printing. In contrast, in additive manufacture applications such as in the synthesis of nylon 6 *in situ* via inkjet printing of reactive fluids, good mixing during drop-on-drop deposition is essential [29].

In microdroplet dynamics, the behaviour of the contact line region, where three phases (fluid-fluid-solid) coexist, and the physical mechanism of the microscopic interactions between the fluid and solid phases are very complex and

play a very crucial role [9]. Some numerical methods dealing with contact-line behaviour have been proposed based on macroscopic hydrodynamic equations and/or microscopic molecular dynamics. In the commonly used macroscopic approaches, such as volume of fluid (VOF) [86], the interfacial behaviour is often obtained by solving a transport equation for the volume fraction and implementing an interface reconstruction process, which is very complicated and usually difficult to implement. Also, empirical slip models are required for such kinds of methods to overcome the stress singularity problem associated with the traditional no-slip boundary condition [3]. Microscopic methods have also been applied but they are computationally expensive and this restricts their application to practical problems [51]. Recently Lattice Boltzmann methods have been applied to microdroplet behaviour [11, 10, 3]. Whereas Castrejón-Pita et al. [10] use a pseudopotential model, Ba et al. [3] use a colour model based on the work by Reis and Phillips [85]. In colour-gradient models, the contact angle is usually considered by directly prescribing a colour-function value on the wall or implementing a colour-conserving wetting boundary condition in both static and dynamic contact line simulations. Both methods naturally satisfy the classical Navier slip rule in hydrodynamic models between the dynamic contact angle and contact line velocity, which makes the colour-gradient model an effective tool for the dynamic contact-angle simulations.

What follows is a description of the algorithm of Ba et al. [3] which will be used to solve a variety of problems.

5.1 Numerical implementation of wetting boundary condition

To simulate microdroplet motion on a solid surface we need a colour-gradient wetting boundary condition that includes hysteresis. Ba et al. [3] employ a colour conserving scheme based on Hollis et al. [46] and contact angle hysteresis algorithm based on the numerical strategy of Dupont and Legendre [28] but with some modifications as the original model of Dupont and Legendre [28] is for macroscopic VOF-based models and not the mesoscopic LBM.

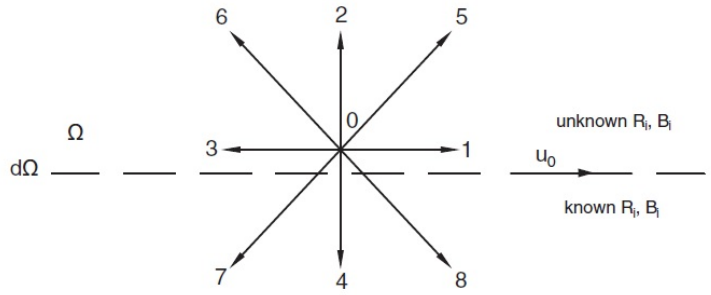

Figure 5.1.1: A D2Q9 lattice node on the bottom boundary of a 2D domain (at propagation step).

Colour conserving boundary condition

To model the fluid-surface interactions, Ba et al. [3] make modifications to the boundary condition proposed by Hollis et al. [46] according to their collision operator $\Omega_{i,k}$ in which the boundary closure scheme is applied to ensure mass conservation for each phase, and a variant of the recolouring operator is designed to maintain the reasonable interface at the solid boundary.

Figure 5.1.1 represents a lattice node on the bottom wall, which moves with velocity $\mathbf{u}_0 = (u_{0x}, u_{0y})$. Assume that the node just lies in the interface of the red and blue fluids. At this lattice node, the post-propagation value of the fluid distribution $f_{i,k}$ exists only for $i \neq 2, 5, 6$, thus, the total distribution function that propagates into the fluid domain at the node for each phase is written as $F_{\text{in}}^k = \sum_{i\neq 2,5,6} f_{i,k}$. On the other hand, the post-perturbation value of the distribution function $f'_{i,k}$ needs to be considered only for the live links, i.e., $i \neq 4, 7, 8$ since the post-perturbation distribution functions with $i = 4, 7, 8$ will propagate out of the fluid domain. Therefore, the effective mass for each phase after collision is given as $\sum_{i\neq 4,7,8} f'_{i,k}$. To ensure mass conservation after each phase, the post-propagation and post-perturbation effective mass of each phase must be equal. Thus, the colour conservation can then be expressed as

$$F_{\text{in}}^k = \sum_{i\neq 4,7,8} f'_{i,k}. \tag{5.1.1}$$

According to the lattice Boltzmann equation (equation (4.6.2)), the distri-

bution function of each phase after the collision can be written as

$$f'_{i,k} = f^{(0)}_{i,k}(\rho'_k, \mathbf{u}_0) + (\Omega_{i,k})^{(2)} + (1-\omega) f^{(1)}_{i,k}, \tag{5.1.2}$$

where ρ'_k represents the auxiliary boundary density determined by the colour conservation. The subtotal of the higher order component of the distribution functions $f^{(1)}_{i,k}$ on the live links is assumed to be zero, and the subtotal of the perturbation operator $(\Omega_{i,k})^{(2)}$ on the live links disrupts the conservation by

$$\Delta M_k = \sum_{i\neq 4,7,8} (\Omega_{i,k})^{(2)} = \sum_{i\neq 4,7,8} A_k W_i \left(1 - \frac{\omega}{2}\right) \times [3(\mathbf{c}_i - \mathbf{u}_0) + 9(\mathbf{c}_i \cdot \mathbf{u}_0)\mathbf{c}_i] \cdot \mathbf{F} \neq 0. \tag{5.1.3}$$

Thus, the subtotal of the equilibrium distribution function $f^{(0)}_{i,k}(\rho'_k, \mathbf{u}_0)$ can be derived using equation (5.1.2), and written as

$$F^k_{in} - \Delta M_k = \sum_{i\neq 4,7,8} f^{(0)}_{i,k}(\rho'_k, \mathbf{u}_0). \tag{5.1.4}$$

Then, the auxiliary boundary density ρ'_k is obtained by introducing the equilibrium distribution function into the above equation:

$$\rho'_k = \frac{F^k_{\text{in}} - \Delta M_k}{\sum_{i\neq 4,7,8} f^{(0)}_{i,k}(1, \mathbf{u}_0)} = \frac{F^k_{\text{in}} - \Delta M_k}{0.7 + 0.3\alpha_k + 0.5u_{0y} - 0.5u^2_{0y}} \tag{5.1.5}$$

Generally, the y component of the wall velocity is considered zero, in which case

$$\rho'_k = \frac{F^k_{\text{in}} - \Delta M_k}{0.7 + 0.3\alpha_k}. \tag{5.1.6}$$

The higher-order distribution function $f^{(1)}_{i,k}$ should satisfy the following con-

straints as given in [46]:

$$\begin{aligned}\sum_{i\neq 4,7,8} f_{i,k}^{(1)} &= 0,\\ \sum_{i} f_{i,k}^{(1)} c_{i\alpha} &= \frac{1}{2}F_\alpha,\\ \sum_{i} f_{i,k}^{(1)} c_{i\alpha}c_{i\beta} &= -\frac{2}{3}\rho_k' S_{\alpha\beta}/\omega,\end{aligned} \tag{5.1.7}$$

where $S_{\alpha\beta}$ is the strain rate tensor and defined in [46] by

$$S_{\alpha\beta} = \frac{1}{2}(\partial_\alpha u_\beta + \partial_\beta u_\alpha) + \frac{3\omega}{4\rho}(F_\alpha u_\beta + F_\beta u_\alpha). \tag{5.1.8}$$

Solving the underspecified equation (5.1.7) by means of the singular value decomposition we obtain $f_{i,k}^{(1)}$ as follows:

$$\begin{pmatrix} f_{0,k}^{(1)}\\ f_{1,k}^{(1)}\\ f_{2,k}^{(1)}\\ f_{3,k}^{(1)}\\ f_{5,k}^{(1)}\\ f_{6,k}^{(1)}\end{pmatrix} = \frac{1}{36}\begin{pmatrix} 0 & -5 & -12 & -2 & 0\\ 3 & -2 & 6 & -8 & 0\\ 0 & 1 & -12 & 10 & 0\\ -3 & -2 & 6 & -8 & 0\\ 3 & 4 & 6 & 4 & 9\\ -3 & 4 & 6 & 4 & -9\end{pmatrix} \times \begin{pmatrix} \delta_t F_x\\ \delta_t F_x y\\ -2\rho_k' S_{xx}/(3\omega)\\ -2\rho_k' S_{yy}/(3\omega)\\ -2\rho_k' S_{xy}/(3\omega)\end{pmatrix}. \tag{5.1.9}$$

Then, the post-perturbation distribution function of each phase on the boundary can be obtained by equation (5.1.2).

A modified recolouring step is needed for boundary nodes to maintain the interface after the collision process. Based on the colour conservation, the post-segregation densities assigned to the live links should satisfy

$$\sum_{i\neq 4,7,8} R_i = F_{\text{in}}^R, \quad \sum_{i\neq 4,7,8} B_i = F_{\text{in}}^B, \quad \sum_{i\neq 4,7,8} f_i = F_{\text{in}}^R + F_{\text{in}}^B, \tag{5.1.10}$$

where R_i (B_i) represent the post-segregation distribution function of red (blue) fluid.

We define ρ_R and ρ_B as the densities of red and blue fluids at the boundary nodes, and $\rho = \rho_R + \rho_B$ as the total density. To obtain an equation for ρ_R and

ρ_B, we substitute equation (4.6.26) into (5.1.10) which yields [3]

$$F_{\text{in}}^R = \frac{\rho_R}{\rho_R+\rho_B}\left(F_{\text{in}}^R + F_{\text{in}}^B\right) \tag{5.1.11}$$

$$+\beta\frac{\rho_R\rho_B}{(\rho_R+\rho_B)^2}\mathbf{n}\cdot\left(\sum_{i\neq 4,7,8}\{[R_i^{eq}(R',0,\alpha_R)+B_i^{eq}(B',0,\alpha_B)]\mathbf{c}_i\}\right)|\mathbf{c}_i|, \tag{5.1.12}$$

which can be expressed in the form

$$F_{\text{in}}^R = \frac{\rho_R}{\rho_R+\rho_B}\left(F_{\text{in}}^R + F_{\text{in}}^B\right)+\beta\frac{\rho_R\rho_B}{(\rho_R+\rho_B)^2}n_y\times\{0.3[\rho_R(1-\alpha_R)+\rho_B(1-\alpha_B)]\}, \tag{5.1.13}$$

where n_y is the y component of the interface normal vector $\mathbf{n}$. The conservation of total mass requires

$$\rho=\sum_k \rho_k'. \tag{5.1.14}$$

Combining equations (5.1.13) and (5.1.14), we obtain a cubic equation with respect to ρ_R:

$$k(\alpha_R-\alpha_B)\rho_R^3+k(-\alpha_R+2\alpha_B-1)\rho\rho_R^2+[(F_{\text{in}}^R+F_{\text{in}}^B)\rho+k\rho^2(1-\alpha_B)]\rho_R-F_{\text{in}}\rho^2=0, \tag{5.1.15}$$

where $k=0.3\beta n_y$. Equation (5.1.15) can be solved by Newton-Raphson say, and then R_i can be calculated using the following segregation formula [3]

$$R_i=\frac{\rho_R}{\rho_R+\rho_B}(f_i')+\beta\frac{\rho_R\rho_B}{(\rho_R+\rho_B)^2}\cos(\varphi_i)|\mathbf{c}_i|\times[R_i^{eq}(\rho_R,0,\alpha_R)+B_i^{eq}(\rho_B,0,\alpha_B)]. \tag{5.1.16}$$

Numerical implementation of constant contact angle

The gradient of the phase field at the boundary nodes is calculated differently from the interior fluid nodes due to the lack of information at adjacent nodes and the necessity of introducing the contact angle. To illustrate the calculation procedure, we choose a bottom boundary node.

For a specified contact angle θ, the gradient of the phase field, $\nabla\rho^N$, at the

boundary node should satisfy

$$\frac{\nabla\rho^N}{|\nabla\rho^N|} = \mathbf{n} = \begin{cases} \sin\theta\mathbf{e}_x + \cos\theta\mathbf{e}_y, & \text{if } \frac{\partial\rho^N}{\partial x} < 0 \\ -\sin\theta\mathbf{e}_x + \cos\theta\mathbf{e}_y, & \text{if } \frac{\partial\rho^N}{\partial x} > 0. \end{cases} \tag{5.1.17}$$

Then, we can obtain a relation for x and y components of $\nabla\rho^N$:

$$\left(\frac{\partial\rho^N}{\partial y}\right)_{x,1} \sin\theta = -\left|\frac{\partial\rho^N}{\partial x}\right|_{x,1} \cos\theta. \tag{5.1.18}$$

Ba et al. [3] evaluate $(\partial\rho^N/\partial x)_{x,1}$ by use of a central difference scheme. The value of $(\partial\rho^N/\partial y)_{x,1}$ is then obtained using equation (5.1.18). Thus, the specified contact angle is implicitly imposed by the gradient of the phase field.

Implementation of dynamic contact angle

In order to reproduce droplet behaviour correctly, it is necessary to develop a contact angle hysteresis model. Ba et al. [3] base their model on the numerical strategy previously proposed in a macroscopic VOF model [28]. It is a colour gradient based algorithm to account for the contact angle hysteresis, in which an iterative procedure is incorporated to obtain an equilibrium contact angle, and the dynamic contact angle is determined by the updated equilibrium contact angle.

Generally, the hysteresis phenomenon of contact line can be defined as follows [99]

$$U_{\text{cl}} > 0 \quad \text{if } \theta_d = \theta_A, \tag{5.1.19}$$

$$U_{\text{cl}} < 0 \quad \text{if } \theta_d = \theta_R, \tag{5.1.20}$$

$$U_{\text{cl}} > 0 \quad \text{if } \theta_R < \theta_d < \theta_A, \tag{5.1.21}$$

where θ_d is the dynamic contact angle, and θ_R and θ_A are, respectively, the limited values of the receding and advancing contact angle. The hysteresis window (θ_R, θ_A) is determined by the properties of the solid substrates in contact with the droplet such as surface roughness and nonuniformity [22]. Ba et al. [3] focus on droplet behaviour with a given hysteresis window. For a given hysteresis window, to model the contact-angle hysteresis behaviour, at

each time step, we need to obtain an instantaneous dynamic contact angle θ_d that satisfies the following condition: the droplet deforms properly within the interval (θ_R, θ_A), beyond which the droplet will move on the solid surface with θ_d obeying the Navier slip relationship. As an illustration see Figure 5.1.2.

Ba et al. [3] implemented an iterative procedure (bisection) for the contact line nodes at both receding and advancing sides to find the equilibrium contact angle θ_e, at which the x component of the fluid momentum u_x will be cancelled locally.

Subsequently, the dynamic contact angle (θ_d) is determined by the following rules based on the calculated equilibrium contact angle:

(1) If $\theta_R < \theta_e < \theta_A$, the dynamic contact angle θ_d is directly assigned as $\theta_d = \theta_e$, and θ_d is then used to calculate the derivatives of the phase field at the solid wall. Thus, the momentum is locally cancelled, and the contact line remains stationary on the solid wall.

(2) If $\theta_e < \theta_R$ or $\theta e > \theta_A$, the equilibrium is disrupted and the droplet starts to move over the solid surface. The dynamic contact angle θ_d is determined such that it satisfies the well known Navier slip relationship i.e.,

$$\begin{aligned} \cos\theta_r &= \cos\theta_R + 9\mathrm{Ca_{cl}}\ln(r/l_m) \quad \text{for } \theta_e < \theta_R, \\ \cos\theta_a &= \cos\theta_A + 9\mathrm{Ca_{cl}}\ln(r/l_m) \quad \text{for } \theta_e > \theta_A, \end{aligned} \tag{5.1.22}$$

where θ_r (θ_a) is the obtained dynamic contact angle at receding (advancing) side, $\mathrm{Ca_{cl}}$ is the contact line Capillary number defined by $\mathrm{Ca_{cl}} = \mu_R U_{\mathrm{cl}}/\sigma$, r is the intermediate length scale and l_m is the microscopic length scale. To guarantee the slip relationship (equation (5.1.22)), empirical slip-length models are usually required in macroscopic models [28]. Latva-Kokko and Rothman [59] have shown that colour-gradient models naturally satisfy the Navier-slip relation, due to the nature of intermolecular interactions of LBM when the θ_R (θ_A) is appointed as the dynamic contact angle θ_d. Based on this argument we take θ_d as θ_R (or θ_A) when θ_e is beyond the hysteresis window, and the obtained θ_d in simulation will vary automatically with $\mathrm{Ca_{cl}}$ according to equation (5.1.22). Therefore, no additional models or assumptions are required in the method described by Ba et al. [3].

To verify the accuracy and applicability of their LBM for simulating droplet

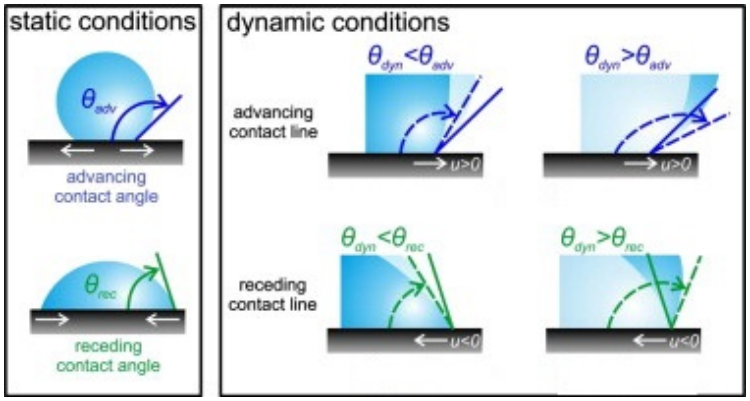

Figure 5.1.2: Illustration of droplet contact angles by Ba et al. [3]

motion Ba et al. [3] firstly investigated the equilibrium shapes of the droplet wetting on a solid surface to verify the models ability to impose a given static contact angle θ_s. Different values of θ_s were used, ranging from $\theta_s = 10°$ to $\theta_s = 170°$. Their results show good agreement between theoretical results and their model for all presented contact angles. Next they validated their dynamic colour-conserving wetting boundary condition by simulationg the dynamical partial wetting process. Initially the droplet with radius R_0 is located with its centroid $0.95R_0$ above the bottom plate. As the droplet continually spreads over the solid surface, its contact angle changes until it is approximately equal to the imposed static contact angle $\theta_0 = 45°$. The time evolution of the dimensionless we length shows good agreement with experimental data. They then use their model to simulate the droplet behaviour subjected to a simple shear flow. For the droplet pinned to the wall, the predicted shape of the droplet agrees with results by Schleizer and Bonnecaze [92].

5.2 Discussion

In this chapter we have discussed a significant colour model capable of simulating the flow of droplets and contact angle hysteresis. With the presented model, the influence of hysteresis on the dynamical behaviour of contact line can be studied systematically, enabling us to predict droplet motion in numerous industrial applications such as ink-jet printing or fibre coating and so it is helpful to improving our understanding of the mechanisms controlling

droplet behaviour at microscale. A key feature of Lattice Boltzmann methods for simulating the impingement and spreading of droplets on solid surfaces is that only the static contact angles are needed as the dynamic contact angle emerges naturally from the simulation without complicated treatment.

Chapter 6

LBM for viscoelastic fluids

So far the focus of this thesis has been on Newtonian fluids, characterised by the Navier-Stokes equation (1.1.13,1.1.14). A Newtonian fluid is a fluid with a simple microstructure, in which the viscous stress is linearly proportional to the rate of strain (rate of change of deformation over time), with the coefficient of proportionality called the viscosity.

This is sufficient to describe many everyday fluids such as air and water but there are many other fluids that are non-Newtonian, such as molten polymers and other commonly found substances such as ketchup, custard, toothpaste, starch suspensions, paint, blood, and shampoo.

There are many different types of non-Newtonian behaviour such as rheopecty or thixotropy, where apparent viscosity increases or decreases under a constant shear rate over time, shear thickening or thinning, where apparent viscosity increases or decreases as the shear rate is increased and viscoelasticity, where the substance exhibits both elastic and viscous behaviour. In this chapter we focus on models for viscoelasticity.

6.1 What are viscoelastic fluids?

Viscoelasticity is the 'property of a substance of exhibiting both elastic and viscous behaviour, the application of a constant stress causing an immediate deformation that disappears if the stress is quickly removed but increases for a time and becomes permanent if the stress is maintained' [74]. In rheology, solids and liquids form a continuum, characterised by the ratio of a charac-

teristic relaxation time (τ_1) of the material to a characteristic time of the experiment (T_0). The time scale ratio, $De = \tau_1/T_0$ is called the Deborah number, after the prophetess in the Book of Judges, and is zero for a Newtonian fluid and infinite for a Hookean elastic solid. The time scale in practice varies widely, for example water, which is 10^{-13}s, minutes for polymer solutions, to hours for melts and soft solids [79].

Understanding the dynamics of polymer solutions is important in relation to plastic manufacture, performance of lubricants and applications of paints [7].

6.2 Mathematically modelling viscoelastic fluids

6.2.1 Linear Viscoelasticity

The macroscopic equations of motion for a fluid are

$$\nabla \cdot \mathbf{u} = 0, \tag{6.2.1}$$

$$\rho \frac{D\mathbf{u}}{Dt} = \nabla \cdot \boldsymbol{\sigma}, \tag{6.2.2}$$

where we have omitted the body force. The stress can be decomposed as follows

$$\sigma_{\alpha\beta} = -P\delta_{\alpha\beta} + T_{\alpha\beta}, \tag{6.2.3}$$

where $\delta_{\alpha\beta}$ is the usual Kronecker delta function and $\mathbf{T}$ is the deviatoric extra stress tensor. The constitutive relation for the extra stress tensor for a Newtonian fluid is given by

$$\mathbf{T} = \eta\dot{\gamma} \tag{6.2.4}$$

where

$$\dot{\gamma} = \nabla\mathbf{u} + (\nabla\mathbf{u})^{\dagger}. \tag{6.2.5}$$

To understand some of the features of linear viscoelasticity we start by examining the behaviour under small amplitude oscillatory shear motion. The

stress can be shown to be [102]

$$\mathbf{T}_{\alpha\beta}(t) = \int_{-\infty}^{t} G(t-t')A^{(1)}_{\alpha\beta}(t')dt' \tag{6.2.6}$$

where $G(t)$ is the relaxation modulus of the fluid and $A^{(1)}_{\alpha\beta}$ is the first Rivlin-Ericksen tensor which is equivalent to the rate of strain [80] (p29) tensor $\dot{\gamma}$. We can recover the stress for a Newtonian fluid by setting $G(t) = \eta\delta(t)$ so that

$$\mathbf{T} = \int_{-\infty}^{t} \eta\delta(t-t')\dot{\gamma}(t')dt' = \eta\dot{\boldsymbol{\gamma}}(t). \tag{6.2.7}$$

Consider one-dimensional shearing motion and in particular small amplitude oscillatory motion with strain given by

$$\gamma(t) = \gamma_0 \exp(i\omega t), \tag{6.2.8}$$

where i is the imaginary unit, ω is the frequency and γ_0 is the strain amplitude. Then

$$\dot{\gamma} = i\omega\gamma_0 \exp(i\omega t), \tag{6.2.9}$$

and substituting this into (6.2.6) we recover

$$T = i\omega\gamma_0 \exp(-i\omega t) \int_{-\infty}^{t} G(t-t') \exp(i\omega t')dt'. \tag{6.2.10}$$

Defining the complex modulus G^* as T/γ and making the change of variable $s = t - t'$ gives

$$G^\star = i\omega \int_0^\infty G(s) \exp(-i\omega s)ds. \tag{6.2.11}$$

The real and imaginary components of $G^\star$

$$G^\star = G' + iG'' \tag{6.2.12}$$

are known as the storage modulus G' and loss modulus G''. The complex viscosity, $\eta^\star$ is defined to be $T/\dot{\gamma}$, hence

$$\eta^\star = \eta' - i\eta'' = \frac{G''}{\omega} - i\frac{G'}{\omega}. \tag{6.2.13}$$

The exact form of $\eta^\star$ depends on the constitutive relation for stress. Two such models are the Maxwell and Jeffreys model which are given by

$$T + \lambda_1 \dot{T} = \eta \dot{\gamma}, \tag{6.2.14}$$

$$T + \lambda_1 \dot{T} = \eta(\dot{\gamma} + \lambda_2 \ddot{\gamma}) \tag{6.2.15}$$

respectively, where λ_1 is a relaxation time and λ_2 is a retardation time. For the Jeffreys model (6.2.15) the components of the complex shear viscosity are found to be

$$\eta' = \eta_\infty + \frac{\eta_0 - \eta_\infty}{1 + (\omega\lambda_1)^2}, \tag{6.2.16}$$

$$\eta'' = \frac{\omega\lambda_1(\eta_0 - \eta_\infty)}{1 + (\omega\lambda_1)^2}, \tag{6.2.17}$$

where η_0 and η_∞ are the zero and infinite frequency viscosities, respectively. The special case $\eta_\infty = 0$ recovers the Maxwell model.

Extending the Maxwell model (6.2.14) to higher dimensions gives the Upper Convected Maxwell (UCM) model for stress

$$\mathbf{T} + \lambda_1 \overset{\nabla}{\mathbf{T}} = \eta \dot{\gamma} \tag{6.2.18}$$

where $\overset{\nabla}{\mathbf{T}}$ denotes the upper convected derivative of $\mathbf{T}$ given by

$$\overset{\nabla}{\mathbf{T}} = \frac{D\mathbf{T}}{Dt} - (\nabla \mathbf{u}) \cdot \mathbf{T} - \mathbf{T} \cdot (\nabla \mathbf{u})^\dagger. \tag{6.2.19}$$

6.2.2 Constitutive equations derived from microstructures

In the microstructural approach, a relevant model for the microstructure of the fluid is proposed and the consequences of this are explored at the macrostructural level, with appropriate averages (ensemble or volume) being taken to smooth out microstructural details.

In dilute polymer solutions, we neglect the interaction between different polymers and inter-polymer interaction and therefore the only forces that come into play are the hydrodynamic forces and the Brownian forces exerted on the

polymer by the surrounding solvent molecules.

The elastic dumbbell model

We consider an elastic dumbbell immersed in a Newtonian solvent and consisting of two identical beads and an inter-connecting spring. The two beads each have mass m and have position vectors $\mathbf{r}_1$ and $\mathbf{r}_2$ relative to some fixed coordinate frame. The equations of motion for the beads in the dumbbell can be written as [80]

$$m\frac{d}{dt}\left(\frac{d\mathbf{r}_i}{dt}-\mathbf{u}(\mathbf{r}_i)\right)=-\zeta\left(\frac{d\mathbf{r}_i}{dt}-\mathbf{u}(\mathbf{r}_i)\right)+\mathbf{F}_i+\mathbf{B}_i,\quad i=1,2, \tag{6.2.20}$$

where $\mathbf{u}(\mathbf{r}_i)$ is the velocity of the solvent at the point with position vector $\mathbf{r}_i$, $\mathbf{F}_i$ is the force on the ith bead exerted by the spring, ζ is the friction coefficient and $\mathbf{B}_i$ is the Brownian force due to the impact of the solvent molecules on the ith bead given by

$$\mathbf{B}_i dt=\sqrt{2kT\zeta}d\mathbf{W}_i \tag{6.2.21}$$

where $\mathbf{W}_i=\mathbf{W}_i(t)$ is a multi-dimensional Wiener process. Let $\mathbf{Q}=\mathbf{r}_2-\mathbf{r}_1$ denote the end-to-end vector of the dumbbell and suppose that the flow is homogeneous so that we may write

$$\mathbf{u}(\mathbf{r}_i)=\mathbf{u}(\mathbf{0})+\kappa\mathbf{r}_i, \tag{6.2.22}$$

where $\kappa=(\nabla\mathbf{u})^\dagger$ is constant in space. It was shown by Schieber and Öttinger [91] that by subtracting the two components of (6.2.20) and introducing the relative velocity

$$\mathbf{V}=\frac{d\mathbf{Q}}{dt}-\kappa\mathbf{Q}, \tag{6.2.23}$$

we now arrive at the equivalent first-order system of stochastic equations

$$\begin{aligned} m d\mathbf{V} &= -(\zeta\mathbf{V}+2\mathbf{F})dt+2\sqrt{kT\zeta}d\mathbf{W}_t,\\ d\mathbf{Q} &= (\mathbf{V}+\kappa\mathbf{Q})dt, \end{aligned} \tag{6.2.24}$$

where $\mathbf{F}=\mathbf{F}_1=-\mathbf{F}_2$ and $\mathbf{W}_t=(\mathbf{W}_2-\mathbf{W}_1)/\sqrt{2}$.

Suppose that the probability that a dumbbell has an orientation in the

range $\mathbf{Q}$ to $\mathbf{Q}+d\mathbf{Q}$ and a velocity in the range $\mathbf{V}$ to $\mathbf{V}+d\mathbf{V}$ at time t is given by $\psi(\mathbf{Q},\mathbf{V},t)d\mathbf{Q}d\mathbf{V}$, where $\psi(\mathbf{Q},\mathbf{V},t)$ is the configurational distribution function. The Fokker-Planck equation corresponding to the system of equations (6.2.24) and governing the evolution of $\psi(\mathbf{Q},\mathbf{V},t)$ is

$$\frac{\partial\psi}{\partial t} = -\frac{\partial}{\partial\mathbf{Q}}\cdot[(\mathbf{V}+\kappa\mathbf{Q})\psi] + \frac{1}{m}\frac{\partial}{\partial\mathbf{V}}\cdot[(\zeta\mathbf{V}+2\mathbf{F})\psi] + \frac{2kt\zeta}{m^2}\frac{\partial^2\psi}{\partial\mathbf{V}^2}. \tag{6.2.25}$$

By taking entropic spring force laws of the form

$$\mathbf{F} = Hf(Q)\mathbf{Q} \tag{6.2.26}$$

where H is a spring constant and $f(Q)$ some scalar function of the dumbbell length $Q=|\mathbf{Q}|$, and $\lambda_1 = \zeta/4H$ for the relaxation of the dumbbell configuration we arrive at the contracted Fokker-Planck equation [80]

$$\frac{\partial\psi}{\partial t} = -\frac{\partial}{\partial\mathbf{Q}}\cdot\left[\kappa\mathbf{Q}\psi - \frac{1}{2\lambda_1}f(Q)\mathbf{Q}\psi - \frac{2kT}{\zeta}\frac{\partial\psi}{\partial\mathbf{Q}}\right]. \tag{6.2.27}$$

Defining the ensemble average $\langle\cdot\rangle$ for any function g of $\mathbf{Q}$ by

$$\langle g(\mathbf{Q})\rangle = \int g(\mathbf{Q})\psi(\mathbf{Q},\mathbf{V},t)d\mathbf{Q} \tag{6.2.28}$$

and by referring to Bird et al. [8], relating the extra-stress tensor $\mathbf{T}$ to the ensemble average of the dyadic product $\mathbf{QF}$ as

$$\mathbf{T} = -nkT\mathbf{I} + \eta_s\dot{\gamma} + n\langle\mathbf{QF}\rangle, \tag{6.2.29}$$

where n is the number density of the dumbbells, we arrive at the Kramers expression for the stress tensor. We now multiply (6.2.27) by $\mathbf{QQ}$, integrate over $\mathcal{R}^3$, and use the divergence theorem and the fact that $\psi\to 0$ as $|\mathbf{Q}|$ tends to its maximum permissible length to obtain [48]

$$\langle\overset{\nabla}{\mathbf{QQ}}\rangle = \frac{4kT}{\zeta}\mathbf{I} - \frac{1}{\lambda_1}\langle\mathbf{QF}\rangle \tag{6.2.30}$$

and by substituting for $\langle\mathbf{QF}\rangle$ into the Kramers expression (6.2.29) for $\mathbf{T}$ we

recover the Giesekus expression for the stress tensor

$$\mathbf{T} = \eta_s \dot{\gamma} - \frac{n\zeta}{4} \langle \overset{\nabla}{\mathbf{QQ}} \rangle. \tag{6.2.31}$$

If the connecting spring force is Hookean, the force law for $\mathbf{F}$ is

$$\mathbf{F} = H\mathbf{Q} \tag{6.2.32}$$

and equations (6.2.29) and (6.2.31) become

$$\mathbf{T} = -nkT\mathbf{I} + \eta_s \dot{\gamma} + nH\langle \mathbf{QQ} \rangle, \tag{6.2.33}$$

$$\mathbf{T} = \eta_s \dot{\gamma} - \frac{n\zeta}{4} \langle \overset{\nabla}{\mathbf{QQ}} \rangle. \tag{6.2.34}$$

Observing that

$$\overset{\nabla}{\mathbf{I}} = -\dot{\gamma} \tag{6.2.35}$$

we can eliminate $\langle \mathbf{QQ} \rangle$ between equations (6.2.33) and (6.2.34) by taking the upper convected derivative of (6.2.33) to give

$$\mathbf{T} + \lambda_1 \overset{\nabla}{\mathbf{T}} = \eta_0 \left(\dot{\gamma} + \lambda_2 \overset{\nabla}{\dot{\gamma}} \right) \tag{6.2.36}$$

where

$$\lambda_2 = \frac{\eta_s \zeta}{4(\eta_p + \eta_s)H} = \frac{\eta_s \lambda_1}{(\eta_p + \eta_s)} \tag{6.2.37}$$

is the characteristic retardation time for the fluid and $\eta_0 = \eta_p + \eta_s$ is the total viscosity where the zero shear rate polymeric viscosity, η_p, is given by

$$\eta_p = \frac{nkT\zeta}{4H}. \tag{6.2.38}$$

Equation (6.2.36) is known as the Oldroyd B constitutive equation. The solvent and polymeric contributions to the stress can be separated as

$$\mathbf{T} = \eta_s \dot{\gamma} + \boldsymbol{\tau}_p, \tag{6.2.39}$$

where $\boldsymbol{\tau}_p$ is the elastic stress and by substituting into (6.2.36) we obtain

$$\boldsymbol{\tau}_p + \lambda_1 \overset{\nabla}{\boldsymbol{\tau}}_p = \eta_p \dot{\gamma} \tag{6.2.40}$$

which is the UCM equation for the extra stress $\mathbf{T}$ as $\eta_s \to 0$.

The Oldroyd-B model is crude and cannot capture many features of real complex fluids. However, the model has a constant shear viscosity and so can be useful in providing qualitative predictions of the flow of Boger fluids. Boger fluids are the exception in having a constant viscosity and as a consequence the Oldroyd B model is of limited use in industrial applications. The infinite extensibility of the Hookean connecting spring leads to an extensional viscosity which blows up at a finite extensional rate [80] making the Oldroyd-B model unable to predict extensional flow of dilute polymer solutions.

This leads naturally to examining whether something tractable and useful can come out of a finitely extensible spring model. As an alternative to the Hookean spring consider the connector force law

$$\mathbf{F} = \frac{H\mathbf{Q}}{1 - (\mathrm{tr}(\mathbf{QQ})/Q_0^2)} \tag{6.2.41}$$

where Q_0^2 is some finite constant. It may be seen that with a force law of this type the spring cannot be extended beyond a length Q_0. This gives rise to the model's name FENE which stands for finitely extensible nonlinear elastic. The main problem with FENE is that it is not possible to derive a closed form constitutive equation directly from the diffusion equation for the configuration pdf [80]. It is common to make approximations to FENE such as FENE-P (first described by Peterlin [78] hence the 'P'), however due to its simplifications, FENE-P is not able to predict the hysteresis effects that polymers have in elongational flow in contrast to the FENE model [6].

CONNFFESSIT

Traditionally the mathematical description and numerical simulation of the flow of polymeric fluids have involved the coupling of the macroscopic equations for the conservation of linear momentum and of mass with the determination of the polymeric contribution to the Cauchy stress tensor through

some constitutive equation, considering the fact that the stresses depend not only on the instantaneous rate of deformation but also on the history of the deformation which fluids experienced.

The idea of using stochastic simulations of the polymer dynamics as an alternative to solving constitutive equations for the determination of the polymer stress is due to Laso and Öttinger [57]. They termed this hybrid method CONNFFESSIT (Calculation of Non-Newtonian Flow: Finite Elements and Stochastic Simulation Technique). This approach combines a finite element solution of the conservation equations with stochastic simulation techniques for computing polymer stress. Since the approach combines a description of the microstructure of a polymeric liquid using kinetic theory with a macroscopic description of the flow this type of simulation method is known as a micro-macro approach. This approach allows for greater flexibility in the kinetic theory models that can be studied since it does not require the existence of an equivalent or approximate closed-form constitutive equation. Therefore, models based on kinetic theory considerations such as the FENE model can be simulated without resorting to closure approximations that are not universally accurate.

Numerical methods based on the micro-macro approach decouple the solution of the conservation laws from the solution of the stochastic differential equation for the polymer conformations that serves to determine the polymer contribution to the extra-stress tensor. At each time step (for transient flows) or iteration (for steady flows) the micro-macro algorithm proceeds as follows:

1. Using the current approximation to the polymer stress as a source term in the momentum equation the conservation equations are solved using standard finite element methods, for example, to obtain updated approximations to the velocity and pressure fields.

2. The new velocity field is then used to convect a sufficiently large number of model polymer 'molecules' through the flow domain. This is achieved by integrating the stochastic differential equation associated with the kinetic theory model along particle trajectories.

3. The polymer stress within an element is determined from the configurations of the polymer molecules in that element.

These steps are repeated until convergence is obtained.

Despite the advantages of the CONNFFESSIT approach in terms of the kinetic theory models that can be simulated there were a number of computational shortcomings in the original implementations of the idea. First, the trajectories of a large number of molecules have to be determined. Secondly, to evaluate the local polymer stress the model polymer molecules must be sorted according to elements. Thirdly, the computed stress may be nonsmooth and this may cause problems when differentiated to form the source term in the momentum equation [80].

6.3 Viscoelastic Lattice Boltzmann methods

In general, the equations governing the motion of viscoelastic fluids are complicated nonlinear partial differential equations. For example, for an incompressible fluid one must solve the system of equations

$$\nabla \cdot \mathbf{u} = 0, \tag{6.3.1}$$

$$\rho \frac{D\mathbf{u}}{Dt} = \nabla \cdot \boldsymbol{\sigma}, \tag{6.3.2}$$

$$\boldsymbol{\sigma} = -p\mathbf{I} + \mathbf{T} \tag{6.3.3}$$

where the extra stress tensor $\mathbf{T}$ is given by an appropriate consitutive equation such as the UCM model. There are only a few special cases where analytical solutions exist and most of those are for the simpler rheological models. Therefore, accurate and efficient numerical schemes are vital for solving non-Newtonian flow problems. Traditional approaches to solving non-Newtonian flow problems are very similar to solving Newtonian flow problems, such as finite difference, finite volume, finite elements or spectral elements. Some of the problems previously discussed when solving Newtonian fluid problems are apparent for non-Newtonian fluid problems. For example, irregular geometries, unresolved theoretical problems concerning compatibility conditions to ensure a well-posed discrete problem (LBB condition), and difficulties in dealing with the convective term, $\mathbf{u} \cdot \nabla \mathbf{T}$. Since the lattice Boltzmann method is based on discrete mesoscopic dynamics, and has already proved to be useful in solving Newtonian fluid problems in irregular geometries (such as porous rock) it is

considered a promising computational tool for viscoelastic flows.

6.3.1 A lattice Boltzmann method for the Jeffreys model

The first attempt to incorporate viscoelastic effects into the lattice Boltzmann method was by Giraud et al. [31], who added the Jeffreys' complex shear viscosity (6.2.17) into the original LBE framework. They considered the LBE with a full collision matrix,

$$f_i(\mathbf{x}+\mathbf{c}_i, t+1) = f_i(\mathbf{x}, t) - \sum_j \Omega_{ij}(f_j - f_j^{eq}). \tag{6.3.4}$$

and first defined the model on a D2Q13 lattice. As previously discussed in Chapter 1, the leading nonzero eigenvalue of the scattering matrix Ω controls the viscosity of the LB fluid with the remaining eigenvalues arbitary. The normalised eigenvectors of this model were chosen to be

$$\begin{aligned}
\boldsymbol{\phi}_0 &= (1,1,1,1,1,1,1,1,1,1,1,1,1)/\sqrt{13},\\
\boldsymbol{\phi}_1 &= (0,1,0,-1,0,1,-1,-1,1,2,0,-2,0)/\sqrt{14},\\
\boldsymbol{\phi}_2 &= (0,0,1,0,-1,1,1,-1,-1,0,2,0,-2)/\sqrt{14},\\
\boldsymbol{\phi}_3 &= (28,15,15,15,15,2,2,2,2,-24,-24,-24,-24)/2\sqrt{1001},\\
\boldsymbol{\phi}_4 &= (0,1,-1,1,-1,0,0,0,0,4,-4,4,-4)/2\sqrt{17},\\
\boldsymbol{\phi}_5 &= (0,0,0,0,0,1,-1,1,-1,0,0,0,0)/2,\\
\boldsymbol{\phi}_6 &= (4,-2,-2,-2,-2,1,1,1,1,0,0,0,0)/6,\\
\boldsymbol{\phi}_7 &= (28,4,4,4,4,-20,-20,-20,-20,9,9,9,9)/6\sqrt{77},\\
\boldsymbol{\phi}_8 &= (0,-2,0,2,0,1,-1,-1,1,0,0,0,0)/2\sqrt{3},\\
\boldsymbol{\phi}_9 &= (0,0,-2,0,2,1,1,-1,-1,0,0,0,0)/2\sqrt{3},\\
\boldsymbol{\phi}_{10} &= (0,-2,0,2,0,-2,2,2,-2,3,0,-3,0)/\sqrt{42},\\
\boldsymbol{\phi}_{11} &= (0,0,-2,0,2,-2,2,2,-2,0,3,0,-3)/\sqrt{42},\\
\boldsymbol{\phi}_{12} &= (0,-4,4,-4,4,0,0,0,0,1,-1,1,-1)/2\sqrt{17},
\end{aligned}$$

corresponding to the eigenvalues

$$\{0,0,0,\lambda_e,\lambda_\nu,\lambda'_\nu,\lambda_S,\lambda_S,\lambda_\chi,\lambda_\chi,\lambda'_\chi,\lambda'_\chi,\lambda_z\}. \tag{6.3.5}$$

To incorporate viscoelastic effects into this model, Giraud et al. [31] coupled the symmetric viscous stress tensor to some new quantity that evolves slowly in time causing memory effects. The new model they proposed was a D2Q15 model with $\boldsymbol{\phi}_4$ and $\boldsymbol{\phi}_5$ replaced by

$$\boldsymbol{\phi}_4 = (a, 0, 0, 1, -1, 1, -1, 0, 0, 0, 0, 4, -4, 4, -4), \tag{6.3.6}$$

$$\boldsymbol{\phi}_5 = (0, b, 0, 0, 0, 0, 0, 1, -1, 1, -1, 0, 0, 0, 0), \tag{6.3.7}$$

and two new eigenvectors

$$\boldsymbol{\phi}_{13} = (-68/a, 0, 0, 1, -1, 1, -1, 0, 0, 0, 0, 4, -4, 4, -4), \tag{6.3.8}$$

$$\boldsymbol{\phi}_{14} = (0, -4/b, 0, 0, 0, 0, 0, 1, -1, 1, -1, 0, 0, 0, 0), \tag{6.3.9}$$

where a and b are coupling constants and the eigenvectors haven't been normalised. The corresponding eigenvalues are denoted by $[\lambda_\gamma, \lambda_\gamma]$ and the added lattice vectors are in the rest particle position. The other eleven eigenvectors are derived from the previous D2Q13 lattice with each vector having an additional two components equal to zero added to the front of them.

If $\lambda_\gamma = 0$, the moments m_{13} and m_{14} are conserved and the following macroscopic equations are obtained

$$\partial_t \rho + \partial_x j_x + \partial_y j_y = 0, \tag{6.3.10}$$

$$\partial_t j_x + \left(\partial_x \frac{j_x^2}{\rho} + \partial_y \frac{j_x j_y}{\rho}\right) + \partial_x P + \frac{c_\perp}{\kappa}(\partial_x m_{13} + \partial_y m_{14}) = \nu_\infty \Delta j_x + \xi_\infty \partial_x (\partial_x j_x + \partial_y j_y), \tag{6.3.11}$$

$$\partial_t j_y + \left(\partial_y \frac{j_y^2}{\rho} + \partial_x \frac{j_x j_y}{\rho}\right) + \partial_y P + \frac{c_\perp}{\kappa}(\partial_x m_{14} - \partial_y m_{13}) = \nu_\infty \Delta j_y + \xi_\infty \partial_y (\partial_x j_x + \partial_y j_y), \tag{6.3.12}$$

$$\partial_t m_{13} + \kappa(\partial_x j_x - \partial_y j_y) = D_\infty \Delta m_{13}, \tag{6.3.13}$$

$$\partial_t m_{14} + \kappa(\partial_x j_y + \partial_y j_x) = D_\infty \Delta m_{14}, \tag{6.3.14}$$

where $\mathbf{j}$ is the momentum, and κ and $c_\perp$ are free parameters such that $0 < \kappa < 749/442$ and $c_\perp^2 < \kappa/2 < 749/884$. The viscosity and pressure are given

by

$$\nu_\infty = \left(\frac{\kappa}{2} - c_\perp^2\right)\left(\frac{1}{\lambda_\nu} - 0.5\right), \tag{6.3.15}$$

$$\xi_\infty = \left(\frac{2\kappa}{2} - c_s^2\right)\left(\frac{1}{\lambda_e} - 0.5\right), \tag{6.3.16}$$

$$D_\infty = c_\perp^2 \frac{845 - 1383\kappa + 442\kappa^2}{\kappa(749 - 442\kappa)}\left(\frac{1}{\lambda_\xi} - 0.5\right), \tag{6.3.17}$$

$$P = c_s^2 \rho, \tag{6.3.18}$$

where the sound speed, c_s is a free parameter.

When $\lambda_\gamma \neq 0$, m_{13} and m_{14} are not conserved quantities and must have equilibrium values and are set to zero in Giraud et al. [31] for simplicity. If λ_γ is of the same order of magnitude as the other eigenvalues, the Navier-Stokes equations can be derived by the Chapman-Enskog analysis with a shear viscosity

$$\nu_0 = \left(\frac{\kappa}{2} - c_\perp^2\right)\left(\frac{1}{\lambda_\nu} - 0.5\right) + c_\perp^2\left(\frac{1}{\lambda_\nu} - 0.5\right). \tag{6.3.19}$$

When λ_γ is non-zero but very small, the fluid behaves viscously for time scales much longer than $1/\lambda_\gamma$ and elastically for very short time scales. Although this model was encouraging the results presented were only qualitative and the amount of numerical evidence for viscoelasticity is small. Giraud et al. were unable to derive the macroscopic equations of motion since the Chapman-Enskog analysis assumes the time scales are much larger than the inverse of the smallest non-zero eigenvalue, which is not necessarily true in this model.

This model was improved by Giraud et al. [32] by reducing the lattice to a D2Q11 model. They argued that the collision matrix Ω_{ij} can be perturbed in the same manner as the distribution functions in the Chapmann-Enskog analysis so that

$$\mathbf{\Omega} = \mathbf{\Omega}^{(0)} + \epsilon\mathbf{\Omega}^{(1)} + \epsilon^2\mathbf{\Omega}^{(2)}. \tag{6.3.20}$$

The matrices are assumed to have the same eigenvectors which are split into three groups. The conserved ones with zero eigenvalues, the quasi-conserved ones with zero eigenvalues for $\mathbf{\Omega}^{(0)}$ but non zero ones for $\mathbf{\Omega}^{(1)}$ and $\mathbf{\Omega}^{(2)}$ and the non-conserved ones with non zero eigenvalues for $\mathbf{\Omega}^{(0)}$ and zero eigenvalues for $\mathbf{\Omega}^{(1)}$ and $\mathbf{\Omega}^{(2)}$. After some algebra, the three conservation equations and two

quasi-conservation ones corresponding to the eleven-velocity model are given by

$$\partial_t \rho + \partial_x j_x + \partial_y j_y = 0, \tag{6.3.21}$$

$$\begin{aligned} &\partial_t j_x + \partial_x P + c_\perp(\partial_x m_9 + \partial_y m_{10}) \left(1 - \frac{\lambda_\gamma}{2}\right) \\ &\quad = \nu_\infty \Delta j_x + \xi_\infty \partial_x(\partial_x j_x + \partial_y j_y), \end{aligned} \tag{6.3.22}$$

$$\begin{aligned} &\partial_t j_y + \partial_y P + c_\perp(\partial_x m_{10} - \partial_y m_9) \left(1 - \frac{\lambda_\gamma}{2}\right) \\ &\quad = \nu_\infty \Delta j_y + \xi_\infty \partial_y(\partial_x j_x + \partial_y j_y), \end{aligned} \tag{6.3.23}$$

$$\left(1 - \frac{\lambda_\gamma}{2}\right) \partial_t m_9 + \lambda_\gamma m_{10} + \partial_x j_x - \partial_y j_y = D_\infty \Delta m_9, \tag{6.3.24}$$

$$\left(1 - \frac{\lambda_\gamma}{2}\right) \partial_t m_{10} + \lambda_\gamma m_9 + \partial_x j_x - \partial_y j_y = D_\infty \Delta m_{10}, \tag{6.3.25}$$

where

$$\nu_\infty = \left(\frac{1 - 4c_\perp^2}{4}\right) \left(\frac{1}{\lambda_\nu} - 0.5\right), \tag{6.3.26}$$

$$\xi_\infty = \left(\frac{3}{4} - c_s^2\right) \left(\frac{1}{\lambda_e} - 0.5\right), \tag{6.3.27}$$

$$D_\infty = c_\perp^2 \left(\frac{1}{\lambda_\xi} - 0.5\right). \tag{6.3.28}$$

The three conservation equations can also be written in an equivalent mechanical formulation

$$\partial_t \rho + \partial_x j_x + \partial_y j_y = 0, \tag{6.3.29}$$

$$\partial_t j_\alpha = \partial_\beta \sigma_{\alpha\beta}, \tag{6.3.30}$$

where the stress tensor $\sigma_{\alpha\beta} = -P\delta_{\alpha\beta} + \sigma_{\alpha\beta}^{(v)} + \sigma_{\alpha\beta}^{(N)}$ contains two traceless tensors, one the usual viscous form for compressible fluids (v) and one for the non-Newtonian contributions (N)

$$\sigma_{\alpha\beta}^{(v)} = \nu_\infty(\partial_\alpha j_\beta + \partial_\beta j_\alpha - \partial_\gamma j_\gamma \partial_{\alpha\beta}) + \xi_\infty \partial_\gamma j_\gamma \delta_{\alpha\beta}, \tag{6.3.31}$$

$$\sigma_{\alpha\beta}^{(N)} = c_\perp \left(1 - \frac{\lambda_\gamma}{2}\right) m_{\alpha\beta} \tag{6.3.32}$$

where $m_{xx} = m_{yy} = m_9$ and $m_{xy} = m_{yx} = m_{10}$. Equation (6.3.32) is a solution of

$$\sigma_{\alpha\beta}^{(N)} + \tau(\partial_t \sigma_{\alpha\beta}^{(N)} + D_\infty \Delta \sigma_{\alpha\beta}^{(N)}) = (\nu_0 - \nu_\infty)(\partial_\alpha j_\beta + \partial_\beta j_\alpha - \partial_\gamma j_\gamma \delta_{\alpha\beta},) \quad (6.3.33)$$

which Giraud et al. [32] claim is the Jeffreys constitutive equation with an added stress diffusion term $D_\infty \Delta \sigma_{\alpha\beta}^{(N)}$, which becomes negligible when $D_\infty \tau \approx 1$.

For verification, Giraud et al. [32] simulated a pulsed Couette flow between two plates, where the plate at height $h = 0$ oscillates in time with pulsation ω while the other one at $h = H$ was kept fixed and modelled with the bounce-back condition. Their results for the amplitude of the flow velocity are in excellent agreement with theoretical predictions but errors in the second harmonic are observed.

It should be noted that the right hand side of (6.3.33) should contain time derivatives that are present in a Jeffreys model. It should also be noted that equation (6.3.33) does not satisfy the principles of objectivity of continuum mechanics (cf. [79] for further details) and thus is not frame invariant and may only be valid for simple shear flows (with $\alpha = x$ and $\beta = y$ in (6.3.33)).

6.3.2 Lattice Fokker-Planck Equation

Luo and He [66] have shown how the lattice Boltzmann equation can be derived from a direct numerical discretisation of the continuous Boltzmann equation. A lattice Boltzmann style equation for the Fokker-Planck equation has been developed by Onishi et al. [75] which uses the ideas of Luo to discretise the Fokker-Planck equation on a lattice in order to recover the UCM model for polymeric liquids.

The procedures are organised as follows. Firstly, the configuration space is discretised so that the moments of ψ in the discrete space agree with those in the continuous space. Then, the time evolution equation for the distribution function defined in the discrete space is derived, and is further discretised in physical space and time.

In order to illustrate the discretisation procedure, a new variable $\psi(\mathbf{Q}) = \phi(\mathbf{Q}) e^{-(H/2k_B T_m)(\mathbf{Q}\cdot\mathbf{Q})}$ and a normalisation factor $Q_C = \sqrt{2k_B T_m / H}$ are intro-

duced. With the new variable, the moments of ψ involve integrations of the form,

$$\langle B(\mathbf{Q})\rangle = \int B(\mathbf{Q})\psi(\mathbf{Q})d(\mathbf{Q}) = \left(\frac{2k_BT_m}{H}\right)^{D/2}\int B(Q_C\boldsymbol{\xi})\phi(Q_C\boldsymbol{\xi})e^{-\boldsymbol{\xi}\cdot\boldsymbol{\xi}}d\boldsymbol{\xi}, \tag{6.3.34}$$

where $B(\mathbf{Q})$ is an arbitrary function of $\mathbf{Q}$, and $\boldsymbol{\xi} = \mathbf{Q}/Q_C$ is a non-dimensional configuration vector. It is well known that this form of integration can be approximated with Gauss-Hermitian quadrature up to a certain order depending on the number of the vectors, N, used to span the discrete space:

$$\int \xi_\alpha^m e^{-\boldsymbol{\xi}\cdot\boldsymbol{\xi}}d\boldsymbol{\xi} = \boldsymbol{\pi}^{D/2}\sum_j^N \omega_j\xi_{j\alpha}^m, \tag{6.3.35}$$

where ξ_α is the α-th component of a D dimensional vector $\boldsymbol{\xi}$, $\boldsymbol{\xi}_j$ is the j-th vector of the discrete space, and ω_j is the corresponding weight factor. Applying the Gauss-Hermite quadrature, $\langle B(\mathbf{Q})\rangle$ can be evaluated by the weighted summation with a new weight ψ_j,

$$\langle B(\mathbf{Q})\rangle = \sum_j^N B(\mathbf{Q}_j)\psi_j, \tag{6.3.36}$$

where

$$\psi_j = \omega_j\left(\frac{2\pi k_BT_m}{H}\right)^{D/2}\phi(\mathbf{Q}_j). \tag{6.3.37}$$

This result indicates that any moments of ψ in continuous space can be evaluated with equation (6.3.36), in discrete space. From this viewpoint, ψ_j can be regarded as the configurational distribution function in the discrete configuration space $\mathbf{Q}_j = Q_C\boldsymbol{\xi}_j$.

The time evolution equation for ψ_j can be derived by referring to the Fokker-Planck equation,

$$\frac{\partial\psi_j}{\partial t} = -\mathbf{u}\cdot\nabla\psi_j + \Omega_{\psi,j} + M_j. \tag{6.3.38}$$

We have collected terms from the continuous Fokker-Planck equation based on their physical interpretation. $\Omega_{\psi,j}$ describes the transition process for the dumbbells to approach an equilibrium state, due to the competition between

the thermal fluctuations and the spring force between the connected beads. M_j describes the effect of the solvent flow on the rotation and elongation of the polymer dumbbells. The term $-\mathbf{u}\cdot\nabla\psi_j$ accounts for the convection of the dumbbells based on the solvent flow. The equilibrium distribution $\psi^{eq}(\mathbf{Q})$ is determined as the following

$$\psi^{eq}(\mathbf{Q}) = \left(\frac{H}{2\pi k_B T_m}\right)^{D/2} \exp\left(-\frac{H}{2k_B T_m}\mathbf{Q}\cdot\mathbf{Q}\right). \tag{6.3.39}$$

By the direct substitution of equation (6.3.37) into equation (6.3.39), the discrete equilibrium distribution ψ_j^{eq} is obtained as

$$\psi_j^{eq} = \omega_j. \tag{6.3.40}$$

The dynamics to approach the equilibrium states can be approximated with a relaxation model when the system is close to its equilibrium. Onishi et al. [75] consider a single relaxation time model similar to the BGK model for the velocity distribution function in the standard LBM for $\Omega_{\psi,j}$

$$\Omega_{\psi,j} = -\frac{1}{\tau_\psi}(\psi_j - \psi_j^{eq}), \tag{6.3.41}$$

where τ_ψ is the relaxation time for ψ_j. Next, the discrete model to account for effects of solvent flows M_j is derived. A direct substitution of equation (6.3.37) into the first term in the right-hand side of equation (6.2.27) results in the following

$$M_j = \psi_j \frac{H}{k_B T_m}\left(\mathbf{Q}_j\mathbf{Q}_j - \frac{k_B T_m}{H}\mathbf{I}\right) : \boldsymbol{\kappa}^\dagger - \boldsymbol{\kappa}^\dagger : \mathbf{Q}_j \frac{\partial \psi_j}{\partial \mathbf{Q}}. \tag{6.3.42}$$

Unfortunately, the second term still involves a partial derivative in the configuration space, and needs further discretisation. This difficulty, however, can be avoided by replacing the previously derived terms M_j by

$$M_j = \omega_j \left(\frac{H}{k_B T_m}\right)^2 \left(\mathbf{Q}_j\mathbf{Q}_j - \frac{k_B T_m}{H}\mathbf{I}\right) : \left(\boldsymbol{\kappa}^\dagger \cdot \langle \mathbf{Q}_j\mathbf{Q}_j\rangle\right). \tag{6.3.43}$$

Equation (6.3.43) is obtained in a rather ad hoc manner in that it was derived so that the number of density of polymers is conserved and isotropy is main-

tained. It can be shown that the zeroth to second moments agree with those of the continuous model. In this sense, M_j can be used to recover the correct dynamics at the continuous level, at least up to the second moment of $\mathbf{Q}$ i.e.

$$\sum_j M_j = 0, \quad \sum_j \mathbf{Q}_j M_j = 0, \quad \sum_j \mathbf{Q}_j \mathbf{Q}_j M_j = \boldsymbol{\kappa}^\dagger \cdot \langle \mathbf{Q}_j \mathbf{Q}_j \rangle + \langle \mathbf{Q}_j \mathbf{Q}_j \rangle \cdot \boldsymbol{\kappa} \tag{6.3.44}$$

The final step is the discretisation of physical space and time of equation (6.3.38). In order to discretise equation (6.3.38) in time, equation (6.3.38) is integrated with the second-order scheme, as the derivation of the LBE for thermohydrodynamics [40]

$$\psi_j(\mathbf{x}_j, t + \Delta t) - \psi_j(\mathbf{x}_j, t) = \Delta\psi_j - \frac{\Delta t}{\tau_\psi + 0.5\Delta t}[\psi_j(\mathbf{x}, t) - \psi_j^{eq}(\mathbf{x}, t)] + \frac{\tau_\psi}{\tau_\psi + 0.5\Delta t} M_j \Delta t. \tag{6.3.45}$$

It is interesting to note that in this discretisation the ψ_j term in equation (6.3.45) is not the same as the ψ_j in equation (6.3.38). In fact

$$\bar{\psi_j} = \psi_j + \frac{\Delta t}{2\tau_\psi}\left(\psi_j - \psi_j^{eq}\right) - \Delta t \frac{M_j}{2} \tag{6.3.46}$$

where $\bar{\psi_j}$ is the new ψ_j in equation (6.3.45). This alters the second order moment of ψ_j and hence the approximation to $\langle \mathbf{Q} \cdot \mathbf{Q} \rangle$ introducing an error when trying to simulate equation (6.3.38) but it has been confirmed through simulations that this discretisation method has second-order accuracy with respect to space and time [75]. Unlike the standard Lattice Boltzmann equation in the literature, the left hand side of equation (6.3.45) is the variation of ψ_j in time. A discrete model for the convection term $\Delta\psi_j$ will be discussed later.

Equation (6.3.45) is the main equation proposed in the paper to evaluate viscoelastic stresses of fluids. The viscoelastic stresses are again obtained in the Kramers form

$$\boldsymbol{\tau}_p = -n_p \sum_j \mathbf{Q}_j \mathbf{F}_j^C \psi_j + n_p \sum_j \mathbf{Q}_j \mathbf{F}_j^C \psi_j^{eq}. \tag{6.3.47}$$

The dynamics of $\boldsymbol{\tau}_p$ calculated by equation (6.3.47) is equivalent to the UCM model because the time evolution of the second moment of the discrete distribution satisfies the following equation

$$\langle \mathbf{Q}_j \overset{\nabla}{\mathbf{Q}}_j \rangle = -\frac{1}{\tau_\psi} \left(\langle \mathbf{Q}_j \mathbf{Q}_j \rangle - \frac{k_B T_m}{H} \mathbf{I} \right). \tag{6.3.48}$$

Note that equation (6.3.48) holds only if the vectors and weight factors in the Gauss-Hermite quadrature equation (6.3.35) are chosen so that second order moments can be resolved exactly. One of the optimal choices for this purpose in the two-dimensional case is given by

$$\mathbf{Q}_j = \begin{cases} (0,0), & j = 0, \\ (\pm 1, 0)Q, \quad (0, \pm 1)Q, & j = 1,2,3,4, \\ (\pm 1, \pm 1)Q, & j = 5,6,7,8. \end{cases} \tag{6.3.49}$$

where $Q = \sqrt{3 k_B T_m / H}$, and Q must be set to unity. The corresponding weight factors are $\omega_j = 4/9(|\mathbf{Q}_j|^2 = 0),\ 1/9(|\mathbf{Q}_j|^2 = Q^2)\ 1/36(|\mathbf{Q}_j|^2 = 2Q^2)$

With such a choice, equation (6.3.35) holds for $m = 0, 1, \ldots, 5$, which is sufficient for the recovery of the second-order equation (6.3.48). Note that the number of discrete vectors can be reduced due to the head-tail symmetry of the dumbbells currently considered. However, the vectors shown above may be useful for future applications such as modelling block copolymers with conformational asymmetry.

Finally, the polymer relaxation time and the zero-shear-rate viscosity are related to the relaxation time for ψ_j as,

$$\lambda_H = \tau_\psi,\ \mu_p = n_p k_B T_m \tau_\psi. \tag{6.3.50}$$

Coupling with the Lattice Boltzmann model

In this section, the hydrodynamics of the solvent is modelled by the LBM. In the LBM, states of fluids are described by the velocity distribution $f_i(\mathbf{x}, t)$ which indicates the probability of having a particle with velocity $\mathbf{c}_i$ at lattice site $\mathbf{x}$ and time t. For simplicity the D2Q9 model is shown here. For such a

system, the evolution equation of f_i is given as the following equation which can be derived directly from the Boltzmann equation,

$$f_i(\mathbf{x}+\mathbf{c}_i\Delta t, t+\Delta t) - f_i(\mathbf{x},t) = -\frac{\Delta t}{\tau_n + 0.5\Delta t}[f_i(\mathbf{x},t) - f_i^{eq}(\mathbf{x},t)] + \frac{\tau_n}{\tau_n + 0.5\Delta t} F_i \Delta t. \quad (6.3.51)$$

where $\Omega_i = -\Delta t(f_i - f_i^{eq})/(\tau_n + 0.5\Delta t)$ describes the collision process of particles, that is, the BGK model with the relaxation time τ_n and F_i is the body force term. Again it is interesting to note that this discretisation introduces an error in the second moment of f_i. The non-equilibrium momentum flux $\mathbf{\Pi}^{(1)}$ in this discrete system is given by

$$\mathbf{\Pi}^{(1)} = \frac{\bar{\mathbf{\Pi}} - \mathbf{\Pi}^{(0)}}{1 + \Delta t/(2\tau_n)} \quad (6.3.52)$$

rather than by $\mathbf{\Pi} - \mathbf{\Pi}^{(0)}$ as in the continuous system [23].

The equilibrium distribution f_i^{eq} depends on local physical quantities such as the number density of particles $n_s = \Sigma_i f_i$ and the flow velocity $\mathbf{v} = \Sigma_i \mathbf{c}_i f_i / n_s$. The constraints on the choice of f_i^{eq} are to conserve mass and momentum during the collision process, and to satisfy isotropy and Galilean invariance. The commonly used equilibrium distribution which satisfies such constraints can be obtained by expanding the Maxwell-Boltzmann distribution up to the second-order in $\mathbf{v}$

$$f_i^{eq} = n_s \omega_i \left[1 + \frac{3\mathbf{c}_i \cdot \tilde{\mathbf{v}}}{c^2} + \frac{9(\mathbf{c}_i \cdot \tilde{\mathbf{v}})^2}{2c^4} - \frac{3\tilde{v}^2}{2c^2}\right], \quad (6.3.53)$$

where $c^2 = 3k_B T_m/m$ is the magnitude of the characteristic velocity of the particles, which is set to be unity for the Gauss-Hermite quadrature, with m being the mass of the particle. The weight factor ω_i is given as $4/9(|\mathbf{c}_i|^2 = 0)$, $1/9(|\mathbf{c}_i|^2 = c^2)$, $1/36(|\mathbf{c}_i|^2 = 2c^2)$, and $\tilde{\mathbf{v}}$ is set to $\mathbf{v} + 0.5\Delta t(\mathbf{F}/\rho)$ with $\mathbf{F}$ the body force acting on the fluid.

When the expanded Maxwell-Boltzmann distribution is used, equation (6.3.51) recovers the Navier-Stokes equation at the continuous level, with the

viscosity related to the relaxation time τ_n

$$\boldsymbol{\tau}_s = \mu_s(\boldsymbol{\kappa} + \boldsymbol{\kappa}^\dagger), \quad \mu_s = n_s k_B T_m \tau_n. \tag{6.3.54}$$

Onishi et al. [75] introduce a modified equilibrium distribution in order to incorporate the excess stress $\boldsymbol{\tau}_p$ accounting for the contribution from dumbbells

$$\begin{aligned} f_i^{eq} &= n_s \omega_i \left[1 + \frac{3\mathbf{c}_i \cdot \tilde{\mathbf{v}}}{c^2} + \frac{9(\mathbf{c}_i \cdot \tilde{\mathbf{v}})^2}{2c^4} - \frac{3\tilde{v}^2}{2c^2} \right] + \omega_i T_i, \\ T_i &= \frac{9}{2} \left(\frac{\mathbf{c}_i \mathbf{c}_i}{c^2} - \frac{1}{3}\mathbf{I} \right) : \frac{\boldsymbol{\tau}_p}{k_B T_m}. \end{aligned} \tag{6.3.55}$$

With the modified equilibrium distribution, the zeroth to second velocity moments are, respectively, calculated as

$$\Sigma_i f_i^{eq} = n_s, \tag{6.3.56}$$

$$\Sigma_i \mathbf{c}_i f_i^{eq} = n_s \tilde{\mathbf{v}}, \tag{6.3.57}$$

$$\Sigma_i \mathbf{c}_i \mathbf{c}_i f_i^{eq} = n_s \tilde{\mathbf{v}}\tilde{\mathbf{v}} + \frac{n_s k_B T_m}{m}\mathbf{I} + \frac{\boldsymbol{\tau}_p}{m}. \tag{6.3.58}$$

These results show that the introduction of T_i does not effect the conservation of mass and the conservation of momentum during the collision process. Using the Chapman-Enskog analysis, however, it can be shown that the macroscopic dynamics still obey the Navier-Stokes equations, except that the total stress is now composed of two parts, $\boldsymbol{\tau} = \boldsymbol{\tau}_s + \boldsymbol{\tau}_p$. Thus, combining the results equation (6.3.47) and equation (6.3.54), the proposed Lattice Boltzmann equation (6.3.51) is shown to recover the continuity equation and the Navier-Stokes equation coupled with the Oldroyd-B constitutive equation at the continuous level. Finally, the body force term F_i can be calculated as follows,

$$F_i = 3\omega_i \left[\frac{\mathbf{c}_i - \tilde{\mathbf{v}}}{c^2} + \frac{3\mathbf{c}_i \mathbf{c}_i \cdot \tilde{\mathbf{v}}}{c^4} \right] \cdot \mathbf{F}. \tag{6.3.59}$$

The convection model for dumbbells

In practical simulations, physical space is firstly discretised with square lattices. Two distribution functions, one for the configuration of dumbbells and the other for the velocity distribution of solvent particles, are initialised at each

lattice point with certain values. Then, these distributions are let to evolve according to equation (6.3.45) and equation (6.3.51), respectively. In the time evolution processes, two distributions interact with each other through f_i^{eq}, M_j and so on.

It is appropriate here to elucidate the method to calculate the net variation of the number of dumbbells due to the flow to solvent, that is, $\Delta\psi_j$ in equation (6.3.45). The simplest way is to use the velocity distribution of the solvent as the weights to count the number of dumbbells entering and leaving each lattice point. The central lattice point $\mathbf{x}_c$ exchanges dumbbells with the neighbouring lattice points $\mathbf{x}_\alpha = \mathbf{x}_c + \mathbf{g}_\alpha$, where $\mathbf{g}_\alpha$ is a connecting vector of the two lattice points. The number of solvent particles flying from $\mathbf{x}_c$ to $\mathbf{x}_\alpha$ is $f_\alpha(\mathbf{x}_c)$, and conversely, $f_{\alpha'}(\mathbf{x}_\alpha)$ is the number of solvent particles flying from $\mathbf{x}_\alpha$ to $\mathbf{x}_c$, where α' indicates the index for the opposite direction of $\mathbf{c}_\alpha$. Hence, the net variation of the number dumbbells with the configuration vector $\mathbf{Q}_j$ is evaluated with the weight $W_\alpha(\mathbf{x})$

$$\Delta\psi_j(\mathbf{x}_c) = \Sigma_\alpha \left[-\psi_j(\mathbf{x}_c)W_\alpha(\mathbf{x}_c) + \psi_j(\mathbf{x}_\alpha)W_{\alpha'}(\mathbf{x}_\alpha)\right]/\bar{n}, \tag{6.3.60}$$

$$W_\alpha(\mathbf{x}) = f_\alpha/\Sigma_i f_i(\mathbf{x}), \tag{6.3.61}$$

where $\psi_j(\mathbf{x}_c)W_\alpha(\mathbf{x}_c)$ can be considered as the probability for the dumbbells to move from the lattice point $(\mathbf{x}_c)$ into $(\mathbf{x}_\alpha)$ and $\bar{n}$ is a normalisation factor. Equation (6.3.60) can be expanded around $\mathbf{x}_c$ up to the second-order of $\mathbf{g}_\alpha$, which results in the following equation.

$$\Delta\psi_j(\mathbf{x}_c) \approx -\mathbf{v}\cdot\nabla\psi_j + \frac{1}{6}\nabla^2\psi_j. \tag{6.3.62}$$

This result indicates that there exists a diffusion term in addition to the convection term. The additional diffusion term may be justified as the result of the thermal fluctuation of the solvent. However, the length and time scales of the polymer diffusion should be much smaller compared with hydrodynamic scales. Also, the diffusion term is unwanted for constructing an accurate scheme for the constitutive equation. For these reasons, Onishi et al. introduce an anti-diffusion term into the weight factors as follows,

$$W_\alpha(\mathbf{x}) = f_i/\Sigma f_i(\mathbf{x}) - C\omega_\alpha \tag{6.3.63}$$

where ω_α is the weight factor to calculate the equilibrium distribution of f_i and C is the control parameter for the anti-diffusion coefficient.

Numerical results Onishi model

Onishi et al. [75] calculate shear and first normal stress difference using their model and the results show good agreement with theoretical predictions at a Deborah number $De = \lambda_H \dot{\gamma} = 10$. They also investigate the validity of the model by examining small-amplitude oscillatory shear flows. The temporal evolution of the shear rate and the polymer stress are seen to be in-phase which qualitatively agrees with the UCM model. They performed quantitative comparisons with analytic solutions when the oscillation had a high frequency and the flow domain was large and found the numerical results obtained in [75] agree very well with the analytical solutions.

Here we present results for simple shear flow where the velocity field is imposed in the simulation domain. The dumbbell distribution functions are initially set to their equilibrium values and the velocity field is given by:

$$u_x = \dot{\gamma} y \tag{6.3.64}$$

$$u_y = 0 \tag{6.3.65}$$

where $\dot{\gamma}$ is the shear rate.

Substituting this velocity field into the Olroyd B constitutive equation (6.2.36) we obtain

$$\begin{pmatrix} T_{xx}, & T_{xy} \\ T_{xy}, & T_{yy} \end{pmatrix} - \lambda_1 \left\{ \begin{pmatrix} 0, & \dot{\gamma} \\ 0, & 0 \end{pmatrix} \begin{pmatrix} T_{xx}, & T_{xy} \\ T_{xy}, & T_{yy} \end{pmatrix} + \begin{pmatrix} T_{xx}, & T_{xy} \\ T_{xy}, & T_{yy} \end{pmatrix} \begin{pmatrix} 0, & 0 \\ \dot{\gamma}, & 0 \end{pmatrix} \right\} = \eta_0 \begin{pmatrix} -2\lambda_2 \dot{\gamma}, & \dot{\gamma} \\ \dot{\gamma}, & 0 \end{pmatrix}, \tag{6.3.66}$$

which upon solving this system yields

$$T_{xx} = 2\eta_0(\lambda_1 - \lambda_2)\dot{\gamma}^2, \tag{6.3.67}$$

$$T_{yy} = 0, \tag{6.3.68}$$

$$T_{xy} = \eta_0\dot{\gamma}. \tag{6.3.69}$$

In Figures 6.3.1 and 6.3.3, we see excellent agreement between the numerical results and the analytical solutions for the components of the stress tensor for three different relaxation times and different shear rates. These simulations were performed on a 150×50 lattice. The simulation was stopped when no change in time was observed. The simulation was then performed on various sized lattices in order to test the order of convergence. The error Err of the viscoelastic tensor components is given by

$$Err = \sqrt{\frac{1}{N}\sum^{N} |\tilde{T}_{P,\alpha\beta} - T_{P,\alpha\beta}|^2} \tag{6.3.70}$$

where N is the number of points evaluated, $\tilde{T}_{P,\alpha\beta}$ is the result of the simulation and $T_{P,\alpha\beta}$ is the analytic result. The results in Figure 6.3.2 indicate second order accuracy for two different $\dot{\gamma}$.

To check the temporal evolution of T_p, the start up shear flow is chosen on the same size lattice to the previous test. The time dependent components of the stress tensor are given by Huilgol and Phan-Thien [48] as

$$T_{P,xx}(t) = 2\eta_p\lambda_1\dot{\gamma}^2\left(1 - e^{-t/\lambda_1}\right) - 2\eta_p\dot{\gamma}^2 t e^{-t/\lambda_1} \tag{6.3.71}$$

$$T_{P,xy}(t) = \eta_p\dot{\gamma}\left(1 - e^{-t/\lambda_1}\right) \tag{6.3.72}$$

and we again see excellent agreement with simulated results for start up shear flow in Figure 6.3.4.

6.4 Discussion

In this chapter we have discussed some lattice Boltzmann methods for viscoelastic flows. These can be classified as either multi-relaxation models or models based on a direct discretisation of the Fokker-Planck equation on a

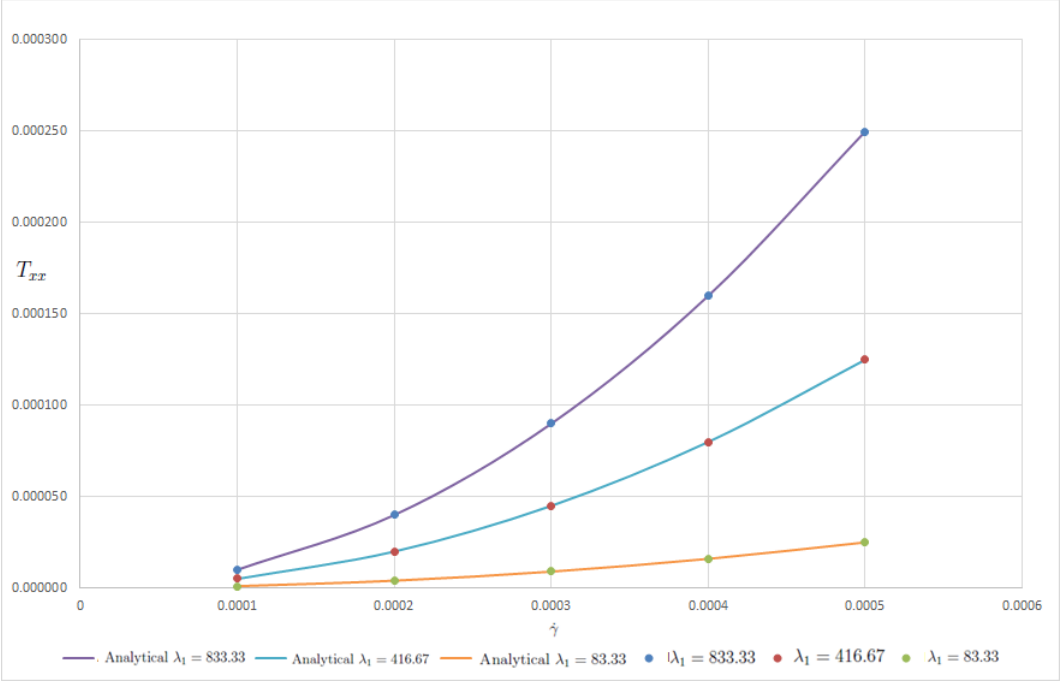

Figure 6.3.1: Comparison of simulation results with the analytical solution at steady state T_{xx} in simple shear with $\lambda = 83.33$, $\lambda = 416.67$ and $\lambda = 833.33$ at different shear rates $\dot{\gamma}$. These simulations were performed on a 150×50 lattice.

lattice. The multi-relaxation models proposed by Giraud et al. [31, 32] take advantage of the LBM framework, incorporating viscoelastic effects into the collision operator, so that the characteristic quantities of complex fluids are given purely in terms of lattice moments. The ability to tune the collision matrix gives these models the potential to recover the constitutive equation of choice without resorting to additional numerical differentiation of macroscopic quantities. However the relation between lattice moments and viscoelastic properties is not well understood at present. The models based on discretising the lattice Fokker-Planck equation have a firm mathematical basis and promise to be a competitive alternative to macroscopic numerical models for polymeric fluids, especially for the problems defined in irregular geometries and multi-phase flows, where lattice Boltzmann methods already have an advantage over traditional numerical schemes. Here we have presented results validating the model by Onishi et al. [75] in the cases of steady shear flow and start up shear flow where we demonstrate excellent agreement with the analytic results.

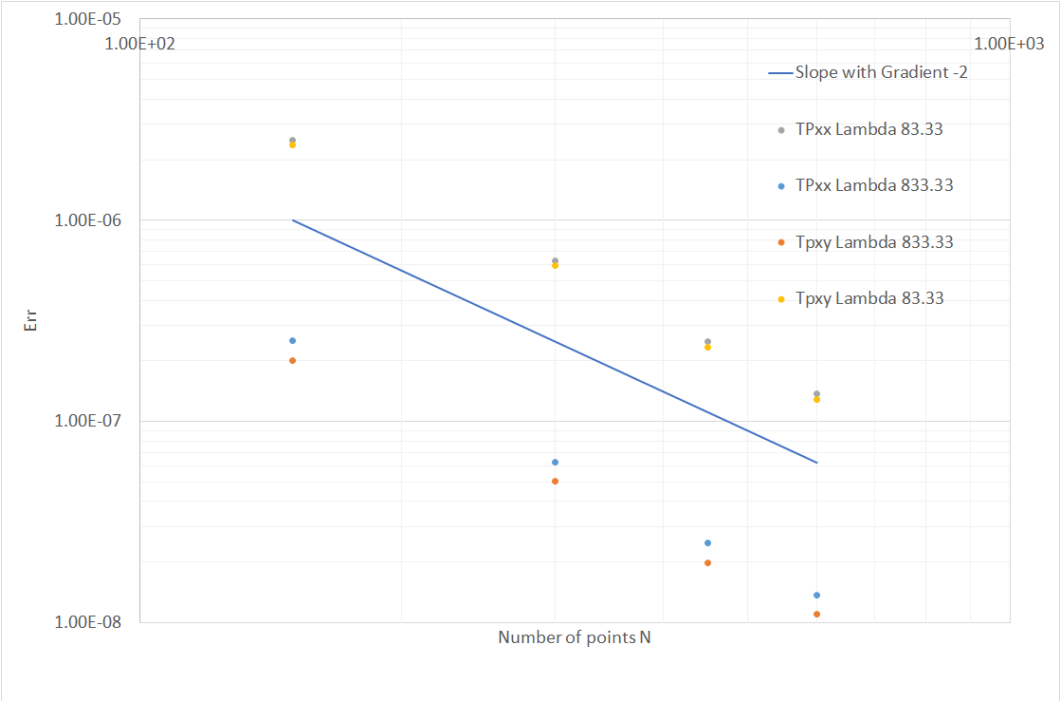

Figure 6.3.2: Err of $T_{P,xx}$ and $T_{P,xy}$ at different spacial resolutions N.

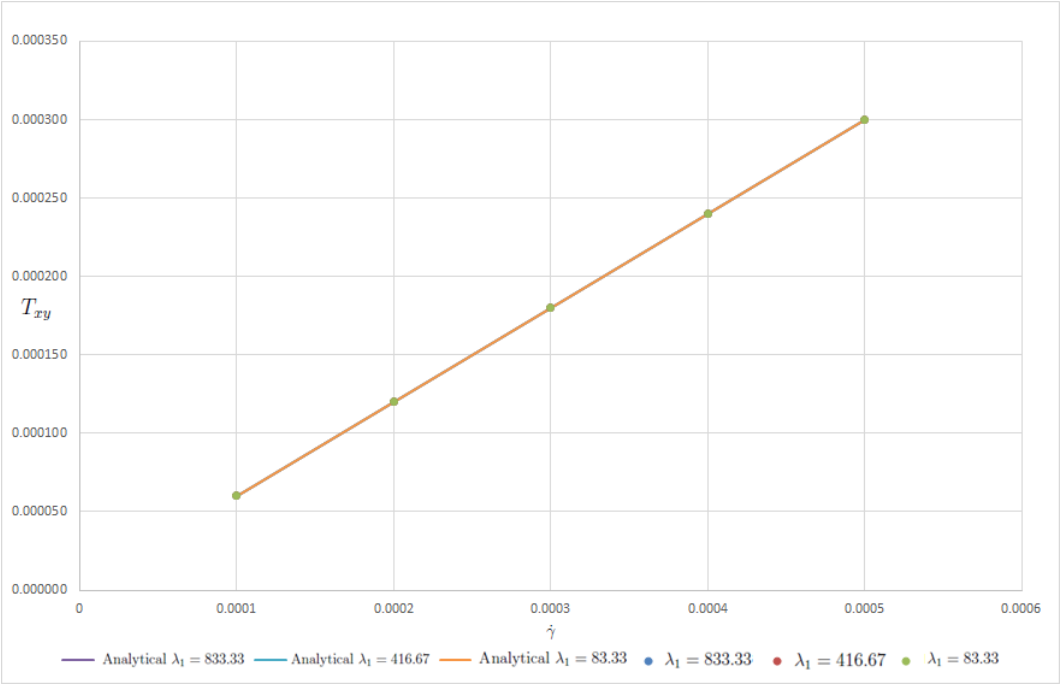

Figure 6.3.3: Comparison of simulation results with the analytical solution at steady state T_{xy} in simple shear with $\lambda = 83.33$, $\lambda = 416.67$ and $\lambda = 833.33$ at different shear rates $\dot{\gamma}$.

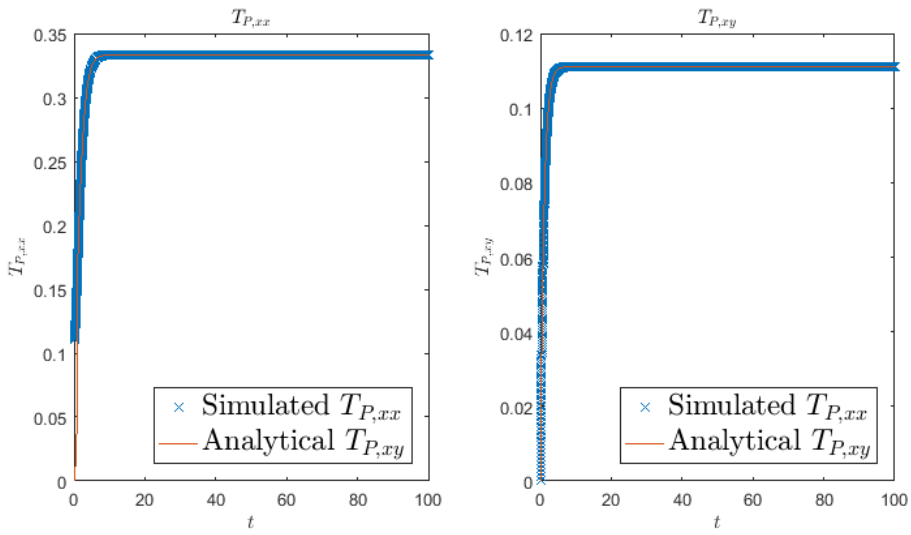

Figure 6.3.4: Comparison of evolution of computational and analytical solution for $T_{P,xx}$ and $T_{P,xy}$.

Chapter 7

LBM for FENE model

The numerical modelling of complex fluids such as colloidal suspensions, polymer solutions and melts, and amphiphilic fluids is very important for many applications. Collodial suspensions are found throughout nature for example milk and blood and are used for a wide variety of purposes, gelofusine is a colloid which is used as an blood replacement if a significant amount of blood has been lost and cranberry glass is made by adding colloidal gold to molten glass. As the Lattice Boltzmann method has been used for flows of Newtonian fluids, due to its advantages in modelling flows in complex geometries (such as flow through porous media), flows of multiple fluids and its amenability to parallel computing [18, 100, 17]. Traditionally flows of complex fluids have been modelled numerically by coupling approximate macroscopic constitutive relations for the stress tensor with a Navier-Stokes description for the solvent.

There has been many recent developments of the LBM directed at modelling collodial suspensions [76, 55, 47], liquid crystals [24] and amphiphilic fluids [14, 72, 63]. These models tend to fall into two distinct categories, top down and bottom up. In the top down approach epitomised in Denniston et al. [24], a thermodynamic potential is used to recover the macroscopic target equations. For a bottom up approach the dynamics of complex fluids is modelled at the kinetic level in order to recover required macroscopic phenomena. The amphiphilic fluid model which reproduces the self-assembled micellar structures [72, 63] is important as it motivated the novel approach of Onishi et al.[75] for modelling polymeric liquids. In that model, viscoelastic stresses of polymeric liquids are evaluated as the net effect of the motion of underlying polymers.

The dynamics of the polymers is modelled based on kinetic theory for polymer solutions. This model is successful at modelling infinitely extendible dumbbells which have closed formed macroscopic constitutive equations.

However, a major problem is that many kinetic theory models for polymeric liquids, such as the FENE dumbbell model, cannot be formulated in terms of closed form constitutive equations. In most approaches a macroscopic flow solver is coupled with microscopic Brownian dynamics (BD) simulations. One can derive an Itô stochastic differential equation which, under certain conditions is equivalent to the Fokker-Planck equation. Thus, the solution of closed form differential or integral constitutive equations can be avoided and replaced with the solution of Itô type stochastic differential equations for the conformations of the polymer molecules describing the coarse grained microstructure. The elastic stress and other macroscopic quantities are then computed by means of ensemble averages.

Since the pioneering work by Laso and Öttinger [57], with the CONNFFESSITT method, micro-macro simulations have become increasingly popular as they have opened up exciting possibilities for incorporating more physics of polymeric fluids into kinetic theory models. The idea to solve the Fokker-Planck equation for the configurational pdf has great value in numerical computations as it has been shown that the direct solution of the Fokker-Planck equation can be much more efficient than stochastic methods in the case of homogeneous flows [64]. Recently Moroni et al. [71] proposed using a lattice Boltzmann style method for solving the Fokker-Planck equation on a lattice. They expanded the Fokker-Planck collision operator in a sequence of Hermite polynomials to account for the diffusion term. This approach is amenable when examining weak flows, as for strong flows one would require a large number of terms to account for the large departure from equilibrium. Recently Singh et al. [96] and Ammar [2] independently developed similar lattice Boltzmann schemes for the Fokker-Planck equation. Essentially these works used the fact that the Fokker-Planck equation is an advection-diffusion equation in configuration space which can be simulated by breaking momentum conservation in the LB framework [96]. Computationally the advantage of the method by Onishi et al. [75] is that it requires a single lattice which is used for both the solvent distribution functions and the configurational distribution functions

where as the method described by Ammar [2] and Singh et al. [96] require solving a lattice Fokker-Planck equation in configurational space to recover the elastic stress at every single lattice site in physical space.

In this chapter we develop a lattice Boltzmann style solver for the Fokker-Planck equation using a single lattice, similar to the framework developed by Onishi et al., but instead using the FENE force law which has a very different equilibrium solution. There are two major theoretical differences between what we have developed and the model by Onishi et al. [75]. Firstly they assume that the configurational distribution functions will be similar to the equilibrium solution which for Hookean dumbbells is similar to the equilibrium solution for the Lattice Boltzmann equation, and then use Gauss-Hermite quadrature to calculated the necessary moments of the distribution functions to recover the elastic stress. Secondly the configuration space for Hookean dumbbells is $\mathbb{R}^2$ (for 2d dumbbells) or $\mathbb{R}^3$ (for 3d dumbbells). For FENE dumbbells the equilibrium solution has a very different form and so the Hermite weighting function is not appropriate and the configurational space is a disk bounded by the maximum permissible length $\sqrt{b}$ and so we require a different quadrature rule that has been developed here. This leads different discrete equilibrium distribution functions and to the use of a D2Q7 lattice for the polymeric distribution functions and the solvent distribution functions so a new coupling is required.

After discussing this new solver for simulating the flow of FENE fluids we will discuss the FENE solver by Ammar [2] in more detail and then present results using both approaches.

7.1 A LBM for FENE fluids

7.1.1 Kinetic theory description of the Fokker-Planck equation for FENE dumbbells

Traditionally viscoelastic stresses have been modelled by solving approximate macroscopic constitutive equations such as the upper-convected Maxwell (UCM) model

$$\mathbf{T} + \lambda_1 \overset{\nabla}{\mathbf{T}} = \eta_0 \dot{\gamma}, \tag{7.1.1}$$

where the shear rate is given by

$$\dot{\gamma} = (\nabla \mathbf{u} + (\nabla \mathbf{u})^{\dagger}) \tag{7.1.2}$$

and the upper-convected derivative is defined by

$$\overset{\nabla}{\mathbf{T}} = \frac{\partial \mathbf{T}}{\partial t} + \mathbf{u} \cdot \mathbf{T} - \nabla \mathbf{u} \cdot \mathbf{T} - \mathbf{T} \cdot (\nabla \mathbf{u})^{\dagger} \tag{7.1.3}$$

where $\mathbf{T}$ is the extra stress tensor, $\eta_0 = \eta_p + \eta_s$ is the sum of the polymeric viscosity and the solvent viscosity, and λ_1 is the polymer relaxation time. As we have seen previously the UCM model can be derived based on simple kinetic theory for polymeric liquids, where the polymer solution is modelled by a Newtonian solvent and dumbbells dispersed in the solvent. The dumbbells consist of two beads connected by a spring. For the UCM model the spring force is assumed to be Hookean, $\mathbf{F} = H\mathbf{Q}$ where H is the spring constant. The viscoelastic stresses are computed based on ensemble averages of the configuration of the dumbbells and are given by the Kramers expression

$$\mathbf{T}_p = -n_p \langle \mathbf{Q}\mathbf{F} \rangle + n_p k_b T_m \mathbf{I} \tag{7.1.4}$$

where $\mathbf{T}_p$ is the polymeric stress tensor, n_p is the number density of the dumbbells, k_b is the Boltzmann constant, and T_m is the mean temperature. $\langle \cdot \rangle$ is the ensemble average which is weighted by the configurational distribution function $\psi(\mathbf{Q}, \mathbf{x}, t)$, which indicates the probability of finding a dumbbell with configuration $\mathbf{Q}$ at $(\mathbf{x}, t)$. The time evolution of ψ obeys a Fokker-Planck equation

$$\frac{\partial \psi}{\partial t} = -\mathbf{u} \cdot \nabla \psi - \frac{\partial}{\partial \mathbf{Q}} \cdot [\kappa \cdot \mathbf{Q} \psi] + \frac{2 k_b T_m}{\zeta} \frac{\partial}{\partial \mathbf{Q}} \left[\frac{\partial \psi}{\partial \mathbf{Q}} + \mathbf{F} \frac{\psi}{k_b T_m} \right] \tag{7.1.5}$$

where ζ is the friction coefficient. Multiplying both sides by $\mathbf{Q}\mathbf{Q}$ and integrating over the configurational space leads to the dynamical equation of the second moment of ψ

$$\overset{\nabla}{\langle \mathbf{Q}\mathbf{Q} \rangle} = \frac{4 k_b T_m}{\zeta} \mathbf{I} - \frac{4}{\zeta} \langle \mathbf{Q}\mathbf{F} \rangle \tag{7.1.6}$$

and from this and Kramers expression for the stress tensor we can recover the UCM model with $\lambda_1 = \zeta/4H$ and $\eta_p = n_p k_b T_m \lambda_1$ [80].

7.1.2 Discrete kinetic model for FENE dumbbells

The aim is to derive a discrete kinetic equation equivalent to the Fokker-Planck equation, so that the macroscopic physics can be recovered and viscoelastic stresses evaluated efficiently with the configurational distribution functions in discrete space and time.

The derivation of the kinetic equation follows the methodology described by Onishi et al. [75], with important changes to incorporate different equilibrium distribution function associated with the FENE model as opposed to the Oldroyd-B or FENE-P model.

The non-dimensional equilibrium distribution function for the FENE model, $\psi^{eq}(\mathbf{Q})$, in the 2D case is given in Lozinski et al. [65]

$$\psi^{eq}(\mathbf{Q}) = \frac{b+2}{2\pi b}\left(1 - \frac{\mathbf{Q}\cdot\mathbf{Q}}{b}\right)^{b/2} \tag{7.1.7}$$

where $\sqrt{b}$ is the dimensionless maximum spring extensibility with the nondimensional force law given by

$$\mathbf{F}(\mathbf{Q}) = \frac{\mathbf{Q}}{1 - \frac{\mathbf{Q}\cdot\mathbf{Q}}{b}}. \tag{7.1.8}$$

In practice b is usually chosen to be between 20 and 100 as 20 is at the lower end of what is physically meaningful and values larger than 100 cause only minor modifications of the Oldroyd-B model. Note that b is not a free parameter, but roughly the number of momomer units represented by the dumbbell, and therefore b should be a large number [44] and it should be noted that in the limit $b \to \infty$ we recover the Hookean dumbbell model.

To illustrate the discretisation procedure, we introduce a new variable, ψ, related to ϕ by

$$\psi(\mathbf{Q}) = \phi(\mathbf{Q})\frac{b+2}{2\pi b}\left(1 - \frac{\mathbf{Q}\cdot\mathbf{Q}}{b}\right)^{b/2}. \tag{7.1.9}$$

The moments of ψ involve integrals of the form,

$$\langle B(\mathbf{Q})\rangle = \int_{|\mathbf{Q}|\leq\sqrt{b}} B(\mathbf{Q})\psi(\mathbf{Q})d\mathbf{Q} = \frac{b+2}{2\pi}\int_{|\mathbf{x}|\leq 1} B(\sqrt{b}\mathbf{x})\phi(\sqrt{b}\mathbf{x})(1-\mathbf{x}^2)^{b/2}d\mathbf{x} \tag{7.1.10}$$

where we have used the change of variable $\mathbf{x} = \mathbf{Q}/\sqrt{b}$ with Jacobian b.

Consider the quadrature rule

$$\int_{|\mathbf{y}|\leq 1} y_\alpha^m (1-\mathbf{y}\cdot\mathbf{y})^{b/2}d\mathbf{y} = \sum_i^N \lambda_i y_{i\alpha}^m, \tag{7.1.11}$$

where the weights λ_i and nodes y_i are chosen so that the rule is exact up to a certain order depending on the number of vectors N, used to span the discrete space. With such a quadrature rule one would be able to compute the moments of ψ in continuous space in discrete space.

Generalised Gauss Quadrature Rule

We need to derive an appropriate Gaussian quadrature so we evaluate integrals of the form

$$I = \int_{x^2+y^2\leq 1} (1-(x^2+y^2))^{b/2}x^i y^j dxdy. \tag{7.1.12}$$

Making the substitution $x = \rho\cos\theta$ and $y = \rho\sin\theta$, this integral becomes

$$I = \int_{-1}^{1} |\rho|(1-\rho^2)^{b/2}\rho^{i+j}d\rho \int_{-\pi/2}^{\pi/2} \cos^i\theta\sin^j\theta d\theta \tag{7.1.13}$$

and then the substitution $t = \sin\theta$ yields

$$I = \underbrace{\int_{-1}^{1} |\rho|(1-\rho^2)^{b/2}\rho^{i+j}d\rho}_{\text{Have to derive a new Gaussian rule}} \underbrace{\int_{-1}^{1} (1-t^2)^{i/2}t^j(1-t^2)^{-1/2}dt}_{\text{Gauss Chebyshev}} \tag{7.1.14}$$

Consider the set of polynomials orthogonal on $(-1,1)$ with respect to the weight function $|\rho|(1-\rho^2)^{b/2}$. Let $P_n(x)$ be the element of the set of degree n. If

$$\int_{-1}^{1} w(x)f(x)dx \approx \sum_{i=1}^{n} A_i f(x_i) \tag{7.1.15}$$

then this rule is exact for all polynomials of degree $2n-1$ or less if the weights A_i are given by

$$A_i = \frac{\int_{-1}^{1} w(x) P_{n-1}^2(x) dx}{P_n'(x_i) P_{n-1}(x_i)} \tag{7.1.16}$$

and the nodes x_i correspond to the zeros of the orthogonal polynomial P_n and the orthogonal polynomials (of the form $P_n(x) = x^n + a_{n,n-1}x^{n-1} + \cdots + a_{n,1}x + a_{n,0}$) are derived by use of a recursive relation of the form

$$P_n(x) = (x - \beta_n)P_{n-1}(x) - \gamma_n P_{n-2}(x), \quad n = 2, 3, 4, \ldots, \tag{7.1.17}$$

$$P_1(x) = x - \beta_1, \quad P_0(x) = 1 \tag{7.1.18}$$

where

$$\beta_n = \frac{I_{n,n-1}}{I_{n-1,n-1}} + a_{n-1,n-2} \tag{7.1.19}$$

and

$$\gamma_n = \frac{I_{n-1,n-1}}{I_{n-2,n-2}} \tag{7.1.20}$$

in which

$$I_{n,m} = \int_{-1}^{1} w(x) x^n P_m(x) dx. \tag{7.1.21}$$

The first two orthogonal polynomials are

$$P_0(x) = 1, \quad P_1(x) = x, \tag{7.1.22}$$

and then using the recursive relation the next two polynomials are

$$P_2(x) = x^2 - \frac{2}{b+4}, \quad P_3(x) = x^3 - \frac{4}{b+6}x, \tag{7.1.23}$$

and the corresponding weights are given by the values in the Table:7.1 so that

$$\int_{-1}^{1} |\rho| (1-\rho^2)^{b/2} \rho^l d\rho = \sum_{k=0}^{2} x_k^l A_k \tag{7.1.24}$$

x_i	A_i
0	$1/(b+4)$
$-\sqrt{4/(b+6)}$	$(b+6)/(2(b+2)(b+4))$
$\sqrt{4/(b+6)}$	$(b+6)/(2(b+2)(b+4))$

Table 7.1: Nodes and Weights for derived quadrature rule.

for $l \leq 5$.

A third order scheme for Gauss-Chebyshev quadrature is

$$\int_{-1}^{1}(1-x^2)^{-1/2}x^l dt = \sum_{j=0}^{2} x_j^l B_i \tag{7.1.25}$$

where the corresponding weights are given in the Table:7.2 for $l \leq 5$.

x_i	B_i
0	$\pi/3$
$-\sqrt{3}/2$	$\pi/3$
$\sqrt{3}/2$	$\pi/3$

Table 7.2: Nodes and Weights for Gauss-Chebyshev quadrature rule.

Now we have separate Gaussian rules for each of the integrals in (7.1.14). We take their Cartesian product to form the new quadrature rule, recalling that $x = \rho\cos\theta$ and $y = \rho\sin\theta$, so that

$$\int_{|\mathbf{x}|\leq 1} f(x,y)(1-\mathbf{x}^2)^{b/2}d\mathbf{x} = \sum_{i=0}^{6} f(x_i,y_i)\lambda_i, \tag{7.1.26}$$

where the nodes and weights are defined in Table:7.3 This quadrature rule approximates integrals over the disk by the use of nodes at the vertices of a hexagon. One way to derive the Lattice Boltzmann method is by discretising the Boltzmann equation using Gauss-Hermite quadrature. The integral is over the domain $\mathbb{R}^2$. If $\mathbb{R}^2$ is approximated as an infinitely large square one recovers the D2Q9 lattice and if it is approximated as an infinitely large disk the D2Q7 lattice is recovered. The difference between the original FHP (D2Q7) lattice and our Fokker-Planck lattice is the length of the lattice vectors. In

i	x_i	y_i	λ_i
0	0	0	$\pi/(b+4)$
1	$-\sqrt{(4/(b+6))}/2$	$\sqrt{(4/(b+6))}\sqrt{3}/2$	$\frac{\pi}{3}\frac{(b+6)}{(2(b+2)(b+4))}$
2	$-\sqrt{(4/(b+6))}/2$	$-\sqrt{(4/(b+6))}\sqrt{3}/2$	$\frac{\pi}{3}\frac{(b+6)}{(2(b+2)(b+4))}$
3	$-\sqrt{(4/(b+6))}$	0	$\frac{\pi}{3}\frac{(b+6)}{(2(b+2)(b+4))}$
4	$\sqrt{(4/(b+6))}/2$	$-\sqrt{(4/(b+6))}\sqrt{3}/2$	$\frac{\pi}{3}\frac{(b+6)}{(2(b+2)(b+4))}$
5	$\sqrt{(4/(b+6))}/2$	$\sqrt{(4/(b+6))}\sqrt{3}/2$	$\frac{\pi}{3}\frac{(b+6)}{(2(b+2)(b+4))}$
6	$\sqrt{(4/(b+6))}$	0	$\frac{\pi}{3}\frac{(b+6)}{(2(b+2)(b+4))}$

Table 7.3: Nodes and Weights for quadrature rule for I.

the original FHP lattice for isothermal fluids the length of the lattice vector has no physical significance [42], whereas here we have the length of the lattice vector depending on b.

Returning to the discretisation of the configuration space, by applying the Gaussian quadrature, $\langle B(\mathbf{Q})\rangle$ can be evaluated by the weighted summation with a new weight ψ_j,

$$\langle B(\mathbf{Q})\rangle = \sum_{j}^{N} \psi_j B(\mathbf{Q}_j) \tag{7.1.27}$$

where

$$\psi_j = \frac{b+2}{2\pi}\lambda_j \phi(\mathbf{Q}_j). \tag{7.1.28}$$

is the configurational distribution function in discrete configuration space with $\mathbf{Q}_j = \sqrt{b}\mathbf{x}_j$.

In order to derive the discrete equilibrium distribution function, we start by substituting (7.1.9) into (7.1.28)

$$\psi_j = \frac{b+2}{2\pi}\lambda_j \phi(\mathbf{Q}_j) = \frac{b+2}{2\pi}\lambda_j \psi(\mathbf{Q_j})\frac{2\pi b}{b+2}\left(1 - \frac{\mathbf{Q_j}\cdot\mathbf{Q_j}}{b}\right)^{-b/2}$$

and then evaluating this expression at equilibrium using (7.1.7) we obtain

$$\begin{aligned}\psi_j^{eq} &= \frac{b+2}{2\pi}\lambda_j\psi^{eq}(\mathbf{Q_j})\frac{2\pi b}{b+2}\left(1-\frac{\mathbf{Q_j}\cdot\mathbf{Q_j}}{b}\right)^{-b/2} \\ &= \frac{b+2}{2\pi}\lambda_j\frac{b+2}{2\pi b}\left(1-\frac{\mathbf{Q_j}\cdot\mathbf{Q_j}}{b}\right)^{b/2}\frac{2\pi b}{b+2}\left(1-\frac{\mathbf{Q_j}\cdot\mathbf{Q_j}}{b}\right)^{-b/2}\end{aligned}$$

so that

$$\psi_j^{eq} = \lambda_j\left(\frac{b+2}{2\pi}\right). \tag{7.1.29}$$

The time evolution equation for ψ_j can be derived by referring to the Fokker-Planck equation (7.1.5) and collecting terms based on their physical contributions

$$\frac{\partial\psi_j}{\partial t} = -\mathbf{v}\cdot\nabla\psi_j + \Omega_{\psi,j} + M_j, \tag{7.1.30}$$

where $\Omega_{\psi,j}$ describes the transition process for the dumbbells to approach an equilibrium state, due to the competition between the thermal fluctuation and the spring force between the connected bead and M_j accounts for the effects of the elongation and rotation of the solvent on the polymer chains. The term $-\mathbf{v}\cdot\nabla\psi_j$ accounts for the convection of the dumbbells based on the solvent flow.

The dynamics to approach the equilibrium states can be approximated with a relaxation model when the system is close to its equilibrium. In this study, a single time relaxation model similar to the BGK model for the velocity distribution function in the standard LBM is employed for $\Omega_{\psi,j}$

$$\Omega_{\psi,j} = -\frac{1}{\tau_{\psi_j}}\left(\psi_j - \psi_j^{eq}\right), \tag{7.1.31}$$

where τ_{ψ_j} is the relaxation time for ψ_j.

Next the discrete model to account for effects of solvent M_j is derived. Consider the discretisation of the corresponding term from equation (7.1.5)

$$S = -\frac{\partial}{\partial\mathbf{Q}}\cdot\left[\boldsymbol{\kappa}\cdot\mathbf{Q}\psi\right]. \tag{7.1.32}$$

Use of the new variable defined by (7.1.9) gives

$$S = -\frac{\partial}{\partial \mathbf{Q}} \cdot \left[\boldsymbol{\kappa} \cdot \mathbf{Q} \phi(\mathbf{Q}) \frac{b+2}{2\pi b} \left(1 - \frac{\mathbf{Q} \cdot \mathbf{Q}}{b} \right)^{b/2} \right] \tag{7.1.33}$$

and then performing the derivative using the product rule yields

$$S = -\left(\frac{b+2}{2\pi b} \right) \left(\boldsymbol{\kappa} : \mathbf{Q} \frac{\partial}{\partial \mathbf{Q}} \left[\phi(\mathbf{Q}) \left(1 - \frac{\mathbf{Q} \cdot \mathbf{Q}}{b} \right)^{b/2} \right] + \boldsymbol{\kappa} : \phi(\mathbf{Q}) \left(1 - \frac{\mathbf{Q} \cdot \mathbf{Q}}{b} \right)^{b/2} \mathbf{I} \right) \tag{7.1.34}$$

and then using the product rule on the remaining derivative gives

$$\begin{aligned} S = -\left(\frac{b+2}{2\pi b} \right) \Bigg(& \boldsymbol{\kappa} : \mathbf{Q} \frac{\partial}{\partial \mathbf{Q}} \left\{ \phi(\mathbf{Q}) \right\} \left(1 - \frac{\mathbf{Q} \cdot \mathbf{Q}}{b} \right)^{b/2} \\ & - \boldsymbol{\kappa} : \mathbf{Q}\mathbf{Q} \left(1 - \frac{\mathbf{Q} \cdot \mathbf{Q}}{b} \right)^{b/2-1} \phi(\mathbf{Q}) + \boldsymbol{\kappa} : \phi(\mathbf{Q}) \left(1 - \frac{\mathbf{Q} \cdot \mathbf{Q}}{b} \right)^{b/2} \mathbf{I} \Bigg) . \end{aligned} \tag{7.1.35}$$

We then integrate this term over configurational space and discretise the inte-

gral using Gauss-Jacobi quadrature in a similar manner as before

$$\begin{aligned}
\int S d\mathbf{Q} &= \left(\frac{b+2}{2\pi b}\right) \int_{|\mathbf{Q}|\leq\sqrt{b}} \left\{ \left(1 - \frac{\mathbf{Q}\cdot\mathbf{Q}}{b}\right)^{b/2} \left[-\boldsymbol{\kappa} : \mathbf{Q} \frac{\partial \phi(\mathbf{Q})}{\partial \mathbf{Q}} - \boldsymbol{\kappa} : \phi(\mathbf{Q}) \mathbf{I} \right] \right. \\
&\quad \left. + \left(1 - \frac{\mathbf{Q}\cdot\mathbf{Q}}{b}\right)^{b/2-1} \left[\boldsymbol{\kappa} : \mathbf{Q}\mathbf{Q}\phi(\mathbf{Q}) \right] \right\} d\mathbf{Q} \\
&= \left(\frac{b+2}{2\pi}\right) \int_{|\mathbf{x}|\leq 1} \left\{ (1 - \mathbf{x}\cdot\mathbf{x})^{b/2} \left[-\boldsymbol{\kappa} : \mathbf{x}\sqrt{b} \frac{\partial \phi(\mathbf{x})}{\partial \mathbf{x}} - \boldsymbol{\kappa} : \phi(\mathbf{x}\sqrt{b}) \mathbf{I} \right. \right. \\
&\quad \left. \left. + (1 - \mathbf{x}\cdot\mathbf{x})^{-1} \boldsymbol{\kappa} : \mathbf{x}\mathbf{x} b \phi(\mathbf{x}\sqrt{\mathbf{b}}) \right] \right\} d\mathbf{x} \\
&\approx \left(\frac{b+2}{2\pi}\right) \sum_j^N \lambda_j \left[\left(1 - \frac{\mathbf{Q}_j\cdot\mathbf{Q}_j}{b}\right)^{-1} \left[\boldsymbol{\kappa} : \mathbf{Q}_j\mathbf{Q}_j\phi(\mathbf{Q}_j) \right] \right. \\
&\quad \left. -\boldsymbol{\kappa} : \mathbf{I}\phi(\mathbf{Q}_j) - \boldsymbol{\kappa} : \mathbf{Q}_j \frac{\partial \phi(\mathbf{Q})}{\partial \mathbf{Q}}\bigg|_{\mathbf{Q}=\mathbf{Q}_j} \right] \\
&= \sum_j^N \left[\left(1 - \frac{\mathbf{Q}_j\cdot\mathbf{Q}_j}{b}\right)^{-1} \left[\boldsymbol{\kappa} : \mathbf{Q}_j\mathbf{Q}_j\psi_j \right] - \boldsymbol{\kappa} : \mathbf{I}\psi_j - \boldsymbol{\kappa} : \mathbf{Q}_j \frac{\partial \psi_j}{\partial \mathbf{Q}} \right] \\
&= \sum_j M_j
\end{aligned}$$

where

$$\frac{\partial \psi_j}{\partial \mathbf{Q}} = \left(\frac{b+2}{2\pi}\right) \lambda_j \frac{\partial \phi(\mathbf{Q})}{\partial \mathbf{Q}}\bigg|_{\mathbf{Q}=\mathbf{Q}_j} \tag{7.1.36}$$

and

$$M_j = \left(1 - \frac{\mathbf{Q}_j\cdot\mathbf{Q}_j}{b}\right)^{-1} \left[\boldsymbol{\kappa} : \mathbf{Q}_j\mathbf{Q}_j\psi_j \right] - \boldsymbol{\kappa} : \mathbf{I}\psi_j - \boldsymbol{\kappa} : \mathbf{Q}_j \frac{\partial \psi_j}{\partial \mathbf{Q}} \tag{7.1.37}$$

$$= \boldsymbol{\kappa} : \left[\left(1 - \frac{\mathbf{Q}_j\cdot\mathbf{Q}_j}{b}\right)^{-1} \mathbf{Q}_j\mathbf{Q}_j - \mathbf{I} \right] \psi_j - \boldsymbol{\kappa} : \mathbf{Q}_j \frac{\partial \psi_j}{\partial \mathbf{Q}}. \tag{7.1.38}$$

It should be noted that this expression for M_j involves a partial derivative in continuous configuration space of a function ϕ evaluated at the points $\mathbf{Q}_j$. To facilitate the discretisation of this partial derivative, a new form for the M_j term is proposed such that it recovers the correct dynamics at the continuous

level, at least, up to the second moment of $\mathbf{Q}$

$$M_0 = 2\begin{pmatrix} -1 & 0 \\ 0 & -1 \end{pmatrix} : (\kappa \cdot \langle \mathbf{Q}_j \mathbf{Q}_j \rangle) \tag{7.1.39}$$

$$M_1 = \begin{pmatrix} 0 & -1/\sqrt{3} \\ -1/\sqrt{3} & 2/3 \end{pmatrix} : (\kappa \cdot \langle \mathbf{Q}_j \mathbf{Q}_j \rangle) \tag{7.1.40}$$

$$M_2 = \begin{pmatrix} 1 & 0 \\ 0 & -1/3 \end{pmatrix} : (\kappa \cdot \langle \mathbf{Q}_j \mathbf{Q}_j \rangle) \tag{7.1.41}$$

$$M_3 = \begin{pmatrix} 0 & 1/\sqrt{3} \\ 1/\sqrt{3} & 2/3 \end{pmatrix} : (\kappa \cdot \langle \mathbf{Q}_j \mathbf{Q}_j \rangle) \tag{7.1.42}$$

$$M_4 = \begin{pmatrix} 0 & -1/\sqrt{3} \\ -1/\sqrt{3} & 2/3 \end{pmatrix} : (\kappa \cdot \langle \mathbf{Q}_j \mathbf{Q}_j \rangle) \tag{7.1.43}$$

$$M_5 = \begin{pmatrix} 1 & 0 \\ 0 & -1/3 \end{pmatrix} : (\kappa \cdot \langle \mathbf{Q}_j \mathbf{Q}_j \rangle) \tag{7.1.44}$$

$$M_6 = \begin{pmatrix} 0 & 1/\sqrt{3} \\ 1/\sqrt{3} & 2/3 \end{pmatrix} : (\kappa \cdot \langle \mathbf{Q}_j \mathbf{Q}_j \rangle) \tag{7.1.45}$$

$$\tag{7.1.46}$$

so

$$\sum_j M_j = 0, \quad \sum_j \mathbf{Q}_j M_j = 0 \tag{7.1.47}$$

$$\sum_j \mathbf{Q}_j \mathbf{Q}_j M_j = \kappa \cdot \langle \mathbf{Q}_j \mathbf{Q}_j \rangle + \langle \mathbf{Q}_j \mathbf{Q}_j \rangle \cdot \kappa^T. \tag{7.1.48}$$

Finally discretising equation (7.1.30) in physical space and time, replacing the time derivative by a first order time difference, as in the derivation of the LBGK [81, 17] gives

$$\psi_j(\mathbf{x}, \mathbf{t}+1) - \psi_j(\mathbf{x}, t) = \Delta\psi_j - \frac{1}{\tau_{\psi_j}} \left(\psi_j(\mathbf{x}, \mathbf{t}) - \psi_j^{eq}(\mathbf{x}, \mathbf{t}) \right) + M_j \tag{7.1.49}$$

where $\Delta\psi_j$ is the convection of the dumbbells which can be handled but in the flow geometries we are exploring can be neglected. The viscoelastic stresses

are obtained in the Kramers form

$$\mathbf{T}_p(\mathbf{x},t) = \frac{1-\beta}{We}\left(\frac{b+4}{b}\right)\left(\sum_j \frac{\mathbf{Q}_j\mathbf{Q}_j}{\left(1-\frac{Q_j^2}{b}\right)}(\psi_j - \psi_j^{eq})\right) \tag{7.1.50}$$

where β is the ratio of the solvent viscosity to the total viscosity and We is the Weissenberg number which is the ratio of the elastic forces to the viscous forces.

7.1.3 Coupling with LBM

In this section, the hydrodynamics of the solvent is modelled by the LBM. In the LBM, states of fluids are described by the velocity distribution $f_i(\mathbf{x},t)$ which indicates the probability of having a particle with velocity $\mathbf{c}_i$ at lattice site $\mathbf{x}$ and time t. For ease of coupling with our derived Lattice Fokker Planck model the D2Q7 model is shown here. For such a system, the evolution equation of f_i is given by the LBGK equation

$$f_i(\mathbf{x}+\mathbf{c}_i, t+1) - f_i(\mathbf{x},t) = -\frac{1}{\tau_n}[f_i(\mathbf{x},t) - f_i^{eq}(\mathbf{x},t)] \tag{7.1.51}$$

with the relaxation time τ_n.

The equilibrium distribution f_i^{eq} depends on local physical quantities such as the number density of particles $n_s = \Sigma_i f_i$ and the flow velocity $\mathbf{u} = \Sigma_i \mathbf{c}_i f_i / n_s$. The constraints on the choice of f_i^{eq} are to conserve mass and momentum during the collision process, and to satisfy isotropy and Galilean invariance. The commonly used equilibrium distribution which satisfies such constraints can be obtained by expanding the Maxwell-Boltzmann distribution up to second-order in $\mathbf{u}$:

$$f_i^{eq} = n_s\left[\frac{1-z}{6} + \frac{\mathbf{c}_i\cdot\mathbf{u}}{3c^2} + \frac{2(\mathbf{c}_i\cdot\mathbf{u})^2}{3c^4} - \frac{\mathbf{u}^2}{6c^2}\right], \quad i = 1,\ldots,6 \tag{7.1.52}$$

$$f_0^{eq} = n_s\left(z - \frac{u^2}{c^2}\right) \tag{7.1.53}$$

where $c = |\mathbf{c_i}|$ and z is a parameter that controls the speed of sound c_s by

$$c_s = \sqrt{\frac{1-z}{2}}. \tag{7.1.54}$$

A given kinematic viscosity can be achieved by use of the appropriate relaxation time parameter τ_n using the relation

$$\nu = \frac{c^2}{4}\left(\tau_n - \frac{1}{2}\right). \tag{7.1.55}$$

When the expanded Maxwell-Boltzmann distribution is used, equation (7.1.51) recovers the Navier-Stokes equation at the continuous level.

To incorporate the extra stress T_p from the contribution from the dumbbells a modified equilibrium distribution is introduced

$$\begin{aligned} f_i^{eq} &= n_s\left[\frac{1-z}{6} + \frac{\mathbf{c}_i\cdot\mathbf{u}}{3c^2} + \frac{2(\mathbf{c}_i\cdot\mathbf{u})^2}{3c^4} - \frac{\mathbf{u}^2}{6c^2}\right] + T_i, \quad i = 1,\ldots,6 \\ f_0^{eq} &= n_s(z - \frac{u^2}{c^2}) + T_0 \end{aligned} \tag{7.1.56}$$

where

$$T_0 = \frac{1}{c^2}\begin{pmatrix} -1 & 0 \\ 0 & -1 \end{pmatrix} : T_p \quad T_{1,4} = \frac{1}{c^2}\begin{pmatrix} 0 & -1/(2\sqrt{3}) \\ -1/(2\sqrt{3}) & 1/3 \end{pmatrix} : T_p \tag{7.1.57}$$

$$T_{2,5} = \frac{1}{c^2}\begin{pmatrix} 1/2 & 0 \\ 0 & -1/6 \end{pmatrix} : T_p \quad T_{3,6} = \frac{1}{c^2}\begin{pmatrix} 0 & 1/(2\sqrt{3}) \\ 1/(2\sqrt{3}) & 1/3 \end{pmatrix} : T_p. \tag{7.1.58}$$

With the modified equilibrium distribution, the zeroth to second velocity moments are, respectively, calculated as

$$\sum_i f_i^{eq} = n_s, \tag{7.1.59}$$

$$\sum_i \mathbf{c}_i f_i^{eq} = n_s\mathbf{u}, \tag{7.1.60}$$

$$\sum_i \mathbf{c}_i\mathbf{c}_i f_i^{eq} = n_s\mathbf{u}\mathbf{u} + \frac{n_s(1-z)c^2}{2}\mathbf{I} + \mathbf{T}_P. \tag{7.1.61}$$

These results show that the introduction of T_i does not effect the conserva-

tion of mass and the conservation of momentum during the collision process. Using the standard Chapman-Enskog analysis [13], [75], [84] it can be shown that the mass and momentum equations are recovered

$$\frac{\partial \rho}{\partial t} + \nabla \cdot \rho \mathbf{u} = 0, \tag{7.1.62}$$

$$\rho \left(\frac{\partial u}{\partial t} + \mathbf{u} \cdot \nabla \mathbf{u} \right) = -\nabla p - \nabla \cdot \boldsymbol{\sigma} \tag{7.1.63}$$

$$\boldsymbol{\sigma} = \mu_s \dot{\gamma} + \mu_p \mathbf{T}_P \tag{7.1.64}$$

where μ_s is the solvent viscosity and μ_p is the polymeric viscosity.

7.1.4 Lattice Boltzmann method for polymer kinetic theory

Ammar [2] presents an alternative scheme for solving the Fokker-Planck equation. Starting with the usual LBGK for fluids

$$f_i(\mathbf{x} + \mathbf{c}_i \Delta t, t + \Delta t) - f_i(\mathbf{x}, t) = -\frac{1}{\tau}(f_i(\mathbf{x}, t) - f_i^{eq}(\mathbf{x}, t)) \tag{7.1.65}$$

for $i = 0, \ldots, 8$ with the D2Q9 lattice. Denote c as the ratio between the lattice spacing Δx and the time step Δt. The local equilibrium distribution function f_i^{eq} is given by

$$f_i^{eq}(\mathbf{x}, t) = \left(1 + \frac{\mathbf{c}_i \cdot \mathbf{u}}{c_s^2} + \frac{(\mathbf{c}_i \cdot \mathbf{u})^2}{2c_s^4} - \frac{|\mathbf{u}|^2}{2c_s^2} \right) \omega_i \psi \tag{7.1.66}$$

where c_s is the so called lattice speed of sound in the LBM for fluids and is given by $c_s = c/\sqrt{3}$, and $\mathbf{u}$ is a convection vector that is not the same as the physical velocity. The weights ω_i are the normal lattice Boltzmann weights. The distribution functions and the equilibrium distribution functions

are subject to the following conditions

$$\sum_i f_i = \sum_i f_i^{eq} = \psi \tag{7.1.67}$$

$$\sum_i \mathbf{c}_i f_i^{eq} = \psi \mathbf{u} \tag{7.1.68}$$

$$\sum_i \mathbf{c}_i \mathbf{c}_i f_i^{eq} = \psi(\mathbf{u}\mathbf{u} + c_s^2 \mathbf{I}) \tag{7.1.69}$$

where $\mathbf{I}$ is the identity tensor. To derive the Fokker-Planck equation, apply an expansion similar to the Chapman-Enskog expansion,

$$f_i = f_i^{eq} + \epsilon f_i^{(1)} + \epsilon f_i^{(2)} \tag{7.1.70}$$

$$\frac{\partial}{\partial t} = \epsilon \frac{\partial}{\partial t_1} + \epsilon^2 \frac{\partial}{\partial t_2} \tag{7.1.71}$$

$$\frac{\partial}{\partial \mathbf{x}} = \epsilon \frac{\partial}{\partial \mathbf{x}_1}. \tag{7.1.72}$$

Using equation (7.1.70) and (7.1.67) gives

$$\sum_i f_i^{(k)} = 0, \quad k = 1, 2. \tag{7.1.73}$$

Denote a combined time-space derivative operator $\mathcal{D}_i$ as

$$\mathcal{D}_i = \frac{\partial}{\partial t} + \mathbf{c}_i \cdot \frac{\partial}{\partial \mathbf{x}} \tag{7.1.74}$$

$$\mathcal{D}_{1i} = \frac{\partial}{\partial t_1} + \mathbf{c}_i \cdot \frac{\partial}{\partial \mathbf{x}_1} \tag{7.1.75}$$

The expansion of equation (7.1.65) gives

$$\mathcal{D}_i f_i + \frac{\Delta t}{2} \mathcal{D}_i^2 f_i + \cdots = -\frac{1}{\tau \Delta t}(f_i - f_i^{eq}). \tag{7.1.76}$$

Using equations (7.1.70), (7.1.71), (7.1.72) and (7.1.76) we can write for different orders of ϵ

$$\mathcal{D}_{1i} f_i^{eq} = -\frac{1}{\tau \Delta t} f_i^{(1)} \tag{7.1.77}$$

$$\frac{\partial}{\partial t_2} f_i^{eq} + \mathcal{D}_{1i} f_i^{(1)} + \frac{\Delta t}{2} \mathcal{D}_{1i} f_i^{eq} = -\frac{1}{\tau \Delta t} f_i^{(2)}. \tag{7.1.78}$$

Combining equations (7.1.77) and (7.1.78) yields

$$\frac{\partial}{\partial t_2} f_i^{eq} + \left(1 - \frac{1}{2\tau}\right) \mathcal{D}_{1i} f_i^{(1)} = -\frac{1}{\tau \Delta t} f_i^{(2)}. \tag{7.1.79}$$

After summing equations (7.1.77) and (7.1.79) and using the constraints on the moments of the distribution functions (7.1.70), (7.1.71) and (7.1.72), we obtain

$$\frac{\partial}{\partial t_1} \psi + \frac{\partial}{\partial \mathbf{x}_1} \cdot (\mathbf{u}\psi) = 0 \tag{7.1.80}$$

$$\frac{\partial}{\partial t_2} \psi + \left(1 - \frac{1}{2\tau}\right) \frac{\partial}{\partial \mathbf{x}_1} \cdot \sum_i \mathbf{c}_i f_i^{(1)} = 0 \tag{7.1.81}$$

where

$$\begin{aligned} \sum_i \mathbf{c}_i f_i^{(1)} &= -\tau \Delta t \sum_i \mathbf{c}_i \mathcal{D}_i f_i^{eq} \\ &= -\tau \Delta t \left(\frac{\partial}{\partial t_1} (\mathbf{u}\psi) + \frac{\partial}{\partial \mathbf{x}_1} \cdot (\psi \mathbf{u}\mathbf{u} + c_s^2 \mathbf{I}) \right) \end{aligned} \tag{7.1.82}$$

The velocity $\mathbf{u}$ is dependent on the flow velocity gradient at the macroscopic level and the large space scale. Thus we can write equation (7.1.82) as

$$\sum_i \mathbf{c}_i f_i^{(1)} = -\tau \Delta t \left(\mathbf{u} \left(\frac{\partial}{\partial t_1} \psi + \frac{\partial}{\partial \mathbf{x}_1} \cdot (\psi \mathbf{u}) \right) + c_s^2 \frac{\partial}{\partial \mathbf{x}_1} \psi \right) \tag{7.1.83}$$

and then using equation (7.1.80)

$$\sum_i \mathbf{c}_i f_i^{(1)} = -\tau \Delta t \left(c_s^2 \frac{\partial}{\partial \mathbf{x}_1} \psi \right). \tag{7.1.84}$$

Substituting this expression into equation (7.1.81) yields

$$\frac{\partial}{\partial t_2}\psi = \Delta t \left(\tau - \frac{1}{2}\right) c_s^2 \frac{\partial}{\partial \mathbf{x}_1}\psi \tag{7.1.85}$$

which we combine with equation (7.1.80) to recover

$$\frac{\partial}{\partial t}\psi + \frac{\partial}{\partial \mathbf{x}} \cdot (\mathbf{u}\psi) = \Delta t \left(\tau - \frac{1}{2}\right) c_s^2 \frac{\partial^2}{\partial \mathbf{x}^2}\psi \tag{7.1.86}$$

which is the general form of the parabolic Fokker-Planck equation.

The Fokker-Planck equation we wish to use to simulate a FENE polymeric liquid is

$$\frac{\partial \psi}{\partial t} = -\frac{\partial}{\partial \mathbf{Q}} \cdot \left(\nabla \mathbf{v} \cdot \mathbf{Q}\psi - \frac{1}{2\lambda_1}\mathbf{F}\psi\right) + \frac{1}{2\lambda_1}\frac{\partial^2 \psi}{\partial \mathbf{Q}^2} \tag{7.1.87}$$

where $\mathbf{F}$ is the FENE force law and λ_1 is the polymeric relaxation time, so we require

$$\mathbf{u} = \nabla \mathbf{v} \cdot \mathbf{Q} - \frac{1}{2\lambda_1}\mathbf{F} \tag{7.1.88}$$

$$\Delta t \left(\tau - \frac{1}{2}\right) c_s^2 = \frac{1}{2\lambda_1} \tag{7.1.89}$$

and then the system evolving equations (7.1.65),(7.1.66),(7.1.67) is able to reproduce the physics of equation (7.1.87). The polymer stress $\mathbf{T}_p$ is provided by the Kramers expression

$$\mathbf{T}_p = \int \psi(\mathbf{Q})\mathbf{F}(\mathbf{Q})\mathbf{Q} d\mathbf{Q} - \mathbf{I} \tag{7.1.90}$$

and the equilibrium distribution is

$$\psi_0 = \frac{H(Q)^{-b/2}}{\int H(Q)^{-b/2} d\mathbf{Q}} \tag{7.1.91}$$

where

$$H(\chi) = \frac{1}{1 - Q^2/b}. \tag{7.1.92}$$

The scheme is summarised as

1. Calculate $\mathbf{u} = \nabla\mathbf{v} - \frac{1}{2\lambda_1}H(\chi)\mathbf{Q}$.
2. Calculate the lattice relaxation time $\tau = 1/(2\lambda_1\Delta t c_s^2) + 0.5$.
3. Initialise the distribution functions according to $f_i = \omega_i\psi_0 \; i = 0, \ldots, 8$.
4. For each time step for each lattice site:
   - Calculate the total probability function according to (7.1.67) $\psi = \sum_i f_i$
   - Update f_i^{eq} according to (7.1.66).
   - Perform collision step to obtain intermediate distribution functions $f_i^\star = f_i - \frac{1}{\tau}(f_i - f_i^{eq})$.
   - Perform the streaming step $f_i =$ move on lattice f_i^* by $\mathbf{c}_i$.
   - Perform the post streaming boundary condition.

It should be noted that for the FENE dumbbell the possible configuration space is the disk with radius $\sqrt{b}$ and it is necessary to apply a mass conserving boundary condition at the edge of the disk such as the bounce back condition. It is thought that other than having the mass conserving property that the exact nature of the boundary condition is not important since $\psi \to 0$ as $\mathbf{Q} \to \sqrt{b}$ [96].

Coupled Couette flow

We consider the start-up of plane Couette flow in which a polymeric liquid is enclosed between two parallel plates of infinite length separated by distance $L = 1$. For $t < 0$, the fluid and the two plates are at rest. At $t = 0$ the top plate begins to move in the positive x-direction with a speed $U = 1$. The problem is to find the time evolution of u, the horizontal component of the velocity, for $t > 0$. The velocity field is assumed to be of the form

$$u = u(y, t), \quad v = 0. \tag{7.1.93}$$

This velocity field automatically satisfies the incompressibility condition. Therefore, at any moment in time, the velocity may be determined from the hori-

zontal component of the dimensionless momentum equation

$$Re\frac{\partial u}{\partial t} = \beta\frac{\partial^2 u}{\partial y^2} - \frac{\partial T_{P,xy}}{\partial y} \tag{7.1.94}$$

where Re is the Reynolds number and β is the dimensionless viscosity ratio, which is defined at the ratio of the solvent to the total viscosity. The polymeric contribution to the extra-stress tensor for the 2d FENE model can be computed, at each instant in time using the Kramers expression

$$\mathbf{T_P}(\mathbf{x},t) = \frac{1-\beta}{We}\left(\frac{b+4}{b}\right)\left(\int \psi(\mathbf{Q})\mathbf{F}(\mathbf{Q})\mathbf{Q}d\mathbf{Q} - \mathbf{I}\right), \tag{7.1.95}$$

where $We = \lambda_1 U/L$ is the global Weissenberg number. The equation of motion (7.1.94) is discretised in time using the backwards Euler method and discretised in space using central differences

$$Re\left(\frac{u_j^{n+1} - u_j^n}{\Delta t}\right) = \beta\frac{u_{j+1}^{n+1} - 2u_j^{n+1} + u_{j-1}^{n+1}}{(\Delta y)^2} - \left(\frac{(T_{P,xy})_{j+1}^n - (T_{P,xy})_{j-1}^n}{2\Delta y}\right) \tag{7.1.96}$$

where Δt is the time step. Given the polymeric contribution to the shear stress at time $t^n = n\Delta t$, equation (7.1.96) can be solved to determine u at the new time. The numerical procedure can be summarised as

1. at time t^n solve the governing equations for $\mathbf{u}$ (7.1.96),

2. at each grid site solve the Fokker-Planck equation with the FENE force law using a sub-grid LBM to equilibrium,

3. computation of the local viscolastic stress tensor, (7.1.95),

4. addition of the extra stress to the momentum equation (7.1.96).

The lattice resolution used to solve each respective Fokker-Planck equation is determined locally based on the local We. As has been demonstrated in Figure 7.1.3, the number of grid points required for a certain degree of accuracy in the viscoelastic stress, is dependent on the local We. This allows the error to be controlled and optimised the computational speed.

7.1.5 Numerical Results

For the LBM of Ammar [2] we start by examining start-up shear flow where the velocity gradient given by

$$u_x = \dot{\gamma} y \tag{7.1.97}$$

$$u_y = 0 \tag{7.1.98}$$

where $\dot{\gamma}$ is the shear rate. The resulting state-state probability distribution function (pdf) for $We = 5$, $b = 10$ is shown in Figure 7.1.2 while the stress evolution for varying We is shown in Figure 7.1.1. This shows good agreement with results in Ammar [2] and Leonenko and Phillips [60]. Error analysis has been carried out for $We = 1$ and $We = 5$ and is shown in Figure 7.1.3. As no analytical solution exists, the shear stress has been normalised using the value obtained with the highest number of nodes for each case. Note that for lower We the shape of the pdf at state state is closer to the initial configuration and so for higher We we require a higher number of nodes to converge.

Next we considered extensional flow. In Figure 7.1.4 the steady state value of the extensional viscosity is presented with $b = 50$. Around $We = 0.5$ there is a drastic increase in the extensional viscosity and then a much higher plateau at higher We. As we can see from Figure 7.1.4 it is necessary to increase the number of grid points to capture the high We plateau. This sudden increase of the extensional viscosity is known as coil-stretch transition. The lower plateau corresponds to dumbbells that have only been weakly stretched and are close to the equilibrium extension where as the higher plateau corresponds to dumbbells that have been nearly fully stretched. When the dumbbells are nearly fully stretched the condition that $\psi(\mathbf{Q}) \to 0$ at the boundary is violated. This is the probably cause of the error at high We as the bounce back boundary condition is artificial and assumed that $\psi(\mathbf{Q}) \to 0$ at the boundary. In Figures 7.1.5 and 7.1.6 the growth of the extensional viscosity is shown with different values of We and the extensibility parameter b. This again shows good agreement with results by Singh et al. [96].

Now we present results for the model presented in this Chapter. Starting with steady state simple shear in Figures 7.1.7 and 7.1.8 we can see excellent agreement for the viscoelastic stress for small $We < 0.5$ and the relative errors

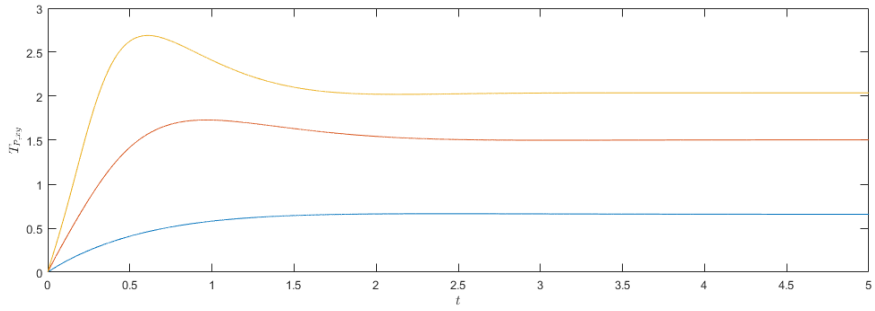

Figure 7.1.1: Start up shear flow shown for $We = 1$, $We = 3$ and $We = 5$ with $b = 10$.

have been given in Tables 7.4 and 7.5. As we can see the relative error at higher We for higher values of b is smaller. A significant source of error in our method is the assumption that the pdf of configuration of the dumbbells is close to equilibrium. In the Ammar model essentially utilises the fact that the Fokker-Planck equation is an advection-diffusion equation in configurational space which can be simulated by breaking momentum conservation in the lattice Boltzmann framework. This means that like the Onishi model, this model is only suitable for weak flows. In fact upon solving lattice Fokker-Planck equation (7.1.49) for steady state simple shear we find that when

$$\dot{\gamma}\lambda > \frac{2(b+6)}{8b\sqrt{3}} \tag{7.1.99}$$

the discrete probability distribution functions are no longer valid as $\psi_j \notin [0, 1]$. However, for weak flows the model developed in this Chapter is much more computationally efficient when compared to the model by Ammar [2]. For example with $We = 0.1$, $b = 10$ we find our method takes 0.0714s compared to 137.4993s to reach the steady state solution which is a very significant increase in speed. It might be beneficial in the future when solving large viscoelastic problems to use both methods depending on the local Weissenberg number. In Figure 7.1.9 the time evolution of the shear stress for start up shear flow is shown and shows good qualitative agreement with results by Ammar [2] and Singh et al. [96].

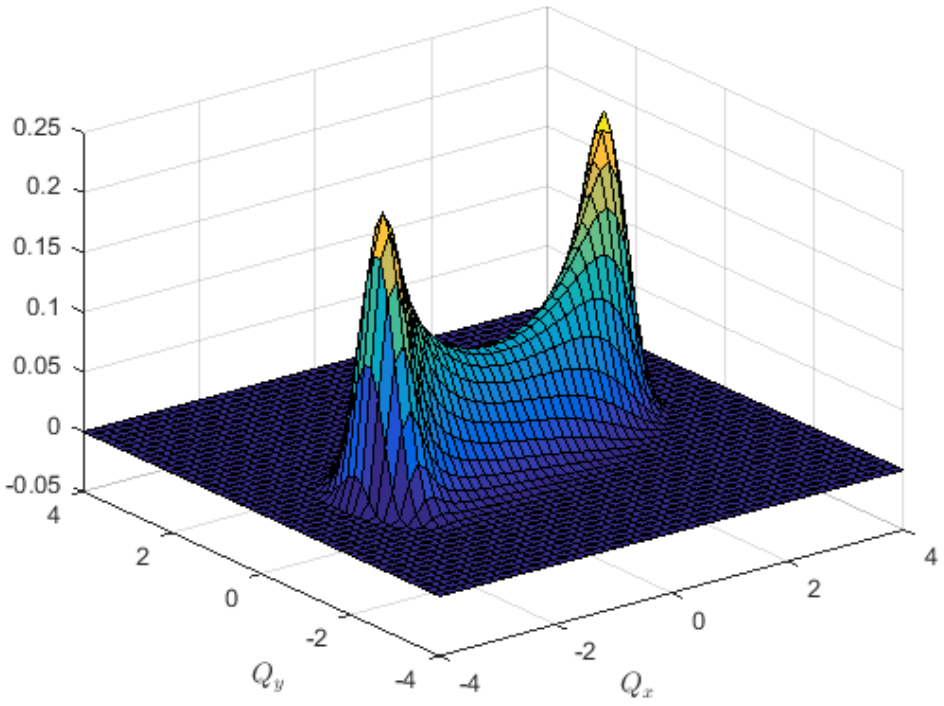

Figure 7.1.2: Shaded surface of the pdf for $We = 5$, $b = 10$

Couette Flow

The next set of results are for the full coupled flow problem of start-up plane Couette flow. Across the channel we solve the evolution of the horizontal velocity at 9 equally spaced points $y = y_k$, $k = 0, \ldots, 8$. The material and flow parameters are given by $b = 10$, $Re = 1$, $\lambda_1 = 1$ and $\beta = 1/9$. The time step is chosen as a compromise between performance and stability and is chosen to be $\Delta t = T/3000$ with $T = 10$. We present results for the evolution

We	0.01	0.05	0.1	0.5	1
Ammar	0.0071	0.0357	0.0714	0.3489	0.6580
Present work	0.0071	0.0357	0.0714	0.3571	0.7143
% Diff.	-0.1988	-0.0269	-0.0870	-2.3659	-8.5573

Table 7.4: Relative percentage errors in steady state shear stress with $b = 10$ between Ammar and the method developed in this Chapter.

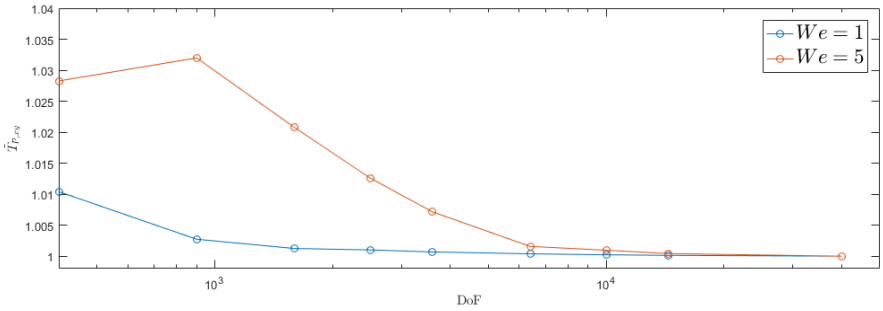

Figure 7.1.3: Error convergence for $We = 1$ and $We = 5$ with $b = 10$.

We	0.01	0.05	0.1	0.5	1
Ammar	0.0096	0.0480	0.0961	0.4770	0.9332
Present work	0.0096	0.0481	0.0962	0.4808	0.9615
% Diff.	-0.4234	-0.0669	-0.0406	-0.7890	-3.0360

Table 7.5: Relative percentage errors in steady state shear stress with $b = 100$ between Ammar and the method developed in this Chapter.

of the horizontal velocity component at the points y_0, y_2, y_4, y_6, y_8 in Figure 7.1.10. Qualitative agreement with Leonenko and Phillips [60] is observed. The velocity exhibits a strong overshoot followed by a weak undershoot before converging on a steady state value at around $t = 3$. The overshoot is strongest in the centre of the channel. The corresponding evolution of the shear stress at the mid-point of the channel is shown in Figure 7.1.11 which shows good agreement with the results by Leonenko and Phillips [60].

7.1.6 Discussion

In this chapter we have presented results for Lattice Boltzmann equation style solvers for the Fokker-Planck equation for the FENE dumbbell model. The model by Ammar [2] is robust under shear flows for a wide range of We but requires large grid sizes to capture the high plateau at large We under extensional flow, due to the artificiality of the bounce back condition.

To model complex viscoelastic flows it is necessary to couple the solver for the polymeric stress with a solver for the solvent velocity. The procedure follows an iterative process where first the governing equations for the velocity

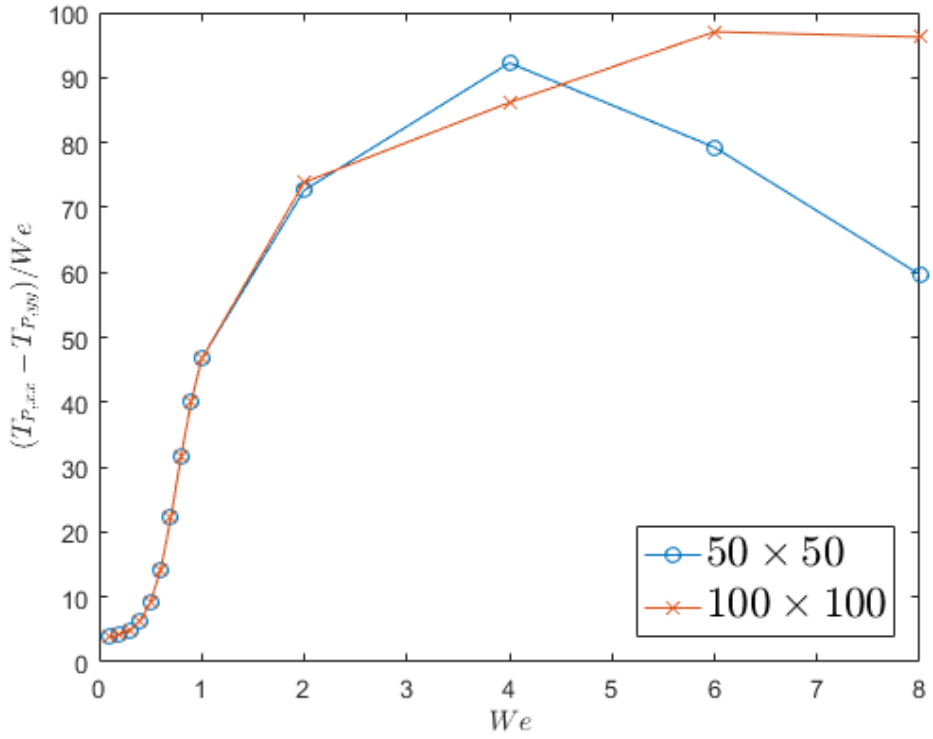

Figure 7.1.4: Steady state value of extensional viscosity with different We for $b = 50$.

and pressure are solved, then the polymeric stress tensor is evaluated at each point in physical space and then the velocity and pressure are updated based on the extra stress to the momentum equation. For the FENE dumbbell model there is no closed form constitutive equation for the polymeric stress tensor and therefore macroscopic simulation techniques cannot be employed. Based on the solution of the Fokker-Planck equation in the mesoscopic stage, a meso-macro numerical algorithm is described. This has been demonstrated for start-up plane Couette flow. Excellent agreement is obtained with the results by Leonenko and Phillips [60]. For large physical domains this is computationally expensive but with proper hardware implementation deserves attention in the framework of numerical methods for complex fluids.

In the model developed in this chapter, we have attempted to solve the Fokker-Planck equation using a single lattice to span both configurational and physical spaces. The LBM of Ammar [2] and Singh et al. [96] use a sepa-

rate lattice to span the configurational space for each point in physical space. Using a single lattice achieves a significant reduction in computation time. For small $We < 0.5$ the present model is capable of replicating the results by Ammar [2] and Singh et al. [96] for shear flow and computationally takes a small fraction of the time to reach a steady state solution (0.0714s compared to 137.4993s). As the method by Ammar [2] requires the Fokker-Planck equation to be solved at each physical point in space, this would lead to an even more significant reduction in computation time when used to solve for large physical domains. However, the assumption that the distribution functions can be expanded about the equilibrium solution means that our method is only suitable for weak flows $We < 0.5$. It might be therefore beneficial to investigate a dual approach if solving flows with a mixture of large and small values of the local We to achieve the best of both approaches.

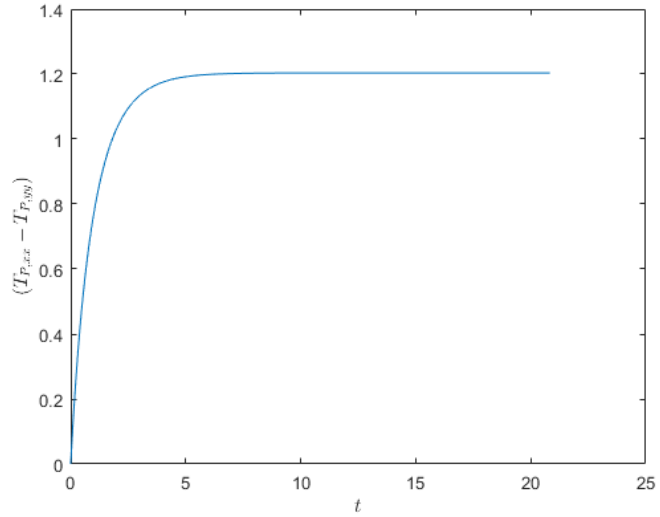

(a) b=20

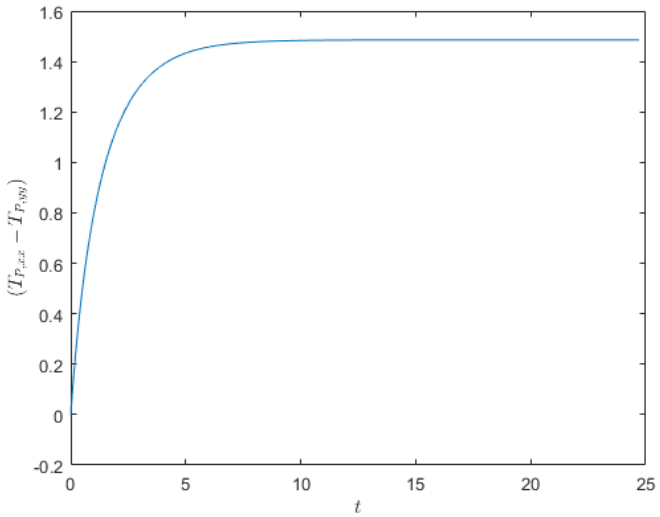

(b) b=50

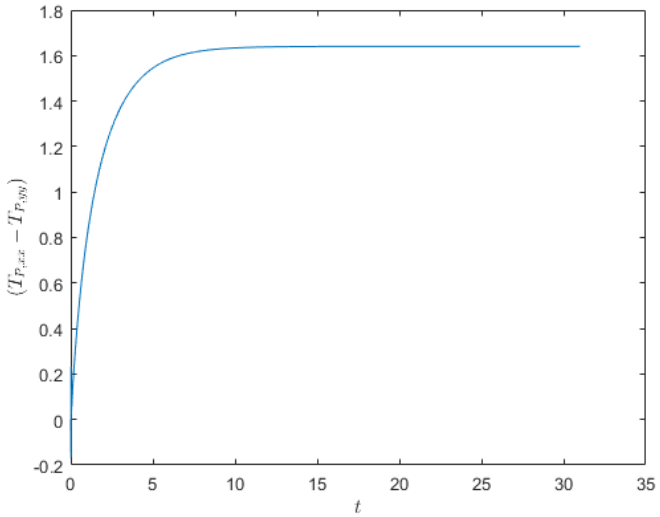

(c) b=100

Figure 7.1.5: Time evolution of the extensional viscosity for $We = 0.3$.

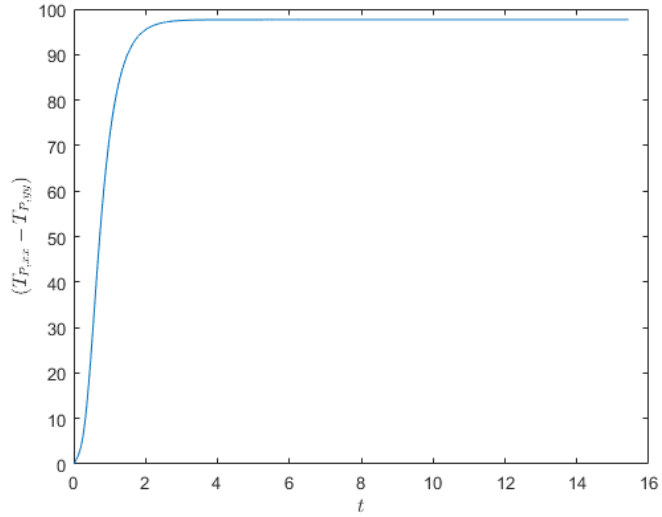

(a) b=20

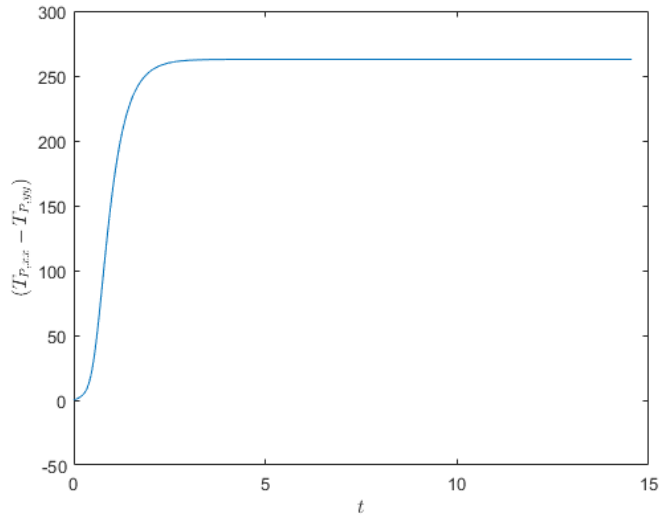

(b) b=50

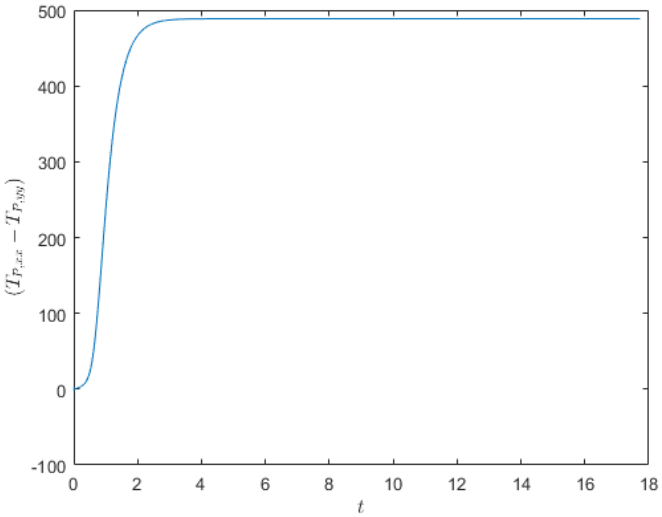

(c) b=100

Figure 7.1.6: Time evolution of the extensional viscosity for $We = 3.0$.

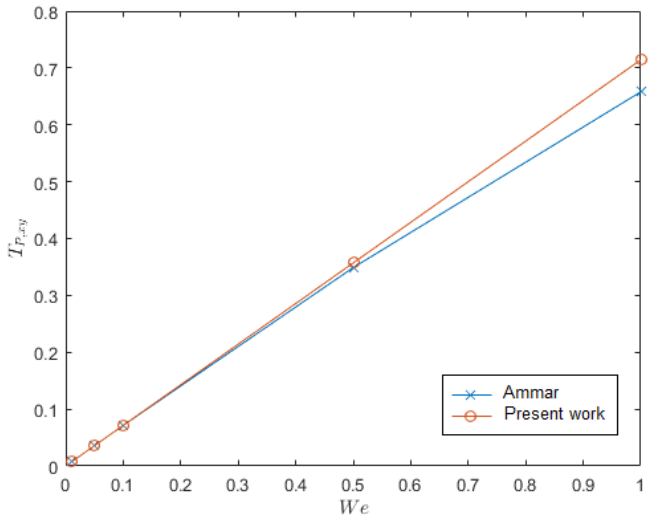

Figure 7.1.7: Comparison between the shear stress with $b = 10$ at different We between the method by Ammar and the method developed in this Chapter.

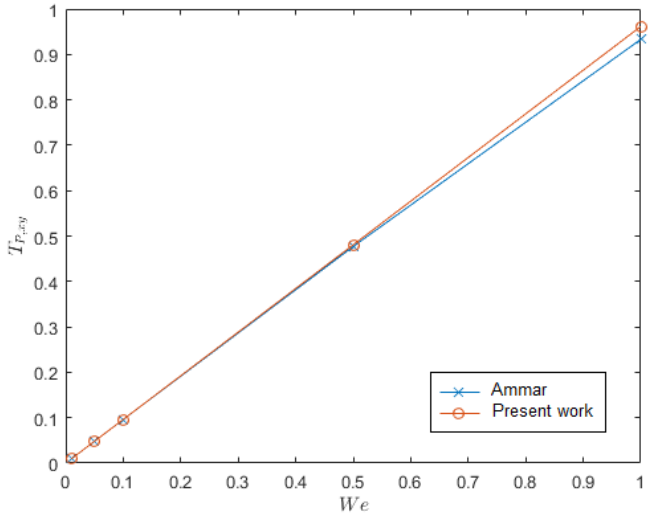

Figure 7.1.8: Comparison between the shear stress with $b = 100$ at different We between the method by Ammar and the method developed in this Chapter.

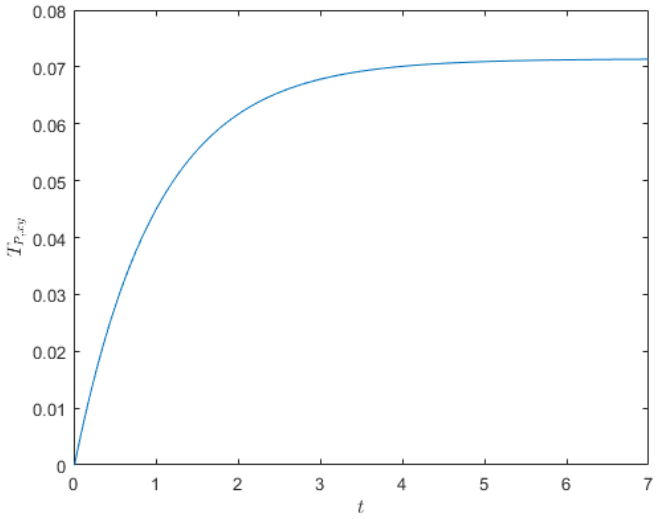

Figure 7.1.9: Time evolution of shear stress with $b = 10$ using the present model.

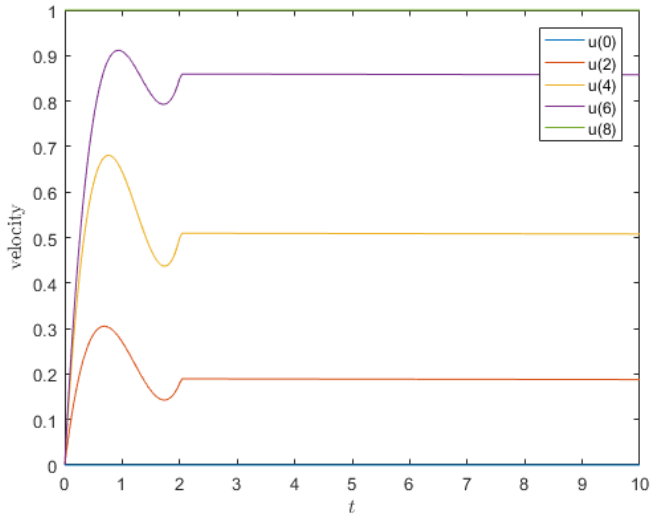

Figure 7.1.10: Time evolution of the horizontal component of velocity at different locations for the start-up plane Couette flow of a FENE fluid with $b = 10$, $\lambda_1 = 1$ and $T = 10$.

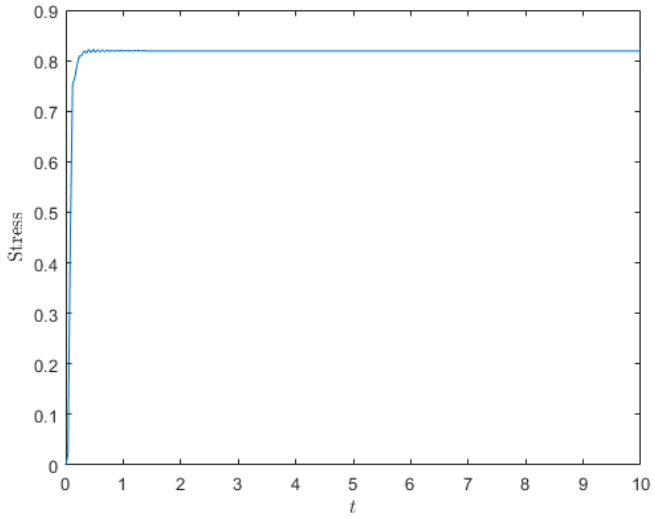

Figure 7.1.11: Time evolution of shear stress at the mid-channel location for the start-up plane Couette flow of a FENE fluid with $b = 10$, $\lambda_1 = 1$ and $T = 10$.

Chapter 8

Conclusions and future Work

The lattice Boltzmann method is a relatively new technique in computational fluid dynamics based on the resolution of physics at a mesoscopic level. It has already had many successes in solving many different flow scenarios such multi-phase fluid flows or flow through porous media and the aim of this thesis was to expand on this success into solving viscoelastic flows.

Chapter 1 is an introduction into LBM and put it into context based on other macroscopic fluid solvers and the LGCA which was its direct forebear. It is important to remember that there is no numerical scheme that is the best at solving every problem and attempts were made to highlight areas where LBM have significant advantages over traditional macroscopic solvers such as FDM or FEM.

Chapter 2 explains how to implement a LBM scheme. The collision algorithm is discussed and the two main approximations BGK and MRT are given. In practice the BGK is far more popular due to its ease of use but MRT has significant advantages for studying more complicated flows as there are non-physical parameters that can be tuned to improve stability. When solving large systems the propagation algorithm used can have a significant difference to the speed of the overall LBM. A more efficient implementation of the propagation algorithm in terms of the memory required is given. However, on modern computer architectures it has been found to be significantly slower than a two array approach. A major advantage of the LBM over traditional macroscopic fluid velocity solvers is the ease of implementation of boundary conditions. In LBM boundary conditions are applied locally and so it is very

simple to describe fluid flow in complex geometries such as porous media. The so called bounce-back condition is used to simulate no-penetration and no-slip condition at a boundary. The two major versions of the bounce-back condition, (on grid and mid grid) are described and results are presented as to the increase in accuracy from using the mid grid condition for Poiseuille flow. Zou-He [106] developed a constant velocity/pressure boundary condition that is second order accurate based on the assumption that the bounce back rule holds for the non-equilibrium part of the particle distribution function normal to the boundary and results are presented for the D2Q7 and D2Q9 lattice for Couette flow using the Zou-He constant velocity condition.

In Chapter 3 the derivation of the equilibrium distribution function is presented in two ways. Firstly it is given as a discretised version of the Maxwell-Boltzmann equilibrium distribution using Gauss-Hermite quadrature and secondly it is constructed from the macroscopic properties required and using them to solve the linear system to recover the coefficients of the equilibrium function. Also in Chapter 3 is the relation between the LBM and Navier-Stokes equations which is given by the Chapman-Enskog multi-scale procedure. Chapter 3 is vital when looking for ways to adapt the LBM to solve other problems such as the Fokker-Planck equation as shown in Chapter 7.

In Chapter 4 an overview of LBM for multiphase fluid flows is given. The four main approaches are chromodynamic models, pseudo-potential models, free-energy models and mean field models. Free energy and mean field models are necessary when examining non-isothermal flows but are computationally expensive and are not able to solve fluid flows with a large density ratio. Pseudo-potential models are easy to implement as they require adding a body force term to the LBM and are capable of simulating fluids with a high density ratio but have relatively low numerical stability and wide diffuse interfaces between the fluids. The colour model is capable of simulating fluids with a significant viscosity ratio and recovers the analytic solutions for Poiseuille flow and fingering simulations. In this Chapter the colour model is used to solve two and three layer Poiseuille flow and gives good agreement with the analytical solutions.

In Chapter 5 a LBM for droplets is discussed. Lattice Boltzmann methods are extremely well suited to modelling the behaviour of droplets on surfaces

since only the static contact angles are needed to simulate the impingement and spreading of droplets as the dynamic contact angle emerges naturally from the simulation without complicated treatment. In the context of real world applications this allows the LBM to be easily calibrated to match experimental results. The static contact angles can be measured by placing a droplet on a surface and tilting the surface until the droplet starts to move and measuring the advancing and receding contact angles relative to the surface. This then allows more complicated droplet flows to be studied numerically.

In Chapter 6 an overview of LBM for viscoelastic flows is presented. The multi-relaxation models for non-Newtonian LBE's proposed by Giraud et al. [31, 32] take advantage of the LB framework by incorporating viscoelastic effects into the collision operator so that characteristic quantities of complex fluids are given purely in terms of lattice moments. The ability to 'tune' the collision matrix gives these models the potential to recover the constitutive equation of choice without having to resort to additional numerical differentiation of macroscopic quantities such as the velocity gradient. This theoretical advantage has yet to be demonstrated correctly in practice and the relation between the viscoelastic properties and lattice moments is not well understood at present. The lattice Fokker-Planck models on the other hand have a firm mathematical basis as they are shown to be a direct discretisation of the continuous kinetic equation.

In Chapter 7 two lattice based approaches are used to solve the Fokker-Planck equation with the FENE force law. The method by Ammar [2] and Singh et al. [96] is presented and shows excellent agreement with other FENE solvers. This method though requires solutions to be generated on separate lattices since a separate Fokker-Planck equation at every position in physical space needs to be solved which is computationally expensive. Taking the work by Onishi et al. [75] as an inspiration the Fokker-Planck equation with a FENE force law was discretised using only one lattice for the whole physical space. This gives a dramatic increase in computational efficiency in terms of both memory and processing power. However, in deriving our model we assume that the distribution functions can be expanded about the equilibrium distribution and for strong flows this assumption does not hold. Therefore while our model is dramatically faster at computing polymeric stresses at small values of the

Weissenberg number ($We < 0.5$) it is unable to accurately capture polymeric behaviour for larger values of We. This contribution is being prepared for submission to Physical Review E. [61]. The start-up of plane Couette flow is considered. A numerical method for solving this problem based on a coupling of the method by Ammar [2] and a solver for macroscopic fluid velocity as been performed and shows excellent agreement for the temporal evolution of both the solvent velocity and the shear stress with the results by Leonenko and Phillips [60].

Future work involves capitalising on the success and features of the LBM by coupling our method for solving for the Fokker-Planck equation with the FENE force law, with a LBM for multiphase fluid flow. A current drawback to our approach is that is unable to accurately capture polymeric behaviour at larger values of We. Currently there a two ideas to improve or mitigate this drawback. Firstly it is worth investigating using more lattice speeds (corresponding to using more nodes in the Gaussian quadrature) when performing the discretisation. Presently the model expands the pdf about the equilibrium solution and adding more terms into this expansion should increase the range of permissible values of We. Secondly a hybrid approach may be adopted where at smaller values of We our model is used to solve for the polymeric stress and at higher values of We where our approach breaks down, use the LBM of Ammar [2]. This should deliver a considerable increase in the overall speed of solution of the polymeric stress. A distinct advantage of the LBM for multiphase fluid flow is for simulating droplets on surfaces, and so it is proposed to couple our method for computing the viscoelastic stresses with a LBM for droplets to simulate the flow of droplets of polymeric liquids on surfaces. This has industrial applications including ink-jet printing where many dyes and paints are viscoelastic.

Bibliography

[1] T. Abe, *Derivation of the lattice Boltzmann method by means of the discrete ordinate method for the Boltzmann equation*, J Comput Phys, 131 (1997), pp. 241–246.

[2] A. Ammar, *Lattice Boltzmann method for polymer kinetic theory*, J Non-Newton Fluid, 165 (2010), pp. 1082–1092.

[3] Y. Ba, H. Liu, J. Sun, and R. Zheng, *Color–gradient lattice Boltzmann model for simulating droplet motion with contact angle hysteresis*, Phys Rev E, 88 (2013), p. 043306.

[4] J. Bernsdorf, S. Harrison, S. Smith, P. Lawford, and D. Hose, *Applying the lattice Boltzmann technique to biofluids: A novel approach to simulate blood coagulation*, Comput Math Appl, 55 (2008), pp. 1408 – 1414. Mesoscopic Methods in Engineering and Science.

[5] P. L. Bhatnagar, E. P. Gross, and M. Krook, *A model for collision processes in gases. i. small amplitude processes in charged and neutral one-component systems*, Phys Rev, 94 (1954), pp. 511–525.

[6] C. Binetruy, F. Chinesta, and R. Keunings, *Flows in Polymers, Reinforced Polymers and Composites: A Multi-scale approach*, Springer, Cham, 2015.

[7] R. Bird, R. Armstrong, and O. Hassager, *Dynamics of Polymeric Liquids, Volume 1: Fluid Mechanics, 2nd edition*, Wiley, New York, 1987.

[8] R. Bird, C. Curtiss, R. Armstrong, and O. Hassager, *Dynamics of Polymeric Liquids, Volume 2: Fluid Mechanics, 2nd edition*, Wiley, New York, 1987.

[9] T. Blake, *The physics of moving wetting lines*, J Colloid Interface Sci, 299 (2006), pp. 1 – 13.

[10] J. Castrejón-Pita, K. Kubiak, A. Castrejón-Pita, M. Wilson, and I. Hutchings, *Mixing and internal dynamics of droplets impacting and coalescing on a solid surface*, Phys Rev E, 8 (2013), p. 023023.

[11] J. R. Castrejón-Pita, E. S. Betton, K. J. Kubiak, M. C. T. Wilson, and I. M. Hutchings, *The dynamics of the impact and coalescence of droplets on a solid surface*, Biomicrofluidics, 5 (2011).

[12] C. Cercignani, *The Boltzmann Equation and its Applications*, New York: Springer, 1988.

[13] S. Chapman and T. G. Cowling, *The Mathematical Theory of Non-Uniform Gases, 3rd ed.*, Cambridge Mathematical Library, Cambridge, 1970, ch. 16.

[14] H. Chen, B. Boghosian, P. Coveney, and M. Nekovee, *A Ternary Lattice Boltzmann Model for Amphiphilic Fluids*, PHILOS T ROY SOC A, 456 (2000), pp. 2043–2057.

[15] H. Chen, S. Chen, and W. Matthaeus, *Recovery of the Navier-Stokes equations using a lattice-gas Boltzmann method*, Phys Rev A, 45 (1992), pp. R5339–R5342.

[16] S. Chen, H. Chen, D. Martinez, and W. Matthaeus, *Lattice Boltzmann model for simulation of magnetohydrodynamics*, Phys Rev Lett, 67 (1991), p. 3776.

[17] S. Chen and D. G., *Lattice Boltzmann method for fluid flows*, Annu Rev Fluid Mech, 30 (1998), pp. 329–364.

[18] S. Chen, X. He, and L.-S. Luo, *Lattice Boltzmann models for multiphase flows*, in Computational Methods for Multiphase Flow, A. Prosperetti and G. Tryggvason, eds., Cambridge University Press, 2007, pp. 157–192.

[19] X.-P. Chen, *Applications of lattice Boltzmann method to turbulent flow around two-dimensional airfoil*, Eng Appl Comput Fluid Mech, 6 (2012), pp. 572–580.

[20] I.-L. Chern, J. Glimm, O. McBryan, B. Plohr, and S. Yaniv, *Front tracking for gas dynamics*, J Comput Phys, 62 (1986), pp. 83–110.

[21] M. Creutz, *Quarks, Gluons and Lattices*, Cambridge University Press, Cambridge, 1983.

[22] P. G. de Gennes, *Wetting: statics and dynamics*, Rev Mod Phys, 57 (1985), pp. 827–863.

[23] P. J. Dellar, *Bulk and shear viscosities in lattice Boltzmann equations*, Phys. Rev. E, 64 (2001), p. 031203.

[24] C. Denniston, E. Orlandini, and J. M. Yeomans, *Lattice Boltzmann simulations of liquid crystal hydrodynamics*, Phys. Rev. E, 63 (2001), p. 056702.

[25] B. Derby, *Inkjet printing of functional and structural materials: Fluid property requirements, feature stability, and resolution*, Annu Rev Mater Sci, 40 (2010), pp. 395–414.

[26] D. d'Humières, A. Cloquer, and P. Lallemand, *Lattice gas models for 3d hydrodynamics*, Europhys Lett, 25 (1986), p. 129.

[27] U. D'Ortona, D. Salin, M. Cieplak, R. B. Rybka, and J. R. Banavar, *Two-color nonlinear Boltzmann cellular automata: Surface tension and wetting*, Phys Rev E, 51 (1995), pp. 3718–3728.

[28] J.-B. Dupont and D. Legendre, *Numerical simulation of static and sliding drop with contact angle hysteresis*, J Comput Phys, 229 (2010), pp. 2453 – 2478.

[29] S. Fathi and P. Dickens, *Challenges in drop-on-drop deposition of reactive molten nylon materials for additive manufacturing*, J Mater Process Tech, 213 (2013), pp. 84 – 93.

[30] U. Frisch, B. Hasslacher, and Y. Pomeau, *Lattice gas automata for the Navier-Stokes equations*, Phys Rev Lett, 56 (1986), pp. 1505–1508.

[31] L. Giraud, D. d'Humières, and P. Lalleemand, *A lattice Boltzmann model for viscoelasticity*, Int. J. Mod. Phys. C,, 8 (1997), pp. 805–815.

[32] ——, *A lattice Boltzmann method for Jeffreys viscoelastic fluid*, Europhys. Lett, 42 (1998), pp. 625–630.

[33] J. Glimm, M. J. Graham, J. Grove, X. L. Li, T. M. Smith, D. Tan, F. Tangerman, and Q. Zhang, *Front tracking in two and three dimensions*, Comps Math Appl, 35 (1998), pp. 1–11.

[34] J. Glimm, J. W. Grove, X. L. Li, K.-m. Shyue, Y. Zeng, and Q. Zhang, *Three-dimensional front tracking*, SIAM J Sci Comput, 19 (1998), pp. 703–727.

[35] J. Glimm, E. Isaacson, D. Marchesin, and O. McBryan, *Front tracking for hyperbolic systems*, Adv Appl Math, 2 (1981), pp. 91–119.

[36] A. Gunstensen, D. H. Rothman, S. Zaleski, and G. Zanetti, *Lattice Boltzmann model of immiscible fluids*, Phys Rev A, 43 (1991), pp. 4320–4327.

[37] Z. Guo, C. Zheng, and B. Shi, *Discrete lattice effects on the forcing term in the lattice Boltzmann method*, Phys Rev E, 65 (2002b), p. 046308.

[38] I. Halliday, A. P. Hollis, and C. M. Care, *Lattice Boltzmann algorithm for continuum multicomponent flow*, Phys Rev E, 76 (2007), p. 026708.

[39] F. H. Harlow and J. E. Welch, *Numerical calculation of time-dependent viscous incompressible flow of fluid with free surface*, Phys Fluids, 8 (1965), pp. 2182–2189.

[40] X. He, S. Chen, and G. Doolen, *A Novel Thermal Model for the Lattice Boltzmann Method in Incompressible Limit*, J. Comp Phys, 146 (1998), pp. 282 – 300.

[41] X. He and G. Doolen, *Thermodynamic foundation of kinectic theory and lattice Boltzmann models for multiphase flows*, J Stat Phys, 107 (2002), pp. 309–328.

[42] X. He and L. L-S, *A priori derivation of the lattice Boltzmann equation*, Phys Rev E, 57 (1997), pp. R6333–R6336.

[43] X. He, X. Shan, and G. Doolen, *Discrete Boltzmann equation model for nonideal gases*, Phys Rev E, 57 (1998), pp. R13–R16.

[44] M. Herrchen and H. Öttinger, *A detailed comparison of various FENE dumbbell models*, J Non-Newton Fluid, 68 (1997), pp. 17–42.

[45] F. Higuera and J. Jimenez, *Boltzmann approach to lattice gas simulations*, Europhys Lett, 9 (1989), p. 663.

[46] A. P. Hollis, T. J. Spencer, I. Halliday, and C. M. Care, *Dynamic wetting boundary condition for continuum hydrodynamics with multi-component lattice Boltzmann equation simulation method*, IMA J Appl Math, 76 (2011), pp. 726–742.

[47] J. Horbach and D. Frenkel, *Lattice-Boltzmann method for the simulation of transport phenomena in charged colloids*, Phys. Rev. E, 64 (2001), p. 061507.

[48] R. R. Huilgol and N. Phan-Thien, *Fluid Mechanics of Viscoelasticity*, Elsevier Science BV, Amsterdam, 1997.

[49] D. Humières, *Multiple–relaxation–time lattice Boltzmann models in three dimensions*, Philos T R Soc A, 360 (2002), pp. 437–451.

[50] T. Inamuro, T. Ogata, S. Tajima, and N. Konishi, *A lattice Boltzmann method for incompressible two-phase flows with large density differences*, J Comput Phys, 198 (2004), pp. 628–644.

[51] K. Kadau, J. Barber, T. Germann, B. Holian, and B. Alder, *Atomistic methods in fluid simulation*, Philos T Roy Soc A, 368 (2010), pp. 1547–1560.

[52] J. Koelman, *A simple lattice Boltzmann scheme for Navier-Stokes fluid flow*, Europhys Lett, 15 (1991), p. 603.

[53] T. Krüger, H. Kusumaatmaja, A. Kuzmin, O. Shardt, G. Silva, and E. M. Viggen, *The Lattice Boltzmann Method*, Springer International Publishing Switzerland, 2017.

[54] F. Kuznik and G. Rusaouen, *Numerical prediction of natural convection occurring in building components: A double-population lattice Boltzmann method*, Numer Heat Tr A-Appl, 52 (2007), pp. 315–335.

[55] A. J. Ladd, *Lattice-Boltzmann methods for suspensions of solid particles*, Mol Phys, 113 (2015), pp. 2531–2537.

[56] P. Lallemand and L.-S. Luo, *Theory of the lattice Boltzmann method: Dispersion, dissipation, isotropy, Galilean invariance, and stability.*, Phys. Rev. E., 61 (2000), pp. 6546–6562.

[57] M. Laso and H. Öttinger, *Calculation of viscoelastic flow using molecular models: the connffessit approach*, J Non-Newton Fluid, 47 (1993), pp. 1 – 20.

[58] M. Latva-Kokko and D. Rothman, *Diffusion properties of gradient-based lattice Boltzmann models of immiscible fluids*, Phys Rev E, 71 (2005), p. 056702.

[59] ——, *Scaling of dynamic contact angles in a lattice-Boltzmann model*, Phys Rev Lett, 98 (2007), p. 254503.

[60] G. M. Leonenko and T. N. Phillips, *The Prediction of Plane Couette Flow for a FENE Fluid Using a Reduced Basis Approximation of the Fokker-Planc Equation*, Int J Mult Comp Eng, 9 (2011), pp. 73–88.

[61] E. Lewis and T. N. Phillps, *A Lattice Boltzmann Approach for the FENE Dumbbell model*, Phys Rev E, (2017). In preparation.

[62] S. V. Lishchuk, C. M. Care, and I. Halliday, *Lattice Boltzmann algorithm for surface tension with greatly reduced microcurrents*, Phys Rev E, 67 (2003), p. 036701.

[63] P. Love, M. Nekovee, P. Coveney, J. Chin, N. GonzÃ¡lez-Segredo, and J. Martin, *Simulations of amphiphilic fluids using mesoscale lattice-Boltzmann and lattice-gas methods*, Comput Phys Commun, 153 (2003), pp. 340 – 358.

[64] A. Lozinski and C. Chauvière, *A fast solver for Fokker-Planck equation applied to viscoelastic flows calculations: 2D FENE model*, J Comput Phys, 189 (2003), pp. 607 – 625.

[65] A. Lozinski, R. Owens, and T. N. Phillips, *The Langevin and Fokker-Planck Equations in Polymer Rheology*, in Numerical Methods for Non-Newtonian Fluids, R. Glowinski and J. Xu, eds., Elsevier B.V. Amsterdam, 2011, pp. 211–303.

[66] L. Luo and X. He., *Theory of the lattice Boltzmann method: From the Boltzmann equation to the lattice Boltzmann equation.*, Phys Rev E, (1997), pp. 6811–6817.

[67] N. Martys and H. Chen, *Simulation of multicomponent fluids in complex three-dimensional geometries by the lattice Boltzmann method*, Phys Rev E, 53 (1996), pp. 743–750.

[68] K. Mattila, J. Hyväluoma, T. Rossi, M. Aspnäs, and J. Westerholm, *An efficient swap algorithm for the lattice Boltzmann method*, Comput Phys Commun, 176 (2007), pp. 200–210.

[69] G. McNamara and G. Zanetti, *Use of the Boltzmann equation to simulate lattice gas automata*, Phys Rev Lett., 61 (1988), p. 2332.

[70] A. Mohamad and A. Kuzmin, *A critical evaluation of force term in lattice Boltzmann method, natural convection problem*, Int, J. Heat Mass Transfer, 53 (2010), pp. 990 – 996.

[71] D. Moroni, B. Rotenberg, J.-P. Hansen, S. Succi, and S. Melchionna, *Solving the Fokker-Planck kinetic equation on a lattice*, Phys Rev E, 73 (2006), p. 066707.

[72] M. Nekovee, P. Coveney, H. Chen, and B. Boghosian, *Lattice-Boltzmann model for interacting amphiphilic fluids*, Phys. Rev. E, 62 (2000), pp. 8282–8294.

[73] W. F. Noh and P. Woodward, *SLIC (Simple Line Interface Calculation)*, Springer Berlin Heidelberg, Berlin, Heidelberg, 1976, pp. 330–340.

[74] OED Online, *viscoelasticity, n.*, 2016. [Accessed March, 2016].

[75] J. Onishi, Y. Chen, and H. Ohashi, *A lattice Boltzmann model for polymeric liquids*, Prog Comput Fluid Dy, 5 (2005), pp. 75–84.

[76] J. Onishi, A. Kawasaki, Y. Chen, and H. Ohashi, *Lattice Boltzmann simulation of capillary interactions among colloidal particles*, Comput Math Appl, 55 (2008), pp. 1541 – 1553.

[77] P. Pavlo, G. Vahala, and L. Vahala, *Higher order isotropic velocity grids in lattice methods*, Phys Rev Lett, 80 (1998), pp. 3960–3963.

[78] A. Peterlin, *Hydrodynamics of macromolecules in a velocity field with longitudinal gradient*, J. Polym. Sci. B, 4 (1966), pp. 287–291.

[79] N. Phan-Thien, *Understanding Viscoelasticity: Basics of Rheology*, Advanced Texts in Physics, Springer Berlin Heidelberg, 2013.

[80] T. N. Phillips and R. Owens, *Computational Rheology*, Imperial College Press, London, 2002.

[81] T. N. Phillips and G. Roberts, *Lattice Boltzmann models for non-Newtonian flows*, IMA J Appl Math, 76 (2011), pp. 790–816.

[82] Y. Qian, D. d'Humières, and P. Lallemand, *Lattice BGK models for the Navier-Stokes equation*, Europhys Lett, 17 (1992), p. 479.

[83] L. E. Reichl, *A Modern Course in Statistical Physics*, John Wiley & Sons, Inc, New York, 1998.

[84] T. Reis, *The Lattice Boltzmann Method for Complex Flows*, PhD thesis, Cardiff University, School of Mathematics, August 2007.

[85] T. Reis and T. N. Phillips, *Lattice Boltzmann model for simulating immiscible two-phase flows*, J Phys A-Math Theor, 40 (2007a), pp. 4033–4053.

[86] M. Renardy, Y. Renardy, and J. Li, *Numerical simulation of moving contact line problems using a volume-of-fluid method*, J Comput Phys, 171 (2001), pp. 243 – 263.

[87] J. Rivet and J. Boon, *Lattice Gas Hydrodynamics*, Cambridge University Press, Cambridge, 2001.

[88] D. Rothman and J. Keller, *Immiscible cellular-automaton fluids*, J Stat Phys, 52 (1988), pp. 1119–1127.

[89] J. S. Rowlinson and B. Widom, *Molecular Theory of Capillarity*, Oxford University Press, Oxford, 1982.

[90] R. Scardovelli and S. Zaleski, *Direct Numerical simulation of free-surface and interfacial flow*, Annu Rev Fluid Mech, 31 (1999), pp. 567–603.

[91] J. D. Schieber and H. C. Öttinger, *The effects of bead inertia on the Rouse model*, J Chem Phys, 89 (1988), pp. 6972–6981.

[92] A. D. Schleizer and R. T. Bonnecaze, *Displacement of a two-dimensional immiscible droplet adhering to a wall in shear and pressure-driven flows*, J Fluid Mech, 383 (1999), pp. 29–54.

[93] M. Seaton, R. Anderson, S. Metz, and W. Smith, *DL_MESO: highly scalable mesoscale simulations*, Mol Simulat, 39 (2013), pp. 796–821.

[94] M. Sellier and E. Trelluyer, *Modeling the coalescence of sessile droplets*, Biomicrofluidics, 3 (2009), p. 022412.

[95] X. Shan and H. Chen, *Lattice Boltzmann model for simulating flows with multiple phases and components*, Phys Rev E, 47 (1993), pp. 1815–1819.

[96] S. Singh, G. Subramanian, and S. Ansumali, *Lattice Fokker Planck for dilute polymer dynamics*, Phys Rev E, 88 (2013), p. 013301.

[97] P. A. Skordos, *Initial and boundary conditions for the lattice Boltzmann method*, Phys Rev E, 48 (1993), pp. 4823–4842.

[98] H. Song, H.-W. Li, M. Munson, T. Van Ha, and R. Ismagilov, *On–chip titration of an anticoagulant argatroban and determination of the clotting time within whole blood or plasma using a plug-based microfluidic system*, Anal Chem, 78 (2006), pp. 4839–4849.

[99] P. Spelt, *A level-set approach for simulations of flows with multiple moving contact lines with hysteresis*, J Comput Phys, 207 (2005), pp. 389 – 404.

[100] S. Succi, *The Lattice Boltzmann Equation for Fluid Dynamics and Beyond*, Oxford University Press, Oxford, 2001.

[101] M. Swift, W. R. Osborn, and J. M. Yeomans, *Lattice Boltzmann simulation of nonideal fluids*, Phys Rev Lett, 75 (1995), pp. 830–833.

[102] R. I. Tanner, *Engineering Rheology*, Oxford University Press, Oxford, 2002.

[103] J. Yang and E. Boek, *A comparison study of multi-component lattice Boltzmann models for flow in porous media applications*, Comput Math Appl, 65 (2013), pp. 882–890.

[104] X. Yang, V. H. Chhasatia, J. Shah, and Y. Sun, *Coalescence, evaporation and particle desposition of consecutively printed colloidal drops*, Soft Matter, 8 (2012), pp. 9205–9213.

[105] D. Ziegler, *Boundary conditions for lattice Boltzmann simulations*, J Stat Phys, 71 (1993), pp. 1171–1177.

[106] Q. Zou and X. He, *On pressure and velocity boundary conditions for the lattice Boltzmann BGK model*, Phys Fluids, 9 (1997), pp. 1591–1598.